Department of Physics and Astronomy

University of Heidelberg

Bachelor thesis in Physics

submitted by

Philipp Immanuel Voigt

born in Friedrichshafen

2019

Simulation and measurement of the water-sided viscous shear stress without waves

This Bachelor thesis has been carried out by

Philipp Immanuel Voigt

at the

Institute of Environmental Physics

under the supervision of

Prof. Dr. Bernd Jähne

Zusammenfassung

Die lokale viskose Schubspannung wurde in der wasserseitigen Luft-Wasser-Grenzschicht, im ringförmigen Wind-Wellenkanal Aeolotron am Institut für Umweltphysik in Heidelberg, gemessen. Die Messungen wurden bei niedrigen Windgeschwindigkeiten bis $u_{10} \sim 6{,}1\,\mathrm{m/s}$ durchgeführt, und es wurde im Instationären direkt nach dem Anschalten und bei periodischem An- und Abschalten des Windes gemessen, sowie im stationären Fall, bei dem Wind und Strömungsfeld im Wasser im Gleichgewicht waren. Die Wellenbildung wurde durch Zugabe von $3{,}3\,\mathrm{g/L}$ des Oberflächenfilms Triton X-100 zum Wasser unterdrückt. Aktive Thermographie wurde verwendet um dünne Linien auf der Wasseroberfläche zu erhizten, und deren Verbreiterung zu beobachteten. Diese Methode kombiniert die Vorteile von einem brührungslosen, luftseitigen Aufbau und der Unabhängigkeit vom herrschenden Windprofil. Mit einem im Rahmen dieser Arbeit entwickelten Simulationsansatz konnte aus der Verbreiterung der geheizten Linien die viskose Schubspannung mit einer maximalen zeitlichen Auflösung von einer Sekunde bestimmt werden. Dabei wurde die zeitliche Entwiklung der Lineienbreiten numerisch simuliert, wobei drei Parameter variiert wurden. Diese waren die anfängliche Linienbreite und die räumlich konstanten Komponenten der Schubspannung in Tiefenrichtung und parallel zu den geheizten Linien. Die Ergebnisse der Simulationen wurden dann interpoliert und mit den Messungen abgeglichen. Die hierbei erhaltenen Werte für die viskose Schubspannung der stationären Messungen wurden mit einer direkten Referenzmessung basierend auf Particle Streak Velocimetry verglichen. Die Unterschiede zwischen den beiden Methoden waren keiner als 20 %.

Abstract

The local viscous sheer stress in the watersided boundary layer of the air-water interface was measured at the Aeolotron, an annular wind-wave facility located at the Institute of Environmental Physics in Heidelberg. The measurements were conducted at low wind speeds up to $u_{10} \sim 6.1\,\mathrm{m/s}$, under non-stationary conditions directly after turning the wind on, while periodically switching the wind on and off, as well as under stationary conditons with the wind- and water flow fields being in equilibrium. The wave formation was suppressed by adding $3.3\,\mathrm{mg/L}$ of the surfactant Triton X-100 to the water. Active thermography was used for heating thin lines on the water surface, and monitoring their broadening. This method combines the advantages of an air-sided and contactless setup and independence on the prevailing wind profile. Using an approach based on simulation developed in this thesis, the viscous shear stress could be obtained with a maximal temporal resolution of one second. Thereby the temporal development of the line widths were simulated numerically, varying three parameters. These were the initial line width and the spatially constant components of the shear stress with respect to depth and the direction parallel to the lines. The results of the simulations were interpolated and matched with the measured line widths. The hereby obtained values for the viscous shear stress were for the stationary measurements compared to a direct measurement based on particle streak velocimetry. The discrepancies were smaller than 20 %.

Contents

1 Introduction

Humankind is influencing the world's climate by its emissions of CO_2. Not all of these anthropogenic emissions stay in the atmosphere, however, as a substantial fraction is taken up by the different active carbon reservoirs, the largest being the ocean (Roy-Barman and Jeandel [2016]). Furthermore, it is absorbing about a third of the anthropogenic emissions (Gruber et al. [2019]), thereby mitigating the temperature increase due to the enhanced greenhouse effect (Crueger et al. [2008]). However, the increased CO_2 concentration in the upper ocean lead to acidification (Hoegh-Guldberg et al. [2014]), with negative effects on marine biota (Kroeker et al. [2013]). In order to be able to model the changes of the future climate, a profound understanding of the exchange processes, those not being limited to gas transfer, between the atmosphere and the ocean is crucial. Still, these processes are not fully understood yet (Liss and Johnson [2014]).

In order to investigate the exchange processes, wind-waves facilities are built to ease the monitoring and adjustment of the conditions relative to in situ measurements. These facilities can be divided into two groups; linear and annular tanks. The first have a limited length and hence also fetch, meaning that the wave fields often cannot develop fully. The Aeolotron in Heidelberg, in which the measurements presented in this thesis were conducted, is of the latter type of facility. These annual tanks avoids the disadvantage of a constrained fetch, enabling the wave fields to develop and hence resemble the open ocean conditions better.

The fluid layers close to the interface between air and water, that is, the boundary layers, are limiting the exchange processes, as the transport in these layers is diffusion controlled. This is especially pronounced at low wind speeds, when surface renewal events and microscale wave breaking are less prominent (Kräuter et al. [2014]). Deeper layers tend to be well mixed, and are thereby not prone to limiting the exchange between the compartments (Münnich and Flothmann [1975]).

The momentum transport through the viscous boundary layer, that is, the viscous shear stress, is proportional to the velocity gradient with respect to the normal of the interface. Further on, the transfer velocities of gas exchange increases with augmented shear, whereas the boundary layer thickness decreases (Jähne [2012b]). Having a proper handle on this quantity is therefore of interest. This is can be achieved by measuring the air-sided logarithmic velocity profile, if present, from which it can be extracted (Charnock [1955]). Due to non-slip conditions, the viscous shear is conserved over the interface and hence equal in both the air- and water-sided boundary layer. In the case of annular wind-wave facilities, there is no logarithmic wind profile due to secondary flows (Bopp [2014]).

Methods to measure the shear stress without relying on the wind profile exist. Looking at the momentum balance for the water compartment, allows for an estimation of transferred momentum from the wind (Ilmberger [1981], Schwenk [2019]). This method relies on measured water velocities, which is laborious if the whole velocity field is

considered. Another weakness of this method is the need for a friction correction from the channel walls and built-in measurement devices, which lead to large uncertainties and dependence on the particular setup and experiment conditions (Bopp [2014]). Further on, the method of particle streak velocimetry (PSV) can also be utilized for the determination of the shear stress (Bopp [2018]). The method relies on tracking particles, and is rather effortful, especially in the field when tracking the particles watersided or close to the interface.

Another approach which deploys active thermography to determine the viscous shear stress is presented in this work. In Heidelberg, the measurement principle was first assessed by Garbe et al. [2007], applied by Gutsche [2014] using a similar configuration, and further developed by Holtmann [2017], Emmel [2017] and Rembeck [2018]. It is applicable independently on the wind profile, offers temporally resolved results and does not disturb the to be measured system. The setup consists of a near infrared laser and an infrared camera, both mounted above the water surface. The laser heats a thin line is heated at the water surface perpendicular to the wind, and its broadening is affected by the velocity gradient in the viscous boundary layer. The temporal evolution is monitored by the camera, allowing for the determination of the viscous shear stress. In comparison to the previous work, the main focus of this thesis is to lay the theoretical foundations for the evaluation of the measurements, and comparing the results to the PSV-method and thereby reach proof-of-concept. The chosen approach is to analyse the measurements by comparing them to a numerical simulation. The experiments are conducted without the influence of waves, which is achieved by applying surfactants to the water, in order to simplify the conditions.

2 | Theory

In this chapter, the necessary physical basics will be introduced.

2.1 The boundary layer and shear stress

Wind blowing over a smooth water surface, will act on this surface with a shear stress. This leads to a momentum transfer from the air to the water. Due to the non-slip condition at the air-water interface, both the velocity and momentum transfer will be continuous across the interface. Under stationary conditions, the watersided viscous boundary layer can simplifiedly be regarded as a Couette flow, i.e. as the flow between to parallel surfaces moving tangentially. The Navier-Stokes equation can be analytically solved for this problem, yielding a linear velocity profile with depth and hence a constant velocity gradient, see figure 2.1. From this consideration, it follows for the viscous shear stress τ_{visc}, with μ being the dynamic viscosity:

$$\tau_{\text{visc}} = \mu \left.\frac{\partial u}{\partial z}\right|_{z=0}. \tag{2.1}$$

In general, the water surface is subject to waves, leading to additional shear stress, likewise will turbulence add a contribution. The transfer of horizontal momentum in vertical direction, τ_{xz}, thereby consists of the following components (Bopp [2018]):

$$\tau_{xz} = \tau_{\text{wave},\,xz} + \tau_{\text{turb},\,xz} + \tau_{\text{visc},\,xz} \tag{2.2}$$

In the viscous boundary layer, the absence of turbulence yields $\tau_{\text{turb},\,xz} = 0$. Further on, in stead of referring to τ, it is common to use the friction velocity u_*, that is,

$$u_* = \sqrt{\tau/\rho}. \tag{2.3}$$

In the following, however, only τ will be used.

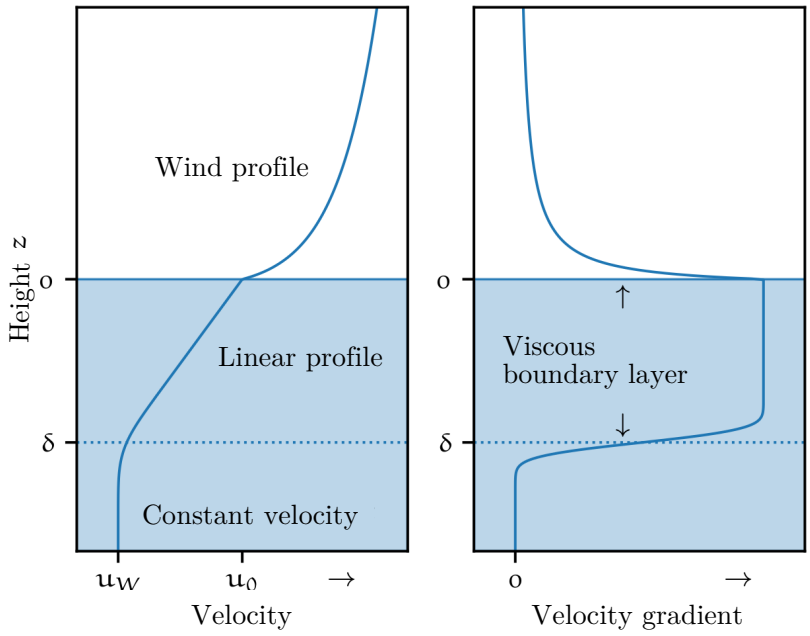

FIG 2.1.: A sketch of the simplified representation of the viscous boundary layer. Adapted and edited from Emmel [2017].

2.2 SURFACTANTS

For low wind speeds, the build-up of waves can be suppressed by using surfactants. These substances consist of both hydrophobic and hydrophilic groups, leading to their preferred placement at the air-water interface, with the hydrophilic groups in the water and their hydrophobic parts pointing away from it. As water can be considered being incompressible, and waves enlarge the water surface, they lead to con- and divergences within the water surface. In turn, this leads to a change in surfactant concentration. As surface tension is decreasing with the increased concentration of surfactants for many of these substances, concentration gradients lead to gradients in surface tension, giving rise to the so called Marangoni flow (Fernando [2013]). In the case of wave build-up, for example, stretching of the surface would be associated with a divergence of the surfactant layer, and thereby decrease its concentration. This would increase the surface tension and hence work against the divergence. In this manner the formation of waves is suppressed for low wind speeds and subsequent low shear stresses; for higher wind speeds, the effect of the surfactants will not be able to withstand the induced dynamics that are necessary for wave formation.

If the waves are suppressed, (2.2) simplifies further for the viscous boundary layer, as $\tau_{\text{wave},xz}$ can be neglected, i.e.

$$\tau_{\text{surfactant},\,xz}\big|_{z=0} = \tau_{\text{visc},\,xz}\big|_{z=0}\,. \tag{2.4}$$

2.3 Heat transport

The processes transporting heat, namely convection and radiative transport, will be discussed in the following section. Note that the term convection here refers to both advection and diffusion, which will be treated separately.

Advection

Advection describes the transport of a quantity or substance, by bulk motion. A fluid with temperature dependant density, for example, could experience a density driven flow if a part of it is heated. The associated transport of heat would then be referred to as advection.

Diffusion

Diffusion of heat, or thermal conduction, is heat transport by thermal movements and vibration of molecules, atoms and electrons. These exchange the energy through collisions with their neighbours, and the process can, in a isotropic medium and in the absence of advection, be described by Fick's 2. law:

$$\frac{\partial}{\partial t}T(\vec{x},t) = \alpha \Delta T(\vec{x},t), \tag{2.5}$$

with temperature T and thermal diffusivity α. The latter can be calculated from the following expression (Emmel [2017]):

$$\alpha = \frac{\kappa}{\rho \cdot c}, \tag{2.6}$$

with the thermal conductivity κ, density ρ and specific heat c of the medium.

Radiative transport

Heat is also transported through radiation. A black body with $T > 0$ emits radiation according to Planck's law, which states that the power emitted per unit area, per unit solid angle, per unit wavelength λ is described by the following expression:

$$L(\lambda, T) = \frac{2hc^2}{\lambda^5}(e^{\frac{hc}{\lambda k_{\mathrm{B}} T}} - 1)^{-1}, \tag{2.7}$$

where h is the Planck constant, c is the speed of light in the medium, and k_{B} the Boltzmann constant. $L(\lambda, T)$ is referred to as spectral radiance.

A black body absorbs all the incoming radiation. As real objects are not ideal black bodies, they absorb only a fraction $\alpha(\lambda)$, called spectral absorptivity, of incident radiation. According to Kirchhoff's law, any body in thermal equilibrium needs to emit and absorb the same amount of radiative energy for each wavelength,

$$\alpha(\lambda) = \epsilon(\lambda). \tag{2.8}$$

Real bodies therefore have wavelength dependant (spectral) emissivities $\epsilon(\lambda) < 1$. If an object has a spectral emissivity that is not wavelength dependant, ie. $\epsilon(\lambda) = \epsilon < 1$, the

object is called a grey body. Within the sensitive spectral range of the used camera (see section 5.1), water has a emissivity of $\epsilon \approx 0.97$ (Haußecker [1996]).

Incoming radiation onto a body can either be absorbed, transmitted or reflected. The (spectral) transmissivity $\tau(\lambda)$ and reflectivity $\rho(\lambda)$ can be defined in the same line as the absorptivity above; namely as the fraction of incident radiant flux that is transmitted and reflected, respectively. Due to conservation of energy, it follows that

$$\alpha(\lambda) + \tau(\lambda) + \rho(\lambda) = 1. \tag{2.9}$$

The transmittance after passing through Δz of a material with wavelength dependant penetration depth $\xi(\lambda)$ can be described with the Lambert-Beer law,

$$\tau(\Delta z, \lambda) = \frac{\Phi(\Delta z, \lambda)}{\Phi_0(\lambda)} = \exp\left(-\frac{\Delta z}{\xi(\lambda)}\right), \tag{2.10}$$

where $\Phi_0(\lambda)$ is the incoming spectral radiant flux, and $\Phi(\Delta z, \lambda)$ the flux remaining after passing through Δz.

2.4 Refraction

The speed of light in a medium, v, is given by:

$$v = c/n_{\text{med}}, \tag{2.11}$$

where c is the speed of light in vacuum and n_{med} is the refractive index in the medium. This means that when electromagnetic radiation passes from one medium to another, it may experience a change in the speed of light. As the frequency ν stays unchanged across the interface, the wavelength will need to change, specifically $\lambda_{\text{med}} = n_{\text{med}}\lambda_{\text{vac}}$.

The momentum $\vec{p}$ of a photon is proportional to its wave vector $\vec{k}$, that is, $|\vec{p}| \propto |\vec{k}| \propto 1/\lambda$, and it follows that

$$\vec{k}_{\text{med}} = n_{\text{med}}\vec{k}_{\text{vac}}. \tag{2.12}$$

Let θ_1 be the angle of incidence relative to the normal of the interface, and θ_2 the angle of refraction, that is, relative to the negative surface normal. The component of $\vec{k}$ normal to the interface needs to be conserved, ie. $|\vec{k}_1|\sin(\theta_1) = |\vec{k}_2|\sin(\theta_2)$. Inserting (2.12) yields Snell's law:

$$n_1 \sin\theta_1 = n_2 \sin\theta_2. \tag{2.13}$$

3 Active thermography

Using thermal imaging techniques in measurements is referred to as thermography, for temperatures around room temperature, this means that the detected radiation lies in the infrared. If additional sources of energy are used to emphasize the attribute of interest, the method is reffered to as active thermography.

The following work focuses on the determination of the velocity gradient in the viscous boundary layer, and hereby the related shear stress (equation (2.1)), using a method of active thermography. The approach is based on the work of Holtmann [2017], Emmel [2017] and Rembeck [2018].

3.1 Basic principle

By heating a thin line in the watersided boundary layer, perpendicular to the flow direction, the broadening of this line can be monitored. In the case of gentle heating, thus avoiding heat induced advection, and neglecting heat loss to the air and due to radiative transport, the broadening of the line is only due to diffusion. The loss to the overlying air is assumed neglectable, as its heat capacity is much lower than that of water, and there is a no-slip condition preventing mixing in the air sided boundary layer. Also the heat conductivity of air is low (Lide and Frederikse [1995]).

In the presence of a velocity gradient in the boundary layer, there will be an additional broadening relative to the case without. This can be illustrated in the case of a constant gradient with depth, a situation as shown in figure 2.1. As the heat profile is experiencing the gradient, it will "tilt" with time, see figure 3.1, hence enable an increased diffusive heat flow. For a better understanding of this, see figure 7.1 and 7.2. The width of the profile after a given time is therefore larger the higher the vertical gradient is, enabling for the assessment of this quantity by measuring the temperature profiles.

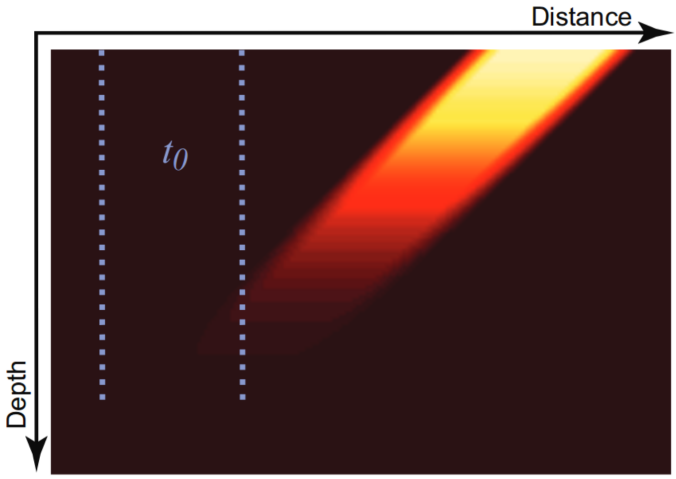

FIG 3.1.: Cross-section of heated line. The wind direction is from left to right, and the ordinate shows the depth. Due to the velocity gradient, the profile gets tilted with time. The dotted lines refer to the untilted shape of the profile immediately after heating. The figure is adapted from Garbe et al. [2007].

3.2 Earlier approach

The problem with a constant gradient with depth z, was analytically approached by Emmel [2017]. The outline will be briefly highlighted in the following section.

Let z be zero at the interface between air and water, and x the direction of the stationary flow

$$u(z) = u(z=0) + z \left.\frac{\partial u}{\partial z}\right|_{z=0}. \tag{3.1}$$

The temperature profile heated by the laser is assumed Gaussian, with width σ_0, and exponentially declining with z according to Lambert-Beer law (2.10):

$$T(x, z, t=0; \lambda) = \frac{a}{\sigma_0} \exp\left(-\frac{x^2}{2\sigma_0^2} - \frac{z}{\xi(\lambda)}\right) + T_0, \tag{3.2}$$

with T_0 being the temperature of the surrounding water, $\xi(\lambda)$ the penetration depth of the laser's radiation, and a/σ_0 the maximal amplitude of the temperature profile. The profile is assumed independent of the remaining spacial direction, y, i.e. parallel to the line, implicating an infinitely long line and hence no boundary effects. Consequently, there will be no heat flow along the line.

A closer look at (2.5) and realising that a additional term is needed for describing the advection associated with $u(z)$, yields for the temperature change of the profile:

$$\frac{\partial T(x,z,t)}{\partial t} = \alpha \left(\frac{\partial^2 T(x,z,t)}{\partial x^2} + \frac{\partial^2 T(x,z,t)}{\partial z^2}\right) - u(z)\frac{\partial T(x,z,t)}{\partial x}. \tag{3.3}$$

To solve this equation analytically, one might assume, based on symmetry considerations, that the temperature profile only depends on the difference $x - u(z)t$, with $u(z)$ from

(3.1). It follows:

$$\frac{\partial^2 T(x,z,t)}{\partial z^2} = \left(\frac{\partial u}{\partial z} t\right)^2 \frac{\partial^2 T(x,z,t)}{\partial x^2}. \tag{3.4}$$

This approximation neglects boundary effects due to the water surface, where the symmetry assumption is not fulfilled. It also assumes the amplitude of the profile to be independent of z, and hence no heat flux along the profile in z-direction.

Equation (3.4) can then be inserted into (3.3), and solved for a "δ-stripe-shaped" initial temperature distribution $T(x,z,t=0) \propto \delta(x)$. Thereafter, this solution is convolved with the initial temperature profile (3.2), yielding the final, gaussian shaped solution:

$$T(x,z,t;\lambda) = \frac{a}{\sigma(t)} \exp\left(-\frac{(x-u(z)t)^2}{2\sigma^2(t)} - \frac{z}{\xi(\lambda)}\right) + T_0, \tag{3.5}$$

with

$$\sigma(t) = \sqrt{\sigma_0^2 + 2\alpha t \left(\frac{1}{3}\left(\frac{\partial u}{\partial z}\right)^2 t^2 + 1\right)}. \tag{3.6}$$

3.3 Approach by simulation

As the earlier approach is based on the assumption (3.4), the validity of (3.5) is questionable. Especially since the temperature profile seen by the camera is located at the surface, this assumption is potentially leading to non-negligible deviations. In order to assess the system without neglecting the boundary effects, the described system is simulated numerically, with an additional component of the velocity gradients in y-direction. A total equation for the temporal change of the temperature profile, still neglecting heat induced advection, heat loss to the air and radiative transport of heat, is therefore given by the diffusion-advection equation:

$$\frac{\partial T(x,y,z,t)}{\partial t} = \alpha\left(\Delta T(x,y,z)\right) - u(y,z)\frac{\partial T(x,z,t)}{\partial x}, \tag{3.7}$$

with

$$u(y,z) = u(y=y_0, z=0) + z\left.\frac{\partial u}{\partial z}\right|_{y=y_0,z=0} + (y-y_0)\left.\frac{\partial u}{\partial z}\right|_{y=y_0,z=0}, \tag{3.8}$$

with an arbitrary reference point y_0. The implementation is explained in the next chapter.

4 Simulation

In the following chapter, the background and implementation of the problem introduced in chapter 3 is discussed. The denotation used there, is adapted in the following. All programming was done in Python.

4.1 Idea

The volume of the viscous boundary layer to be simulated will be divided into voxels with unequal side lengths Δx_i. This volume then undergoes

- a heating step as long as the laser is on,
- a diffusion step,
- a shift of the volume in x-direction corresponding to the shear flow.

The gradient of the stationary velocity $u(y, z)$ is constant, with components in y- and z-direction. To save as much computational effort as possible, the number of voxel slices in y-direction is set to three. Further on, in the case of no gradient parallel to the heated line, i.e.

$$\frac{\partial u}{\partial y} = 0, \tag{4.1}$$

the y dimension is omitted. As the heated line is assumed homogeneous in this direction, no net heat flux will occur along the line and hence the two dimensional representation of the system is fully descriptive.

4.2 Heating step

The temperature profile (3.2) corresponds to a infinitely fast heating, as it does neither account for diffusion whilst the laser is on, nor the shear in the flow. Assuming a laser profile that is Gaussian in x-direction around x_0, and box-shaped in y centred about y_0, corresponding to a segment of length δy of the laser line, it follows for the irradiance flux E hitting the surface:

$$E(x, y) = \frac{P_l}{\sqrt{2\pi}\sigma_0} \exp\left(\frac{(x - x_0)^2}{2\sigma_0^2}\right) \cdot \left[\Theta(y - y_0 + \frac{\delta y}{2}) - \Theta(y - y_0 - \frac{\delta y}{2})\right], \tag{4.2}$$

where P_l is the power per unit length in y-direction emitted from the laser, and $\Theta(y)$ the Heaviside step function. This flux is then deposited in the water, with penetration depth $\xi(\lambda)$, and thereby heating it. The change in temperature ΔT per time step Δt is given by:

$$\Delta T(x, y, z; \lambda) = \frac{E(x, y) \cdot \Delta t}{\xi(\lambda) \rho c_V} \exp\left(-\frac{z}{\xi(\lambda)}\right), \tag{4.3}$$

where ρ is the density of the water and c_V its specific heat. $\xi(\lambda)$ shows up in the denominator of the prefactor due to normalization, and its necessity is also evident due to dimensional reasons.

In the discrete case of the simulation, ΔT corresponds to a matrix of same dimensions as the simulation volume. As the heating time $t_{\text{laser on}}$ in the real application is longer than the time step size Δt, heating for several time steps are needed. In the case that $t_{\text{laser on}}$ is not a multiple of Δt, the last heating step corresponds to a smaller $\Delta t_{\text{reminder}} < \Delta t$. It is therefore convenient to calculate $\Delta T / \Delta t$ once, and reuse it for each time step the laser is turned on.

Note that, as explained later in section 4.4, that the flow velocity at the interface between air and water, is implemented as zero. This means that the realistic case with a certain degree of surface movement whilst heating, is neglected. This leads to a slightly different width and shape of profile; the width poses no problem as it is measured in the real-world application and then compared to the simulation.

4.3 Diffusion step

For simulating the diffusion, and hence the broadening of the temperature profile, convolutions of the simulation volume with binomial- or other reasonable masks are performed. This idea is adapted from Haußecker [1996].

4.3.1 Diffusion in fourierspace

To realize that a convolution with a binomial mask indeed corresponds to a realistic diffusion process, a closer look at the fourier transform and its impact when applied to Fick's 2. law (2.5) is illustrative.

Before transforming the diffusion equation, a couple of properties of the Fourier transform needs to be introduced. Let $\hat{f}(\vec{k}) := \mathcal{F}\{f(\vec{x})\}_{\vec{k}}$ denote the fouriertransform of the integrable function $f(\vec{x})$, ie.

$$\hat{f}(\vec{k}) = \frac{1}{\sqrt{2\pi}^3} \int_{\mathbb{R}^3} f(\vec{x}') \exp\left(-\mathrm{i}\vec{k}\vec{x}'\right) \mathrm{d}\vec{x}'. \tag{4.4}$$

The inverse transform $\mathcal{F}^{-1}\{\hat{f}(\vec{k})\}_{\vec{x}} = f(\vec{x})$ is then defined analogously, differing from (4.4) only by the opposite sign in the exponent. The first and second derivatives of $f(\vec{x})$ with respect to dimension x_i can be expressed with the corresponding k_i in Fourier space, namely

$$\frac{\mathrm{d}}{\mathrm{d}x_i} f(\vec{x}) = \frac{\mathrm{d}}{\mathrm{d}x_i} \mathcal{F}^{-1}\{\hat{f}(\vec{k})\}_{\vec{x}} = \mathrm{i}k_i \mathcal{F}^{-1}\{\hat{f}(\vec{k})\}_{\vec{x}} \tag{4.5}$$

and

$$\frac{\mathrm{d}^2}{\mathrm{d}x_i^2} f(\vec{x}) = \frac{\mathrm{d}^2}{\mathrm{d}x_i^2} \mathcal{F}^{-1}\{\hat{f}(\vec{k})\}_{\vec{x}} = -k_i^2 \mathcal{F}^{-1}\{\hat{f}(\vec{k})\}_{\vec{x}}. \tag{4.6}$$

Taking the Fourier transform of the latter equation, yields the desired result:

$$\mathcal{F}\left\{\frac{\mathrm{d}^2}{\mathrm{d}x_i^2} f(\vec{x})\right\}_{\vec{k}} = -k_i^2 \hat{f}(\vec{k}). \tag{4.7}$$

Having the necessary tool for the following consideration, the Fourier transform of (2.5) can be computed:

$$\frac{\partial}{\partial t}\hat{T}(\vec{k},t) = \alpha \mathcal{F}\left\{\sum_i \frac{\partial^2}{\partial x_i^2} T(\vec{x},t)\right\}_{\vec{k}} \overset{(4.7)}{=} -\alpha \vec{k}^2 \hat{T}(\vec{k},t). \tag{4.8}$$

This shows that the transfer function of the Laplacian operator Δ is isotropic, i.e. $\Delta \circ\!\!-\!\!\bullet\ -k^2$, which is as expected based on its involvement in the diffusion equation. Solving (4.8) yields with respect to time:

$$\hat{T}(\vec{k},t) = \hat{T}_0(\vec{k}) \exp(-\alpha \vec{k}^2 t). \tag{4.9}$$

So, in Fourier space, diffusion act on the initial temperature distribution $\hat{T}_0(\vec{k})$ by multiplying it with a Gaussian. Due to the convolution theorem (Jähne [2012a]),

$$\mathcal{F}\{(f * g)(\vec{x})\}_{\vec{k}} = \sqrt{2\pi}^3 \hat{f}(\vec{k}) \cdot \hat{g}(\vec{k}), \tag{4.10}$$

a convolution $(f * g)(\vec{x})$ in real space corresponds to a multiplication in Fourier space. Hence, taking the inverse transform of (4.10) and applying it on (4.9), also considering the commutativity of convolutions, this yields that

$$T(\vec{x},t) = \frac{1}{\sqrt{2\pi}^3} \cdot \frac{1}{\sqrt{2\alpha t}^3} \exp\left(\frac{-\vec{x}^2}{4\alpha t}\right) * T_0(\vec{x}). \tag{4.11}$$

This result shows that by convolving the inital temperature distribution with a Gaussian of width (in each dimension) $\sigma^2 = 2\alpha t$, the temporal effect of diffusion can be calculated. This property will later be used for finding a suitable, discrete operator for approximating $T(\vec{x},t)$ from earlier time steps of the simulation.

4.3.2 Discretization of Fick's 2. law

Starting from equation (4.8), it is time to discretize Fick's 2. law (2.5) and finally arrive at a computational effective implementation. In the following i, j and k refer to the grid cell indices of the simulated volume in x, y and z direction, respectively. It should also be noted, that the lengths of cubic grid cells are not assumed equal for the different spacial dimensions, leading to an inhomogeneous grid.

A Taylor expansion of the temporal development of the temperature in a grid cell

leads to:

$$T_{i,j,k}(t+\Delta t) = T_{i,j,k}(t) + \Delta t \frac{\partial T_{i,j,k}(t)}{\partial t} + \frac{1}{2}(\Delta t)^2 \left(\frac{\partial^2 T_{i,j,k}(t)}{\partial t^2} \right) + ..., \tag{4.12}$$

and hence for the temporal derivative:

$$\frac{\partial T_{i,j,k}(t)}{\partial t} = \frac{T_{i,j,k}(t+\Delta t) - T_{i,j,k}(t)}{\Delta t} + \mathcal{O}(\Delta t). \tag{4.13}$$

As Δt is small, the first term becomes dominant, preventing the order of $\mathcal{O}(\Delta t)$ becoming a problem.

To ease the following derivation, only one spacial dimension x is considered. Introducing the yet unknown (one dimensional) discrete Laplacian operator $\boldsymbol{L}_x$ and using the result of (4.13), (2.5) can be discretized as

$$\frac{T_i(t+\Delta t) - T_i(t)}{\Delta t} = \alpha \frac{\partial^2}{\partial x^2} T_i(t) =: \alpha \boldsymbol{L}_x T_i(t), \tag{4.14}$$

and then rewritten:

$$T_i(t+\Delta t) = (\boldsymbol{I}_x + \alpha \Delta t \boldsymbol{L}_x) T_i(t), \tag{4.15}$$

with $\boldsymbol{I}_x$ being the identity operator.

Turning to the right hand side of (4.14), the need for discrete realization of the Laplacian arises. It should be repeated here that the goal is to arrive at a mask which, when convolved with the inhomogeneous grid, results in a homogeneous diffusion. So, still considering the one dimensional case, the temperature value of the two neighbouring grid cells of cell i can be approximated as:

$$T_{i\pm1}(t) = T_i(t) \pm \Delta x \left(\frac{\partial T_i(t)}{\partial x} \right) + \frac{\Delta x^2}{2} \left(\frac{\partial^2 T_i(t)}{\partial x^2} \right) \pm ... \, . \tag{4.16}$$

By adding the expressions for T_{i-1} and T_{i+1}, the first spacial derivatives cancel, leaving an expression for the second derivative:

$$\frac{\partial^2 T_i(t)}{\partial x^2} = \frac{T_{i-1}(t) - 2T_i(t) + T_{i+1}(t)}{\Delta x^2} + \mathcal{O}(\Delta x^2). \tag{4.17}$$

This second order approximation is known as the *finite differences* method. Comparing with (4.14), one find:

$$(\boldsymbol{I}_x + \alpha \Delta t \boldsymbol{L}_x) T_i(t) = \beta T_{i-1}(t) + (1-2\beta) T_i(t) + \beta T_{i+1}(t), \tag{4.18}$$

with

$$\beta_x = \frac{\alpha \Delta t}{\Delta x^2}. \tag{4.19}$$

This corresponds to a convolution of the discrete $T(t)$ with the mask $\boldsymbol{M}_x = [\beta, 1-2\beta, \beta]$. Further on, from (4.19) follows that the magnitude of the time step and grid cell size are closely connected, with higher values of β_x being favourable as this gives the longest time step for given Δx. $\beta_x \leq 1/2$ is a necessary condition for avoiding that more heat flows out of grid cell i, than what is contained in it. Another issue is numerical stability,

as β_x=1/2 represents the critical value before issues with numerical instabilities develop (Crank [1975]). $\beta_x = 1/4$ yields the binomial mask, is stable, and thus the highest value of β_x used in the implementation of the simulation.

It is now time to turn to the higher dimensional case. From (4.9) follows that

$$\hat{T}(\vec{k}, t) = \hat{T}_0(\vec{k}) \exp(-\alpha k_x^2 t) \exp(-\alpha k_y^2 t) \exp(-\alpha k_z^2 t), \tag{4.20}$$

and hence, by applying the convolution theorem (4.10), three dimensional mask can be obtained by convolving the three one dimensional masks, that is,

$$\boldsymbol{M} = \boldsymbol{M}_x * \boldsymbol{M}_y * \boldsymbol{M}_z. \tag{4.21}$$

This leads to the final discrete formulation of (2.5):

$$T(t + \Delta t) = \boldsymbol{M} * T(t). \tag{4.22}$$

The non-cubic grid cells leads to anisotropic diffusion, if the mask used is isotropic. Note that $\boldsymbol{M}$ is anisotropic as required, since β is adjusted according to the grid cell size in the corresponding direction. It should also be mentioned that, even though starting with the method of finite differences, (4.21) is not equivalent to the 3D operator of this method, and a better discrete realisation of (4.11). This will be discussed below.

In the two dimensional case discussed in section 4.1, $\boldsymbol{M}_y$ is simply omitted in (4.21). Exploiting the convolution theorem (4.10), the convolution in (4.22) can be replaced by a multiplication in Fourier space. Because multiplications are far less expensive than convolutions (Jähne [2012a]), and with the use of fast Fourier transforms for affordable forth- and back transformation, the computational effort of (4.22) is reasonable. A closer look at (4.21) reveals further advantages, due to the associative property of the convolution and the separability of $\boldsymbol{M}$:

$$\boldsymbol{M} * T(t) = (\boldsymbol{M}_x * \boldsymbol{M}_y * \boldsymbol{M}_z) * T(t) = \boldsymbol{M}_x * (\boldsymbol{M}_y * (\boldsymbol{M}_z * T(t))). \tag{4.23}$$

By successively convolving the volume with the one dimensional masks, the computational expense is additionally reduced.

As a final note, it can be mentioned that (4.22) implies that the solution after n time steps can be obtained by first convolving $\boldsymbol{M}$ n times, and then with $T(t)$. In the case of the simulation, this is not possible, as the velocity gradients in the flow add more terms to Fick's 2. law, as described by (3.7).

The mask $\boldsymbol{M}$ compared to the method of finite differences

As already mentioned, $\boldsymbol{M}$ yields a better approximation than what is obtained from the finite differences, and is therefore the method of choice. Why this can be claimed, will be discussed for the 2D case.

It is illustrative to recall the right hand side of (4.9), i.e. the solution of the diffusion equation in Fourier space, stating the multiplication of the initial distribution $\hat{T}_0(\vec{\kappa})$ with a Gaussian, that is, $\exp(-\beta\kappa^2) = 1 - \beta\kappa^2 + \mathcal{O}(\kappa^4)$. For a discrete realisation of this equation, the transfer function of the operator should approximate the this Gaussian. In the following, $\Delta x = \Delta y$ for simplicity and demonstrative purpose, meaning that $\beta_x = \beta_y = \beta$.

Starting with the finite differences method, a 2D version of (4.18) can be obtained in

an analogous manner, yielding:

$$T(t+\Delta t) = \begin{bmatrix} 0 & \beta & 0 \\ \beta & 1-4\beta & \beta \\ 0 & \beta & 0 \end{bmatrix} * T(t) =: \boldsymbol{A} * T(t). \tag{4.24}$$

The transfer function can then be computed, setting $\kappa_{x_l} = 2\pi k_{x_l}/N$:

$$\begin{aligned} \hat{\boldsymbol{A}}(\kappa_x, \kappa_y) &= \sum_m \left[\sum_n A_{m,n} \exp\left(-\mathrm{i}\kappa_x n\right) \right] \exp\left(-\mathrm{i}\kappa_y m\right) \\ &= 2\beta(\cos(\kappa_x) + \cos(\kappa_y)) + 1 - 4\beta = 1 - \beta\kappa_x^2 - \beta\kappa_y^2 + \mathcal{O}(\kappa^4). \end{aligned} \tag{4.25}$$

Hence, for small wavenumbers κ, $\boldsymbol{A}$ indeed behaves isotropic as expected.

$\boldsymbol{M}_{xy}$, the two dimensional version of the mask from (4.22), i.e.

$$\boldsymbol{M}_{xy} = \begin{bmatrix} \beta^2 & \beta(1-2\beta) & \beta^2 \\ \beta(1-2\beta) & (1-2\beta)^2 & \beta(1-2\beta) \\ \beta^2 & \beta(1-2\beta) & \beta^2 \end{bmatrix}, \tag{4.26}$$

with the transfer function

$$\hat{\boldsymbol{M}}_{xy}(\kappa_x, \kappa_y) = \left(1 + \beta\cos\left(\kappa_x\right) - 2\beta\right)\left(1 + \beta\cos\left(\kappa_y\right) - 2\beta\right) = 1 - \beta\kappa_x^2 - \beta\kappa_y^2 + \mathcal{O}(\kappa^4), \tag{4.27}$$

is also isotropic for small wavenumbers κ. $\boldsymbol{M}_{xy}$ becomes the two dimensional binomial mask of degree two, ${}^2\mathcal{B}_{xy}$, when evaluated for $\beta = 1/4$, as was also the case in 1D, and this holds for 3D as well.

This means that both masks perform as expected as long as κ is small. For $\beta = 1/4$ and larger κ, however, finite differences ($\boldsymbol{A}_{xy}$) yields a more anisotropic transfer function, whereas the binomial mask is performing better and stays a fairly good approximation of the isotropic Gaussian in (4.9), see figure 4.1. This is altered when decreasing β, since both methods converge to the same mask.

It should be mentioned that $\beta = 1/4$ is a critical value for the method of finite differences, as the mask of (4.24) becomes zero for the center element. Considering that larger values of β are favourable, as earlier discussed, this also points towards the choice of $\boldsymbol{M}_{xy}$.

An analogous analysis for the 3D case also finds ${}^2\mathcal{B}_{xyz}$ as the appropriate choice of mask, but is harder to visualize. Summarized, due to the better isotropy and meaningful results for $\beta = 1/4$, the mask of choice for the simulation is $\boldsymbol{M}$.

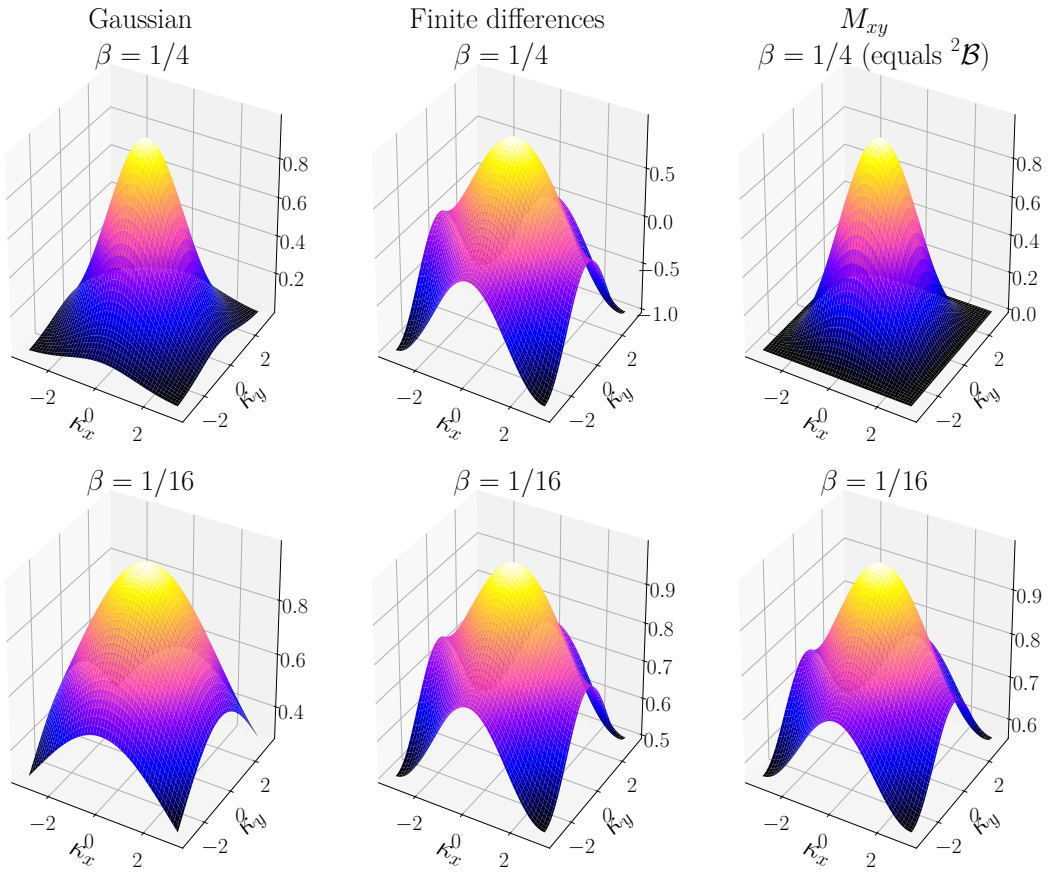

FIG 4.1.: The transfer functions of the ideal (Gaussian) operator $\exp(-\beta k^2)$ (left), the method of finite differences (FD, middle) and the discussed mask $\boldsymbol{M}_{xy}$ (right), for the values of $\beta = 1/4$ (above) and $\beta = 1/16$ (below). Note the different scale of the vertical axes. For $\beta = 1/4$, the binomial mask $^2\mathcal{B}$ represents a fairly isotropic realization of the Gaussian, whereas the FD operator is anisotropic and the value of β is critical. In the case of $\beta = 1/16$, both FD and $\boldsymbol{M}_{xy}$ are anisotropic for large κ and also of similar shape, as the masks approach each other for $\beta \to 0$.

4.4 Shifting step

As given by the diffusion-advection equation (3.7), there is a temporal change of the temperature distribution associated with the flow. Only the boundary layer is simulated, implying that the velocity gradient assumed is constant at all depths. The implementation differs slightly depending on whether the velocity gradients are with respect to y- or z-direction. This is a consequence of different boundary conditions in the two cases.

The following relations between grid cell indices i, j and k and real world coordinates x, y and z, respectively, are used:

$$x = i\Delta x,\ \ y = j\Delta y \text{ and } z = -k\Delta z. \tag{4.28}$$

Shear in z-direction

The flow velocity is taken as zero at the interface between air and water, as are the grid cell indices k with respect to depth. The deeper layers are then shifted by δi in x-direction according to the velocity gradient;

$$\delta i(k) = i(k, t + \Delta t) - i(k, t) = \frac{\partial u}{\partial z} \cdot k\Delta z \cdot \frac{\Delta t}{\Delta x}, \tag{4.29}$$

hence all cells at a certain depth are shifted by an equal amount. Because the flow is stationary, this shift is independent of time. In general, δi is not an integer. It is possible to wait several time steps with the shift until it amounts to more than a half index, but this is a suboptimal solution becoming noticeable when the system is challenged. The better approach is interpolation of the between each time step, in which the values of the to be shifted cells are first interpolated, and then evaluated at the shifted coordinates. In the actual implementation cubic spline interpolation where chosen, using a built-in function for shifting the arrays. Points outside of the original arrays, i.e. those moving into the simulated volume, were filled with the surrounding temperature T_0.

Shear in y-direction

As will be explained in the next section, the implementation of the shift of the volume due to velocity gradients in y-direction, is slightly more complicated than that of (4.29). Recall the extension $N_y = 3$. All cells with $j = j_0 = 1$ are not shifted, hence they represent y_0 in equation (3.8) for the flow $u(y, z)$. Due to the symmetry of the problem, all the three slices $j \in 0, 1, 2$ of the volume, are, except for a displacement in their x-coordinate, identical. At time step n, their shift relative to the slice j_0 is given by:

$$\delta i(j, n) = i(j, t_0 + n\Delta t) - i(j, t_0) = \frac{\partial u}{\partial y}(j - j_0) \cdot \Delta y \cdot \frac{n\Delta t}{\Delta x}. \tag{4.30}$$

Note that an equation analogues to this (notice n time steps) cannot be applied instead of (4.29) for the z-direction, as the different layers k are non-identical.

The implementation of the shift in y is implemented by the use of (4.30), effectively meaning that the slice j_0 of the simulated volume is copied and pasted in a shifted version according to $\delta i(j, n)$, for all $j \neq j_0$. Also here cubic spline interpolation is used, and missing values due to the shift filled with the surrounding temperature T_0.

4.5 Boundary conditions

Regarding the boundaries of the simulated volume, the heat flux through the air-water interface is neglected, corresponding to a no-flow (Neumann) boundary condition. As there is no component of the flow $u(y, z)$ flowing through this interface, only diffusion can contribute to a heat flux through this surface. This is simply realised by implementing the convolution resulting in the diffusion (see section 4.3.2) with mirror symmetric boundaries. This means that the values of the grid cells at the border are mirrored about the edge, hence being symmetric with respect to it. In the case the mask extends into these mirrored values, no net heat flux will occur. This can be thought of as two mirror symmetrical and otherwise identical objects, having the same temperature

distribution, being put together at their corresponding interface. Obviously, no heat flux over the boundary will take place.

For the case with no shear in y-direction, no heat flow will take place parallel to the line (i.e. the y-direction). This means that reflective boundaries would be a option here too, but it is computationally more efficient to lower the dimension of the simulated volume, and thereby only calculate the two dimensional diffusion in the remaining directions.

In the case of $\partial u/\partial y \neq 0$, the implementation with no-flow conditions in the y-direction, is incorrect, as the line is no longer parallel to y and there will be a heat flux. Mirrored boundaries including a shift analogous to (4.30) would yield the wanted result, but are in practice difficult to implement by using built-in functions. A solution to this is to convolve the simulated volume as normal, irrespective to which mode of boundary handling that is used. Of the three slices ($j = 0, 1, 2$) in y-direction, the middle one has experienced a realistic diffusion as the convolved mask also has the dimension $N_{y,\text{mask}} = 3$, and therefore is unaffected by boundary effects. The slices $j = 0$ and $j = 2$ can be discarded, and replaced by the $j = 1$ slice shifted according to (4.30). The next time step, the middle slide will again experience a representational diffusional behaviour, and the process can be repeated.

For the remaining boundaries of the simulation volume, heat flux may take place. This would correspond to a convolution where the volume is extended beyond the edges with the surrounding temperature T_0, but this is difficult to obtain with built-in functions simultaneously with the mirrored boundary conditions needed above. This is solved by keeping the outermost grid cells at T_0, i.e. a Dirichlet boundary condition, yielding the wanted heat flow out of the volume along these edges.

4.6 The observed temperature profile

As the simulation of the temperature distribution is now available, the actual observed profile when looking at the surface from above, needs to be discussed. In order to save computational time, the temperature profiles were only evaluated every 50 ms of the simulated time.

The most simple case would be to just observe the temperature at the interface, that is, return only the upper layer of the simulated volume. But, as discussed earlier, water is transmissible by electromagnetic radiation. This means that deeper layers also contribute to the observed profile, and thereby should be considered. See figure 4.2 for a sketch showing the central elements in the following consideration.

According to the Lambert-Beer law (2.10), the length of the optical path matters, also meaning that the angle of observation θ_a influences the seen signal. According to Snell's law (2.13), the corresponding angle of refraction θ_w, that is, the water sided observation angle, is given by

$$\theta_w = \arcsin\left(\frac{n_a}{n_w}\sin(\theta_a)\right). \tag{4.31}$$

Now, for a water layer of thickness z, the transmitted radiation passing through this layer at an angle θ_w relative to the normal of the layer, is given by the Lambert-Beer

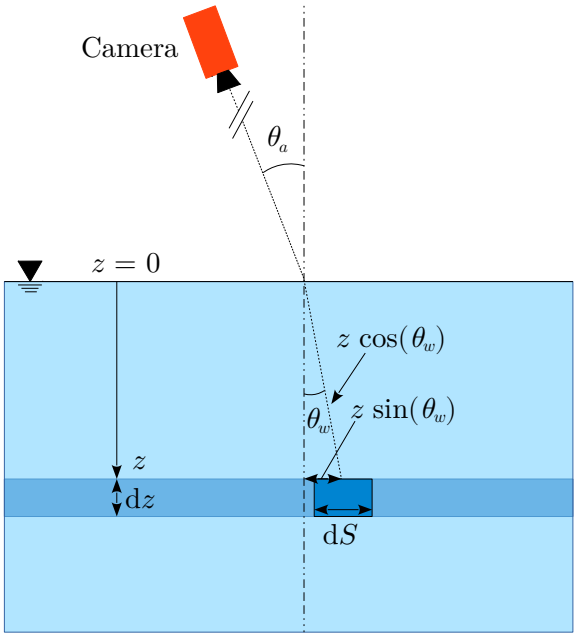

FIG 4.2.: Sketch for calculating the observed temperature profile. The camera plays the role as the observer.

law:

$$\tau(z;\lambda) = \exp\left(-\frac{z}{\cos(\theta_w)\xi(\lambda)}\right). \tag{4.32}$$

There will be no inner reflections within that layer, as the braking index does not change. This yields, by recalling Kirchhoff's law (2.8) and combining it with (2.9), for the emissivity at depth z:

$$\epsilon(z;\lambda) + \tau(z;\lambda) + \underbrace{\rho(z;\lambda)}_{=0} = 1, \tag{4.33}$$

and hence

$$\epsilon(z;\lambda) = 1 - \tau(z;\lambda) = 1 - \exp\left(-\frac{z}{\cos(\theta_w)\xi(\lambda)}\right). \tag{4.34}$$

$\epsilon(z;\lambda)$ is the result of all thin layers of thickness $\mathrm{d}z$, see figure 4.2, that the radiation has passed through. The contribution to from each of these layers can be obtained by differentiating (4.34) with respect to z:

$$\mathrm{d}\epsilon = \frac{1}{\cos(\theta_w)\xi(\lambda)} \exp\left(-\frac{z}{\cos(\theta_w)\xi(\lambda)}\right) \mathrm{d}z. \tag{4.35}$$

$\mathrm{d}\epsilon$ is referred to as the differential emissivity, an idea adapted from Haußecker [1996]. This is now giving the opportunity to express the (differential) spectral intensity $\mathrm{d}I_\lambda(z = 0)$ (unit W/(sr m)) reaching the surface $z = 0$, emitted form a thin layer at depth z, and hence express the total spectral intensity seen by the observer in the solid angle element $\Delta\Omega_a$ with angle θ_a to the surface normal, in terms of an integral over the thin layers

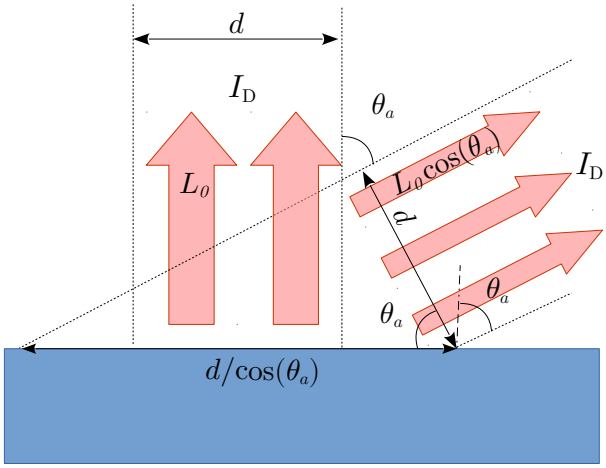

FIG 4.3.: Sketch of the Lambertian surface. The extent from which the detector receives the radiation is d. As the figure shows, the part of the surface seen by the observer at an angle θ_a is increased by $1/\cos(\theta_a)$, where as the radiance is reduced by $\cos(\theta_a)$, relative to the case with the observer normal to the surface. The effects thereby cancel, and the received intensity by the detector, hence the brightness, is equal in the both cases.

(Haußecker [1996]):

$$I_\lambda(z=0) = \int_z \mathrm{d}I_\lambda(z=0) = \int_z I_\lambda(z)\mathrm{d}\epsilon. \tag{4.36}$$

However, the thin layers are not homogeneous in temperature with respect to the horizontal dimensions, and the interesting quantity is exactly this non-uniform distribution. Therefore, it is beneficial to modify the approach by Haußecker [1996] and hereby partition the horizontal layers into infinitesimal pieces $\mathrm{d}S$, and reformulate (4.36) accordingly. The appropriate quantity for this purpose, is the spectral radiance $L(T,\lambda)$ (unit $\mathrm{W}/(\mathrm{m}^2$ sr m)), described by the Planck curve (2.7). The corresponding formulation of (4.36) becomes for the spectral intensity reaching the surface element of the detector $\mathrm{d}S_\mathrm{D}$:

$$\frac{\mathrm{d}I_\lambda(x,z=0)}{\mathrm{d}S_\mathrm{D}} \propto \int_z L(T(x+z\sin(\theta_w),z);\lambda)\mathrm{d}\epsilon. \tag{4.37}$$

As constants only changes the magnitude of this quantity, and not its shape, and the latter is of interest, these are ignored. Note that due to the watersided angle of observation θ_w, the horizontal coordinates of the to be considered fluid element varies with depth. Further on, surface appears equally bright irrespectively of the angle of observation θ_a. This is because that even though the (assumed Lambertian) surface only radiates the fraction $\cos(\theta_a)$ of the intensity normal to the surface towards the observer, the observer sees the enlarged fraction $\mathrm{d}S_\mathrm{D}/\cos(\theta_a)$ of the surface. Hence, the effects cancels, see figure 4.3 for a sketch.

The detector is sensitive to wavelengths in the interval $[\lambda_1,\lambda_2]$, hence leading to a integral over this spectral range. Putting it all together yields:

$$\frac{\mathrm{d}I(x,z=0)}{\mathrm{d}S_\mathrm{D}} \propto \int_{\lambda_1}^{\lambda_2}\int_0^{z_\mathrm{max}} \frac{L(T(x+z\sin(\theta_w),z),\lambda)}{\xi(\lambda)} \exp\left(-\frac{z}{\cos(\theta_w)\xi(\lambda)}\right)\mathrm{d}z d\lambda. \tag{4.38}$$

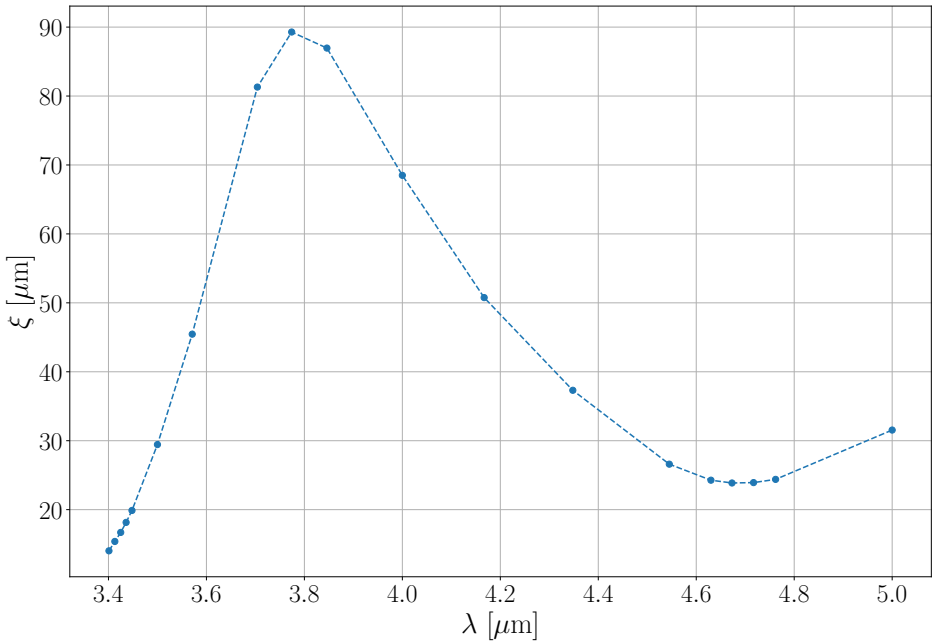

FIG 4.4.: Plot of penetration depth in water $\xi(\lambda)$ for λ between 3.4 and 5 μm for 27°C. This corresponds to the sensitive range of the used IR camera, see section 5.1. The values are taken form Downing and Williams [1975].

As the units of the above expression can tell, this is a directional quantity given per unit solid angle $\Delta\Omega$. It is in the following assumed that $\Delta\Omega$ is the same for all parts of the signal, meaning that the direction of observed radiation is independent of x, and hence the calculated values for different parts of the signals are directly comparable. This approximation can be done since the distance between the fluid element and the (small) detector is much larger than both the horizontal extent of the signal and the extinction coefficient $\xi(\lambda)$ for relevant λ, see figure 4.4.

As the measured quantity is a temperature, (4.38) now needs to be compared to the equivalent expression of a water body that would have a homogeneous temperature T_c, that is, setting $T(x, z) = T_c$ and then match the results. It turns out that $\mathrm{d}I_{z=0}(T_c)/\mathrm{d}S_\mathrm{D}$ of equation (4.38) is well approximated as a linear function $f(T_c) = aT_c + b$ within the small temperature range of the heated profile, see figure 4.5. Being easily invertible, this finding enables a straight forward mapping from (4.38) to temperature. Note that, as only the width of the temperature profile is of interest, this mapping is strictly speaking not necessary; due to the linear relationship, the profile not altered with respect to its shape.

In the case of the simulation, (4.38) needs to be discretized. The integration is performed using the midpoint quadrature. Further on, for evaluating $T(x + z\sin(\theta_w), z)$, the best approach would be to interpolate it and then evaluate it at the respective point. That being said, as Δx is small, the error committed by just using the value of the respective grid cell is small, and it saves computational effort. In the actual implementation, the latter approach is chosen. As the detector is fixed, θ_a and hence also θ_w are constant, a matrix with entries 1 for the to be evaluated grid cell at depth k, and entries of 0 elsewhere, can be precomputed. This matrix can then be multiplied with the

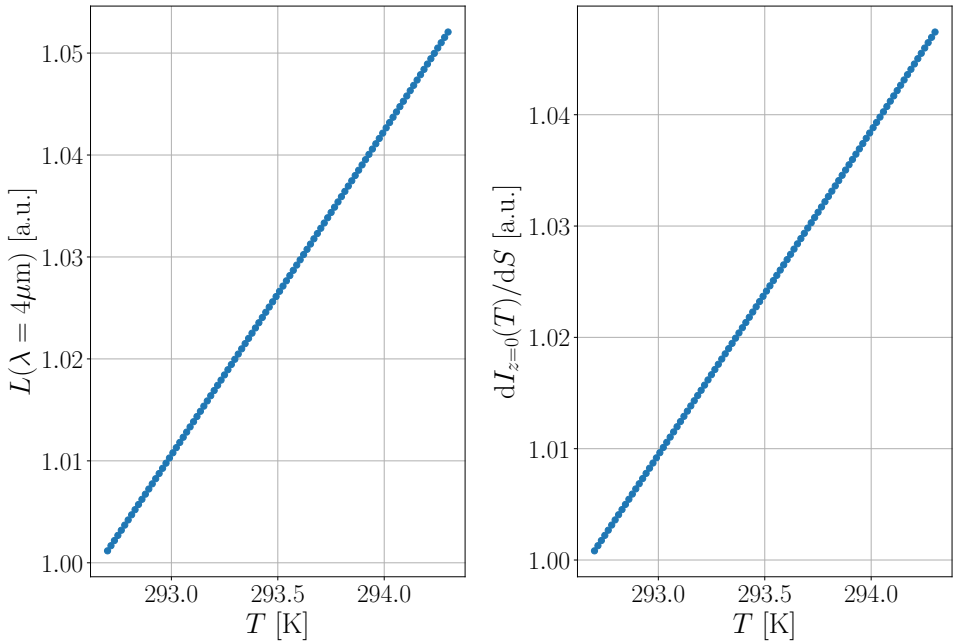

FIG 4.5.: Plot of equation (2.7) (left) and (4.38) (right) for a small temperature range around 20.5°C. For the first equation, the temperature profile was independent of the spacial coordinates. This plot justifies the linear approximations made in section 4.6.

volume at the wanted horizontal positions for efficient evaluation of the temperatures with depth. Also the exponential function in (4.38) can be precomputed for discrete values of λ.

With the perspective of the method of this work being applied, it is of interest to compare (4.38) to more easily applicable approximations. The first approximation considered is using the temperature profile directly at the surface, without taking deeper layers into account.

The second approach is to assume θ_w small enough to be neglected in the expression $x + z\sin(\theta_w)$ in (4.38), hence consider only vertical columns when integrating, and additionally replace the integral over λ by assuming a mean penetration depth ξ_{mean}, ie.

$$T_c(x) = \int_0^{z_{\max}} \frac{T(x,z)}{\xi_{\text{mean}}} \exp\left(-\frac{z}{\xi_{\text{mean}}}\right) \mathrm{d}z. \tag{4.39}$$

Notice that the expression for the Planck curve (2.7) was replaced by a linear approximation with temperature, see figure 4.5 for a plot, hence making the Lambert Beer law applicable to the temperature directly.

5 Setup and measurements

5.1 Setup

In this section, the used setup and wind-wave facility will be presented.

The Aeolotron

The experiments were conducted at the Aeolotron, an annular wind-wave facility (see figure 5.1 for schematic), with an outer diameter of approximately 10 m and a mean width of the channel of about 62 cm (Emmel [2017]). Further on, the height is 240 cm, of which about (100 ± 2) cm were filled with water during the experiments. The water volume hence approximates to 18 m^3. As the walls of the flume are isolated, the air- and water temperatures were stable for the duration of the measurements.

The wind is driven by four evenly distributed axial ventilators, controlled with a frequency between 0 and 50 Hz. In the following, wind speeds are expressed in terms of this frequency, as it is hard to define one appropriate reference wind speed for the whole facility, as the wind field is inhomogeneous (Bopp [2014]) and influenced by secondary flows due to boundary effects and the annular shape. The wind profile is not logarithmic. For a rough comparison between the wind generator frequencies used in this work, and the corresponding wind velocity u_{10} at 10 m height, see table 5.1. These values were given by Maximilian Bopp, and were obtained without the surfactant used in the experiments, hence there could be further discrepancies.

Surfactant

The measurements were carried out using the non-ionic surfactant Triton X-100. About 60 g of this substance were added to the water (yielding 3.3 mg/L), enough to suppress the waves at all considered wind speeds.

Wind generator frequency [Hz]	u_{10} [m/s]
5.0	2.4 ± 0.2
7.5	3.7 ± 0.2
10.0	4.8 ± 0.3
12.5	6.1 ± 0.4
15.0	7.3 ± 0.4

Table 5.1.: The approximate relations between the wind generator frequency and reference wind speed at 10 m height u_{10}. The 15 Hz setting was only used for a faster built-up of the wind field, see section 5.3. Values by M. Bopp.

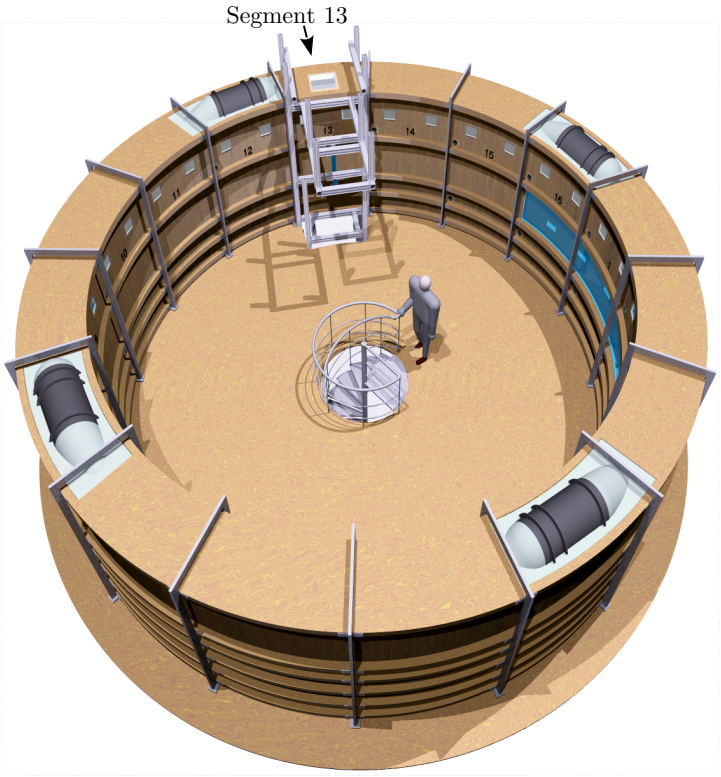

FIG 5.1.: Schematic of the Aeolotron. The experiment was conducted at segment 13, where the optical access is located. Modified from Krall [2013].

NIR-Laser system

The laser used for heating the line on the surface, emits in the near infrared (NIR) part of the electromagnetic spectrum. As described in Rembeck [2018], who used the same laser set up, the laser diode is of the type ALC-1470-04500-CMT-125 from Akela Laser Cooperation, emitting at $\lambda_\mathrm{l} = 1477\,\mathrm{nm}$ width a spectral width of about 10 nm, see figure 5.2. The penetration depth in water for $\lambda_{\mathrm{l},r} = 1479.3\,\mathrm{nm}$ is $\xi_{\lambda_{\mathrm{l},r}} = (354.6 \pm 6.7)\,\mu\mathrm{m}$, this value is adapted for this laser in the following. With the used control electronics, see figure 5.3, the laser has a power of about $P = 3.2\,\mathrm{W}$. The duration and frequency of the pulses were $\tau_{\text{Laser on}} = 10\,\mathrm{ms}$ and 1 Hz, respectively. The maximal heating of the water was about 0.4 K.

The emitter of the laser is rectangular, with a length of 125 μm, thereby having the needed shape of a line, and thus a complex optical system can be omitted. Using a spherical lens with a focal length $f = 10\,\mathrm{mm}$, (Rembeck [2018]) calculates the length of the heated line to $(2.029 \pm 0.013)\,\mathrm{cm}$, which agrees with the observed length.

The IR-Camera

The utilized infrared (IR) sensitive camera, is the IRCAM Velox 327K M. It takes images of size 512 x 640 pixels, with a maximum frequency of 100 Hz and integration time of 2.5 ms. It is sensitive in the wavelength range between 3.4 and 5.0 μm. Instead of outputting images with the recorded intensity, the camera calculates the respective temperature and hence provides an image where the grey values correspond to the

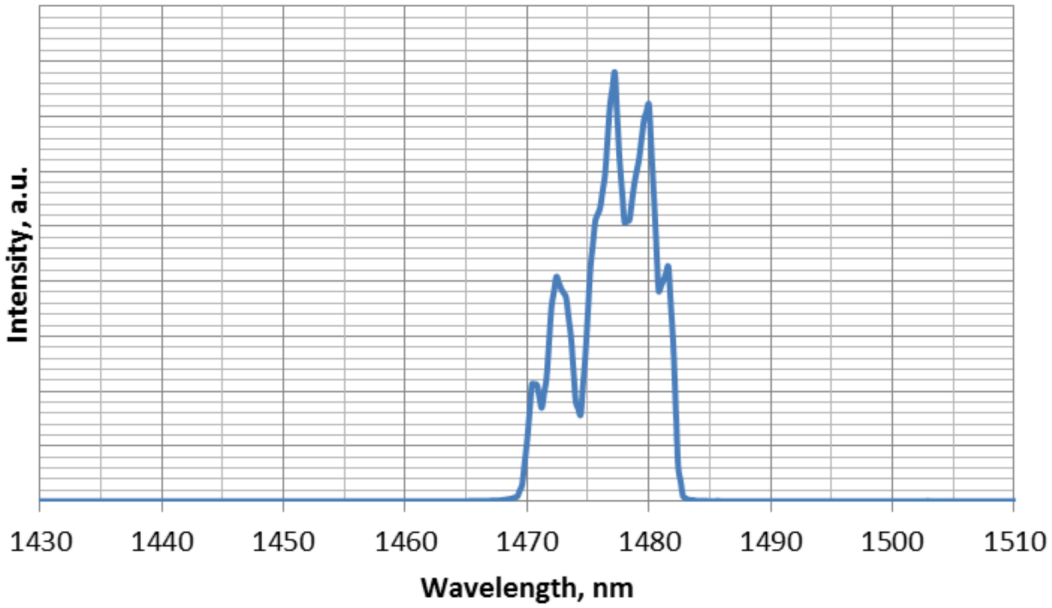

FIG 5.2.: Spectrum of the laser diode. The graphic is taken from its product sheet (las [2017]).

temperature of the objects.

The used objective has a focal length of 100 mm. Further on, as seen in figure 5.4 showing a sketch of the used setup, the camera is mounted at an angle θ_a of about 20° relative to the water surface normal, in the direction tangentially to the annual shape of the channel. The angle θ_y relative to the surface normal, in the radial direction, is small enough to be neglected. The advantage of mounting the camera at an angle, is to diminish the received reflections from the cooled camera sensor, at the cost of a more distorted view (Kunz [2017]).

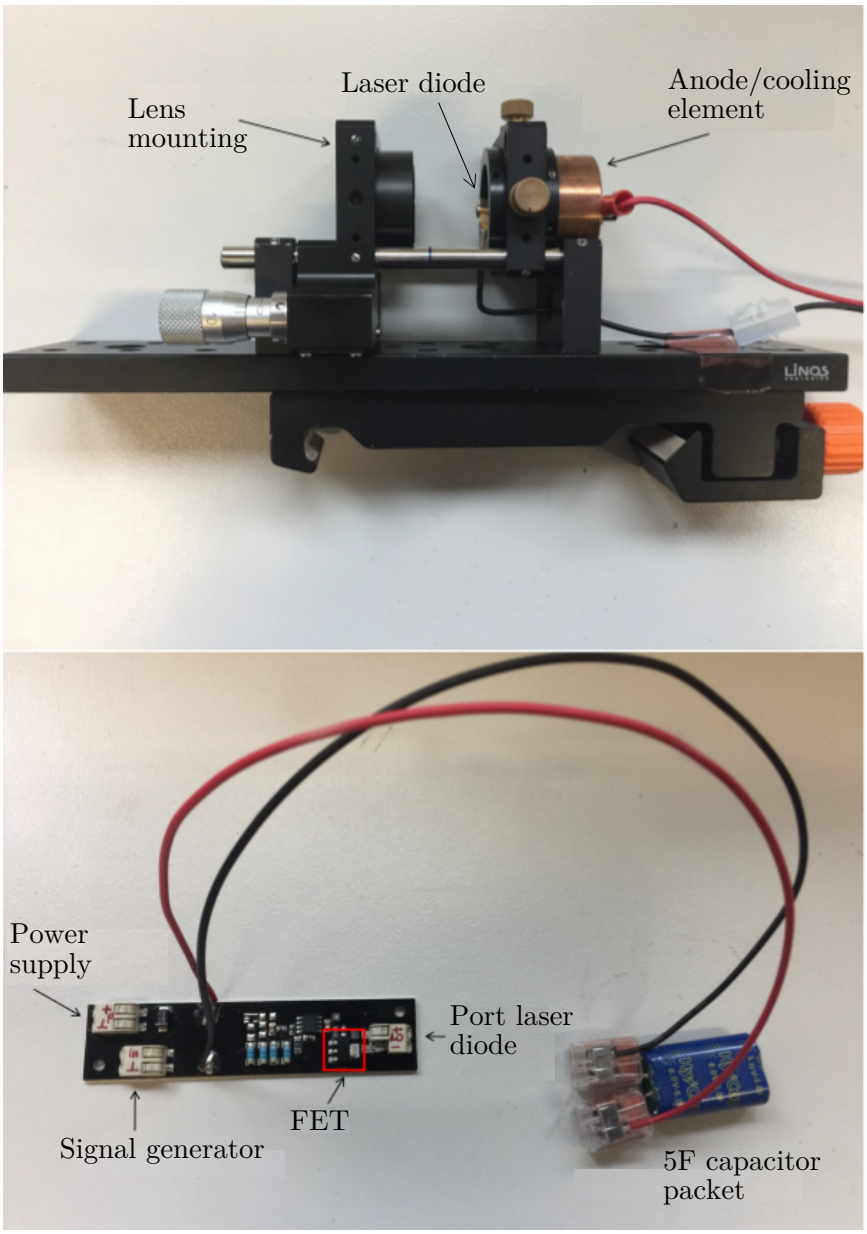

Fig 5.3.: The laser set up. Above: The laser system, note that the anode also serves as a cooling element. Below: The control electronics. The capacitor packet serves to reduce voltage spikes, and additionally enables a fast enough current supply to the laser diode. FET: field-effect transistor. Modified and adapted from Rembeck [2018].

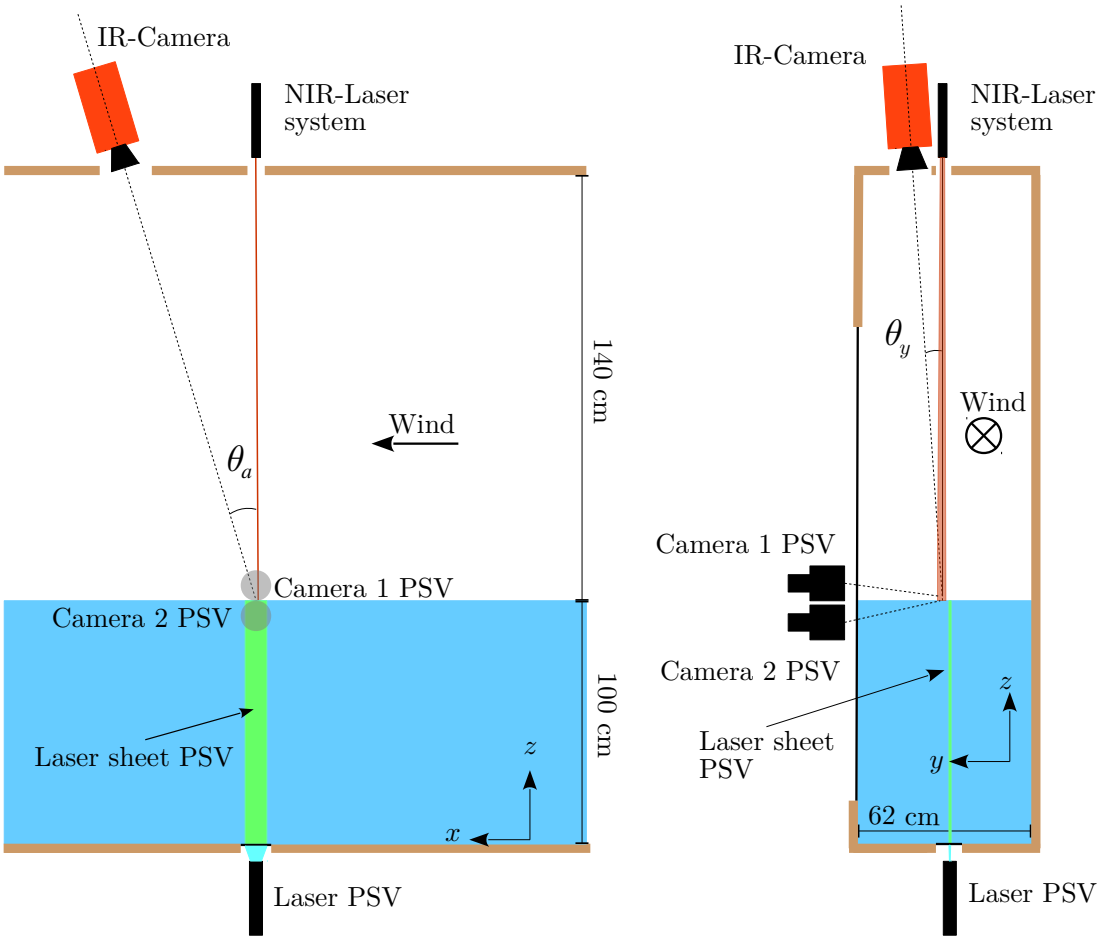

FIG 5.4.: Schematic overview of the setup, tangentially (left) and radially (right) to the wind-wave facility. Active thermography: The laser is pointing vertically at the surface, with the heated line parallel to the direction into the plane, that is, in the negative y direction. θ_a is about 20°, whereas $\theta_y \approx 0$ is negligible. The length of the heated line is about 2 cm. Particle streak velocimetry (PSV) setup: The laser sheet is oriented parallel to the channel walls. Camera 1 observes the water surface at a slight angle from above, and camera 2 the viscous boundary layer from below. Note that the two methods are measuring at about the same location.

5.2 Reference method: PSV

In order to be able to verify the measurements obtained by the thermographic approach, the particle streak velocimetry (PSV) method was applied for some measurements. This is a measurement technique described in detail in Bopp [2018]. Briefly summarized, it is based tracking particles, with a size of about 20 μm (Schwenk [2019]), by the use of a pulsed laser sheet. These pulses consist of five short, then a break, and additional two short pulses, giving enabling the identification of the direction and velocity of the particles, see figure 5.5. All these pulses can be seen in one image, meaning exposure time needs to be adjusted accordingly. The frequency of these groups of pulses were 50 Hz. The method was deployed in the viscous boundary layer, and in the upper transition region between the viscous layer and the bulk, using a camera looking upwards to the air-water interface at a slight angle, see figure 5.4. Another camera, looking at the interface from above at a slight angle and recording at 200 Hz, was also needed for the surface detection. For this purpose, the substance pyranine, a fluorescent dye, was used, as it is illuminating the water when excited by the laser. Hence, the interface becomes visible. The setup and evaluation of the measurements was conducted by Maximilian Bopp.

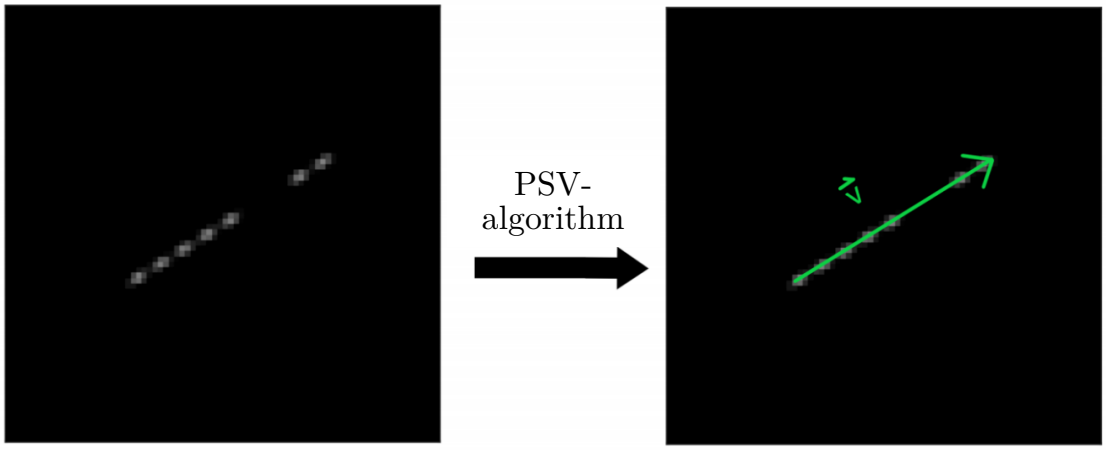

Fig 5.5.: The figure shows particle illuminated by one series of pulses. After running the PSV-algorithm described in Bopp [2018], the velocity and direction of the particle, and hence the localized flow, is known. The figure is modified and adapted from Schwenk [2019].

5.3 Measurements

The measurements were conducted between the 26.01.2019 and 04.02.2019. The water temperatures ranged between 19°C and 23°C, and did not vary within a measurement, with the exception of some low amplitude heat structures at the surface in some cases. These structures vanished on time scales of 10 s after turning the wind on.

There were three types of measurement conditions; stationary, periodic wind on-off, and non-stationary following the on-turning of the wind. The two first types were

conducted for wind speeds corresponding to wind generator frequencies of 5 Hz, 7.5 Hz, 10 Hz and 12.5 Hz, see table 5.1 for reference wind speeds.

For the stationary condition, a duration between 90 minutes for the lowest wind setting and up to 120 minutes for the highest, with the wind switched on, was awaited before the measurements. This assured that the system had reached equilibrium before the onset of the measurements. One measurement lasted about 600 s (hence corresponding to 600 heated lines) was conducted for each frequency, and the PSV method was also applied simultaneously.

The periodic on-off measurement was performed as follows: wind on at 15 Hz for 5 s for a faster build up of the wind field, then 55 s with wind at 10 Hz, before waiting 60 s with the wind turned off. This was then repeated periodically. After 130 minutes, when a stationary flow velocity of the bulk was achieved, the measurement lasting 1160 s was conducted.

The last type of measurement, the non-stationary conditions, at least five measurements with a duration of about 400 s from turning on the wind, were performed for each wind frequency. The water was allowed to settle for at least 35 minutes for the lowest frequency, and at least 40 minutes for the middle ones and 50 minutes for the highest, between each measurement. This was done to assure a proper reset of the conditions before conducting a new measurement.

6 Analysis

In order to extract the temperature profiles from the raw data, the images had to be processed. The obtained data then needed further processing, before being evaluated by the use of the simulation. How this was done, will be explained in the following chapter. The programming language Python was used for all parts of the analysis.

6.1 Image processing

In this section the process from the obtained raw images, with their grey scale values corresponding to the temperature, to the determination of the widths of the heated lines will be clarified. In the following, the heated lines will also be referred to as the signals.

Calibration

The images were calibrated using a checker board target with alternating copper and plastic squares of 22 x 22 mm, of which the copper squares could be heated for increased contrast. Using the same algorithm as in Bopp [2018], a mean image was first computed by averaging 10 images pixel by pixel. Then, the background of the mean image was calculated by using a Fourier transform, and only considering the low frequency components in the inverse transform. This background image was then subtracted from the mean image. The result of this subtraction could then be Fourier transformed, and reconstructed for low frequencies, yielding the amplitude image.

At last the background image was subtracted from a median filtered image, and divided by the amplitude image to compensate for remaining unwanted background structures. This modified image was then used as input to a build-in detect checker board function. The detected points were fitted as described in Bopp [2018], yielding the calibration. See figure 6.1 for the different images.

Note that the calibration was first applied after having analysed the raw data, in order to save computational effort.

Preprocessing of the raw images

As the raw images had many pixel errors, these had to be corrected in order to not distort the analysis and ultimately the results. However, as correcting the faulty pixels is unnecessary for the parts of the image not containing the heated line, the line was first detected and only the relevant parts of the image kept for correction and analysis.

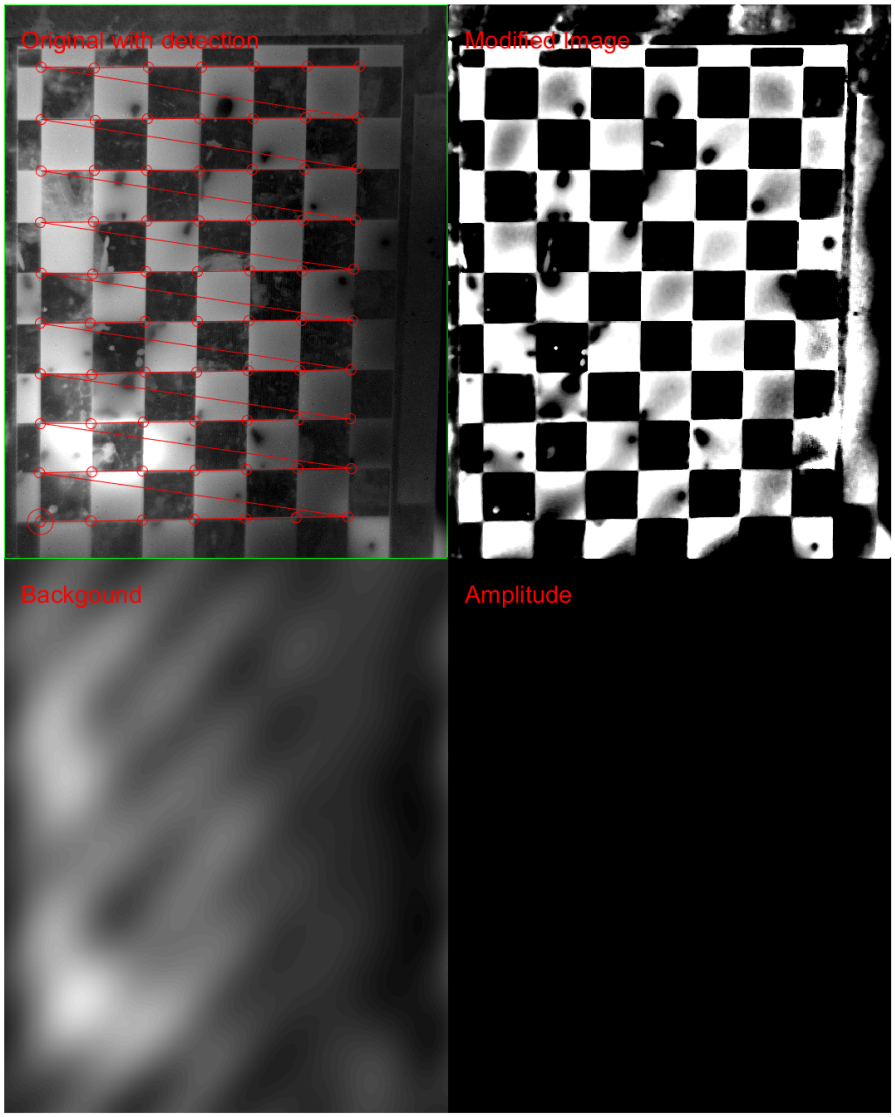

FIG 6.1.: The calibration. In the upper left part, the original image is shown together with its detected points. In the lower left corner the background image is shown, and in the lower right part the amplitude image. The latter is the result of a low pass filtering of a mean image subtracted the background. The modified image shows the result of a median filtered image with subtracted background, then divided by the amplitude image. This image was used as input for detecting the checker board. See section 6.1 and Bopp [2018] for further details. The figure was created by Maximilian Bopp.

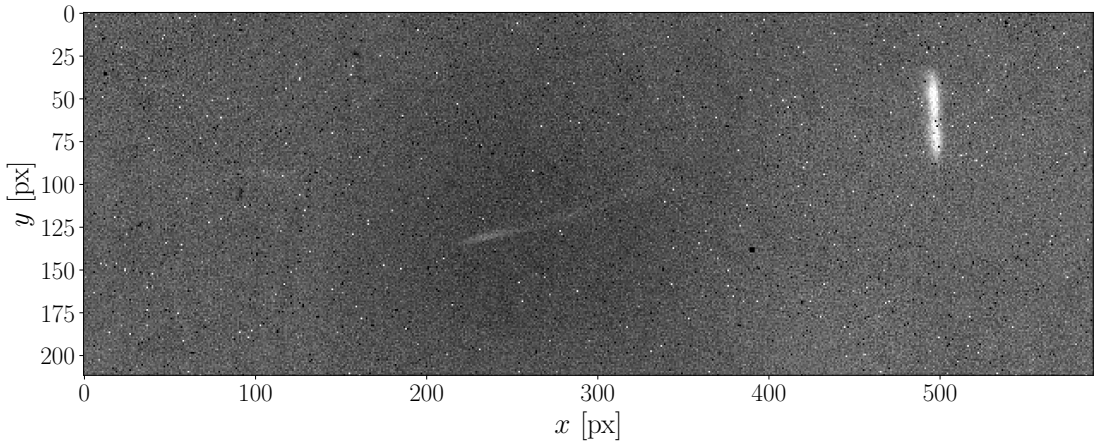

FIG 6.2.: A cropped raw image. Notice the dead pixels (black) and the hot pixels (isolated white pixels). The heated line is seen to the right, and is about 2 cm long. The previous line can also be seen in the middle of the image, being almost parallel to the x-axis. The wind direction is in negative x- and the inner wall of the wind-wave channel in positive y-direction.

Detection of the erroneous pixels

The first thing done for a measurement (typically corresponding to $\sim$ 50 000 images), was to find the faulty pixels. This was only done once for each measurement, hence resulting in a matrix containing the positions of these pixels. There were three different kinds of erroneous pixels; dead pixels, mostly having the lowest possible value of zero, the hot pixels having far too high values, and the unstable pixels with a large variance.

For detecting these pixels, a pixel-averaged image of the last 40 images, which did not contain any heated lines, was computed, yielding the mean image. The median image was then computed by applying a 5 x 5 median filter to the mean image, assuring a majority of non-defect pixel and hence a meaningful median. These two images were then subtracted, leaving a clear signature from strongly deviating pixels. From the latter image, the mean standard deviation and mean value of all pixels together were computed, hereby not considering the strongly deviating pixels, and hence forming a reference standard.

The deviating pixels were found by looping through the 40 mentioned raw images, from which the median image was subtracted in order to account for the background. It was then counted how often the individual pixel values deviated by more than five reference standard deviation from the reference mean value (close to zero). The pixel was considered faulty if this happened for more than 50% of the images.

Detection of the heated lines

The first step in the detection of the line, was dividing the respective image by the mean image explained above, hence removing gradients in grey values due to the background. A 12 x 1 box filter (i.e. calculating the mean over 12 pixels) was then convolved with every second row, that is, perpendicular to the heated lines. The box filter was applied in order to get rid of noise, hence leaving the respective rows smoothed. Now peaks in these rows could be detected, fulfilling certain criteria in amplitude and width in order to not detect signatures from the not jet corrected, defect pixels. These criteria were

found by trial-and-error. The coordinates of the peaks were then saved.

In order to detect the signals, the list of peak coordinates was searched for line-like clusters, indicating a found signal, as randomly detected peaks would tend to be spread arbitrarily. Utilizing that the wind always blows in the same direction, and no waves distort the movement of the heated lines, the relevant (newest) signal would always be the one furthest upwind in the images. Only the newest signals were considered for further processing. If the found clusters did not meet the chosen criteria, e.g. caused by to few peaks found within a given extent, the image would be discarded, instead of a "best guess" approach using the most line-like cluster found.

If a large enough jump in the signal position between to images was detected, and the new signal also lied within the known initial location of the heated line, this was counted as a new signal.

Correction of the faulty pixels

With the known signal positions, it was possible to only process a part of the image. The first thing that needed to be done, was to correct the defect pixels. Knowing their positions, this was easily done by taking the mean of their two neighbouring pixels in y-direction (parallel to the heated lines). The reason why the neighbours in x-direction were not considered, was to avoid smearing the width of the line, which ultimately is the searched quantity of the measurement.

Signal analysis

Finally, the signal was evaluated by fitting a Gaussian,

$$G(x;\mu,\sigma,A,c) = A\exp\left(\frac{-(x-\mu)^2}{2\sigma^2}\right) + c, \tag{6.1}$$

over heated lines in the x-direction, leaving the parameters free to be fitted. σ hereby describes the width of the line, and μ the location of the peak. In order to obtain more data points for the fit, row $i-1$ and $i+1$ was also considered in the fit of row i. The advantage of more stable fits overweighted the resulting smearing in y-direction. In order to avoid boundary effects due to the finite length of the heated line and the subsequent heat transport in y-direction, the five values at each end of the line were discarded.

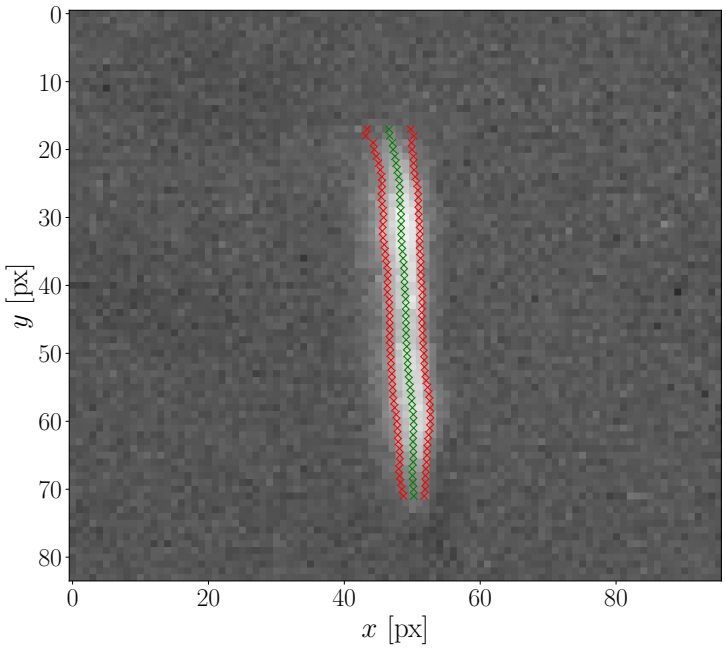

FIG 6.3.: The figure shows the part of the raw image (figure 6.2) with the found signal after processing. The wind blows in negative x-direction. Notice that the faulty pixels being corrected, leaving the signal and normal noise intact. The line width was determined by fitting a Gaussian in x direction, considering three and three rows for an increased number of data points. The green crosses indicates the values of μ, and the red crosses are located at $\mu \pm \sigma$.

6.2 Data analysis

Having processed the raw data, the heated lines were ready for calibration and further analysis. Since the velocity gradient of the flow in y-direction, $\partial u/\partial y$, is of interest and matters for the measured width of the lines (equation (3.7)), the presence and magnitude of such a gradient needed to be estimated.

The first step was to calculate the angle of the line at the points where the widths were measured. This was done by using cubic spline interpolation of the positions along the line (green crosses in figure 6.3), rendering an expression for $x(y)$. The angle θ_s relative to the y-axis was then calculated from the derivative of this expression, namely:

$$\theta_s = \arctan\left(x'(y)\right). \tag{6.2}$$

This is no problem, as a cubic spline is differential everywhere except at its endpoints. See figure 6.4 for an example of a line followed for the first 520 ms after heating, with the determined angles shown.

Having calculated the angles, these can be used for estimating $\partial u/\partial y$. Assuming the gradient at a fixed position along the line to be constant with respect to time within the duration of a signal ($\sim 1\,\mathrm{s}$), this leads to the following expression for $\theta_s(t)$:

$$\theta_s(t) = \arctan\left(\frac{\partial u}{\partial y}\cdot(t-t_0) + \tan(\theta_{0s})\right). \tag{6.3}$$

Here t_0 corresponds to the time of heating the line, and θ_{0s} to the initial line angle. With this expression, it is possible to sort the different parts of the lines per $\partial u/\partial y$, that is, consider all data points satisfying equation (6.3) for $\frac{\partial u}{\partial y} \pm \Delta\frac{\partial u}{\partial y}$. See figure 6.5 and 6.6 for examples of this sorting for the temporal evolution of an individual heated line, and figure 6.7 for a sorted data set compared to an unsorted.

When considering stationary conditions, the temporal development of the heated lines at different measurement times can be compared. The resulting distribution of the quadratic line widths $\sigma^2(t')$ of the lines at a given signal time t' since heating the line, is normal when the sorted data set is considered, see figure 6.7. Thereby Gaussians could be fitted, using the mean value $\mu(t')$ as a representative quadratic width of the heated line at t'. These can then be compare to the widths gained by the corresponding simulation. This will in the following be referred to as the statistical approach to evaluate the measurement.

In the case of a higher temporal resolution, only one or a few heated lines are considered at once, there are not enough data points to assure a Gaussian distribution. Therefore, the values of $\mu(t')$ used as a representation for $\sigma^2(t')$ as described above, were replaced by a fit of a third degree polynomial $p_3(t)$ through $\sigma^2(t)$ for all data points lying within the to be considered time interval (section 6.4), with $p_3(t)$ describing the shape well (see section 7.1.2).

The initial width of the heated line, σ_0, on the other hand, was more difficult to estimate. As shown in figure 6.8, the initial widths, except for the first while the laser is still heating, are somewhat larger than the ones that follow immediately after, i.e. the lines are getting thinner. This is unphysically in the context of the described system and might be due to a reflex from the laser heating the surroundings of the line. After about 50 ms, the widths reach a minimum, and start to broaden again. As the velocity

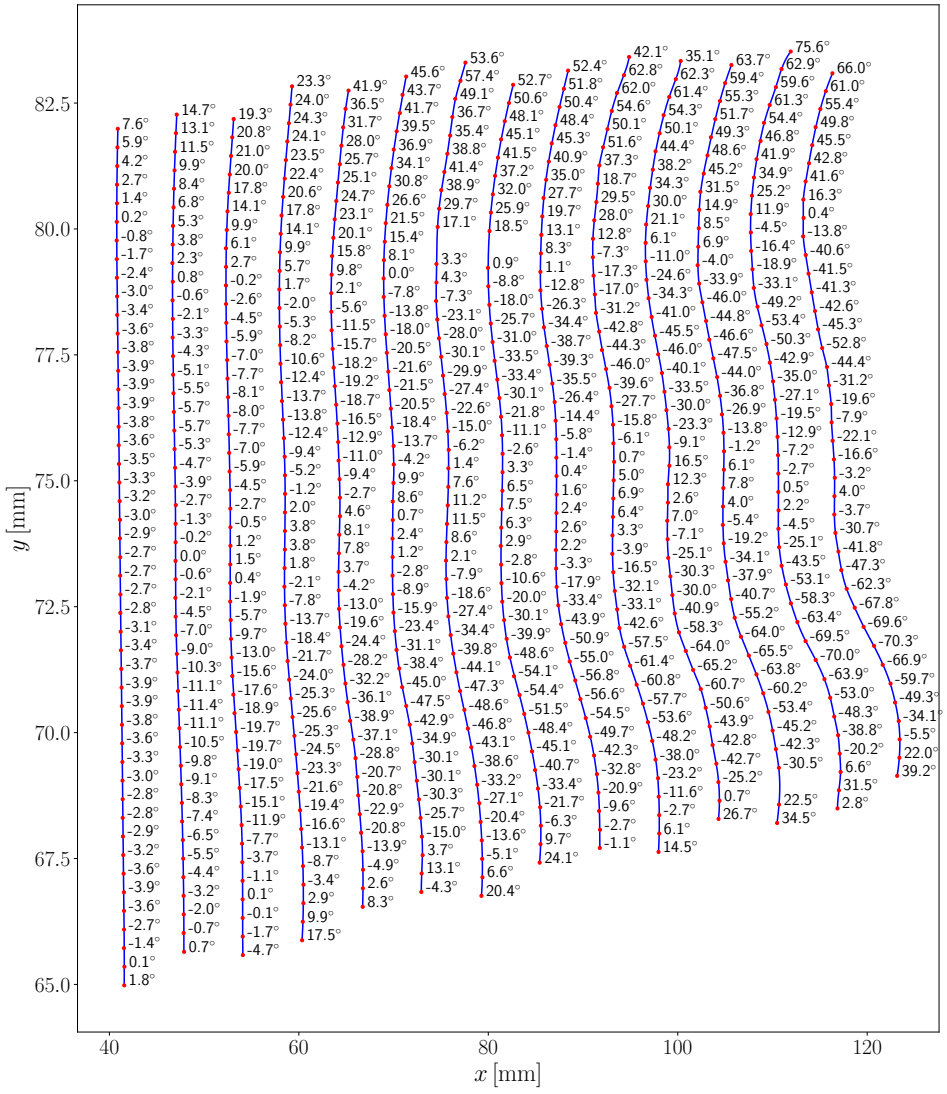

FIG 6.4.: The figure shows the heated line every 40 ms for the first 520 ms after heating. The wind direction is from left to right, and the positive y-direction points towards the inner wall of the facility. The calculated angles θ_s relative to the y-axis are given in degrees, and located at the right side of the point at which they describe the angle. Note that the mean initial angle is not perfectly 0°, and that the line is shortening somewhat with time, because of heat loss at its ends. Points that are missing out correspond to failed fits.

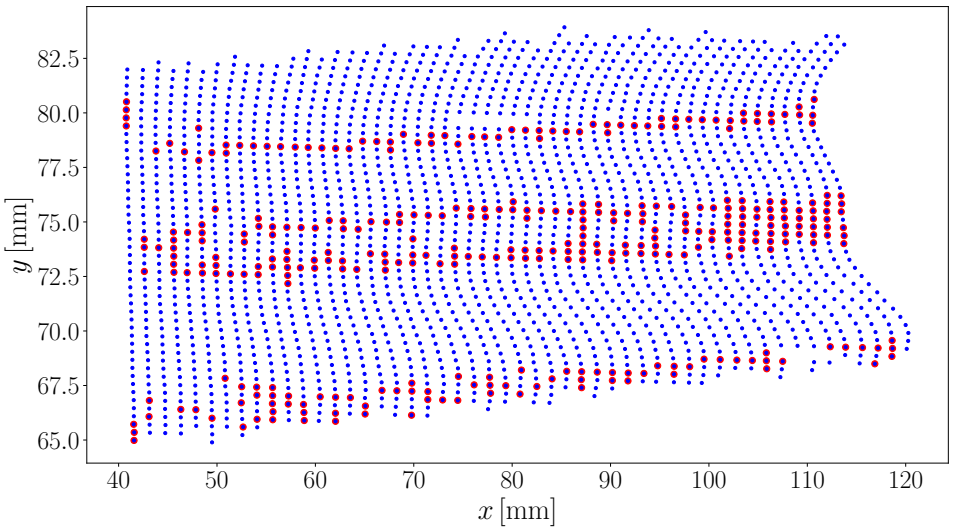

FIG 6.5.: The figure shows the heated line under stationary conditions at the 10 Hz wind setting, for every 10 ms (corresponding to the frequency of the camera) for the first 500 ms after heating. The wind direction is from left to right, and the inner wall is located in positive y-direction. The red dots show the part of the line that corresponds to $\left|\frac{\partial u}{\partial y}\right| \pm \Delta\frac{\partial u}{\partial y} = (0.0 \pm 0.2)/\text{s}$ (see equation (6.3)). The initial angle was θ_{0s} = -2.1°. As the figure shows, the structure of the surface flow can be followed reasonably well. Notice the different scales of the two axes. The line is the same as the one in figure 6.4.

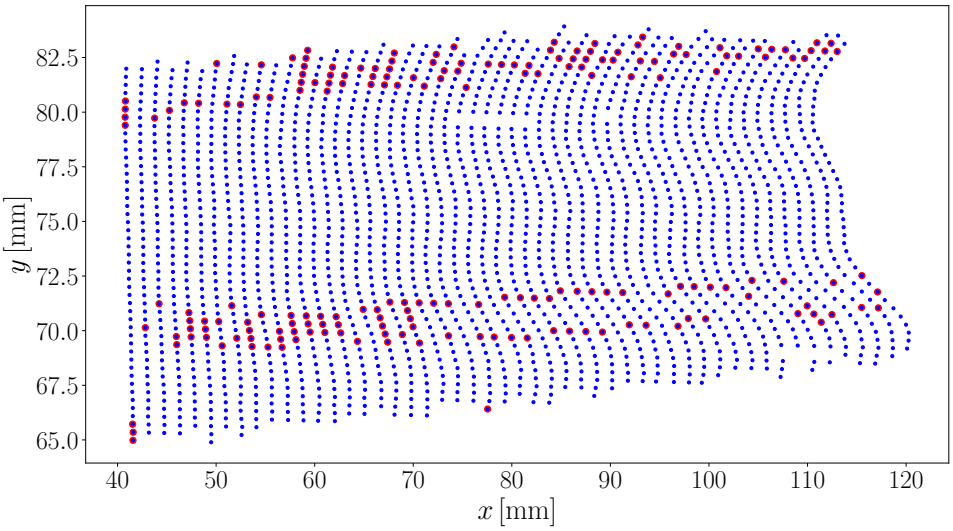

FIG 6.6.: Analogous to figure 6.5, but for $\left|\frac{\partial u}{\partial y}\right| \pm \Delta\frac{\partial u}{\partial y} = (3.9 \pm 0.3)/\text{s}$. Again, the structures can be followed reasonable well, indicating that equation (6.3) yields a valid description.

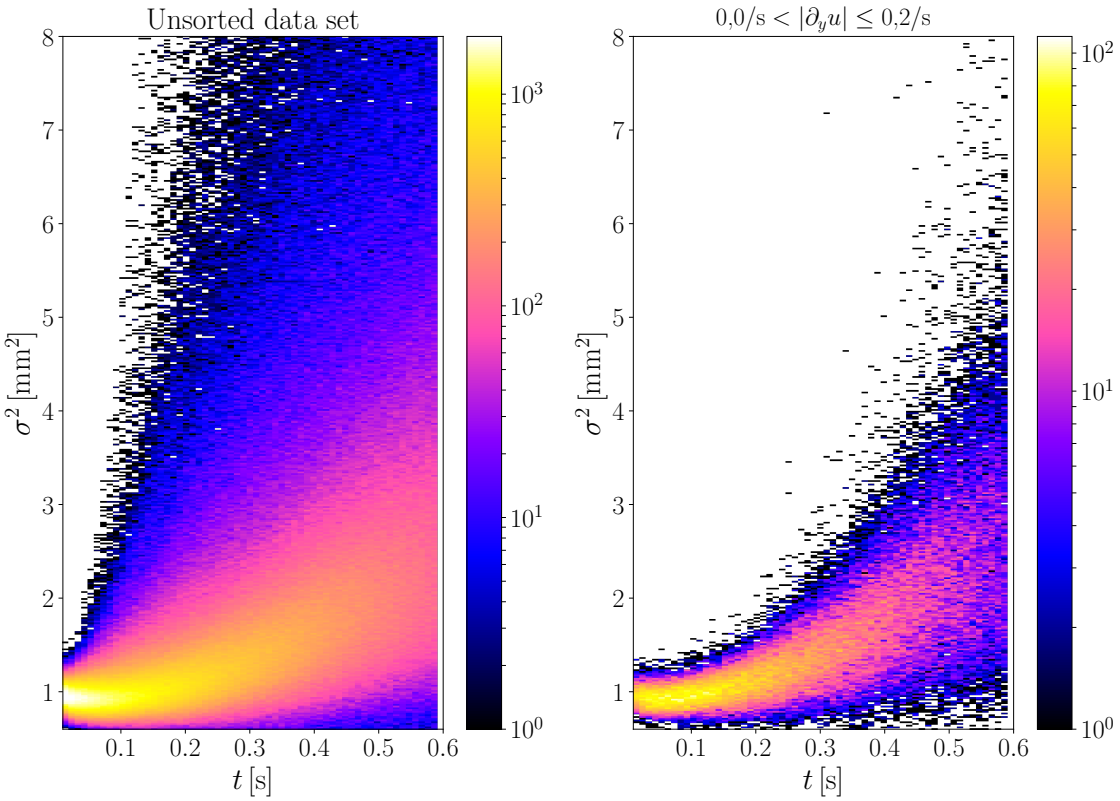

FIG 6.7.: The figure shows the unsorted (left) and sorted (right) data set for the 10 Hz stationary measurement. The ordinate shows the quadratic widths of the headed lines, and the abscissa the time since the heating of the line. The plot of the sorted set shows only the data points meeting the angle criteria of equation (6.3), for $\left|\frac{\partial u}{\partial y}\right| \pm \Delta\frac{\partial u}{\partial y} = (0.0 \pm 0.2)/\mathrm{s}$. The colours represent the number of data points, note the logarithmic scale. The distribution of the data points at a given time, tend to resemble a skew Gaussian in the unsorted case, and the normal distribution when sorted.

gradient need time to distort the initial profile and cause the excess broadening of the line, the initial broadening can be assumed to be according to 1D diffusion, i.e.

$$\sigma^2 - \sigma_0^2 = 2\alpha t, \tag{6.4}$$

with α being the thermal diffusivity. The initial width were therefore estimated by fitting a third degree polynomial through the widths of the first 100 ms after turning on the laser, and then use the minimum of this curve and extrapolate it to t = 0. This was found to be the most stable way to estimate σ_0. For comparison, σ_0 was also estimated as the mean value of the five first values of μ (t <50 ms), which could the be used to evaluate the measurements and thereby obtain an uncertainty in the calculated τ_{visc} regarding σ_0.

In the case of considering only a few lines, the explained estimation could not be used in the lack of a sufficient number of data points. Hence, σ_0 was estimated as the mean value of the widths for times in the interval 20-50 ms since heating the line, using the standard deviation as an indicator for the uncertainty of this approach.

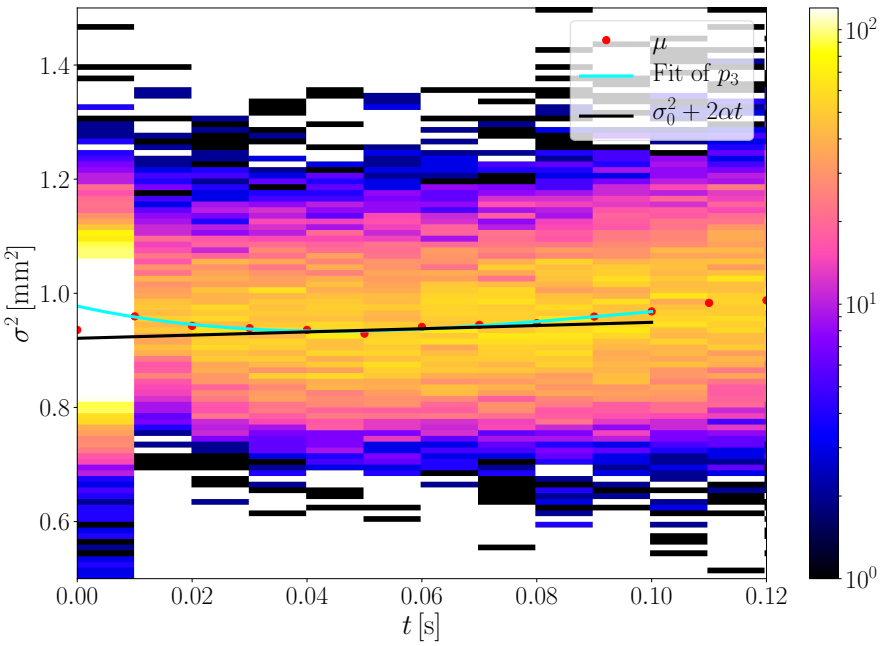

FIG 6.8.: The estimation of the initial width of the line σ_0, for a data set for $\left|\frac{\partial u}{\partial y}\right| \pm \Delta\frac{\partial u}{\partial y} = (0.0 \pm 0.2)/\text{s}$. Note that some bins for the first 10 ms are white due to saturation of the plot, as no $\partial u/\partial y$ sorting is done while as the laser is still heating the line. As the minimal width is not at $t = 0$, but reached somewhat later, a third degree polynomial p_3 is fitted to the values of μ obtained by fitting a Gaussian over distributions of $\sigma^2(t)$. The minimal value of the polynomial is then extrapolated to $t = 0$ for the determination of σ_0.

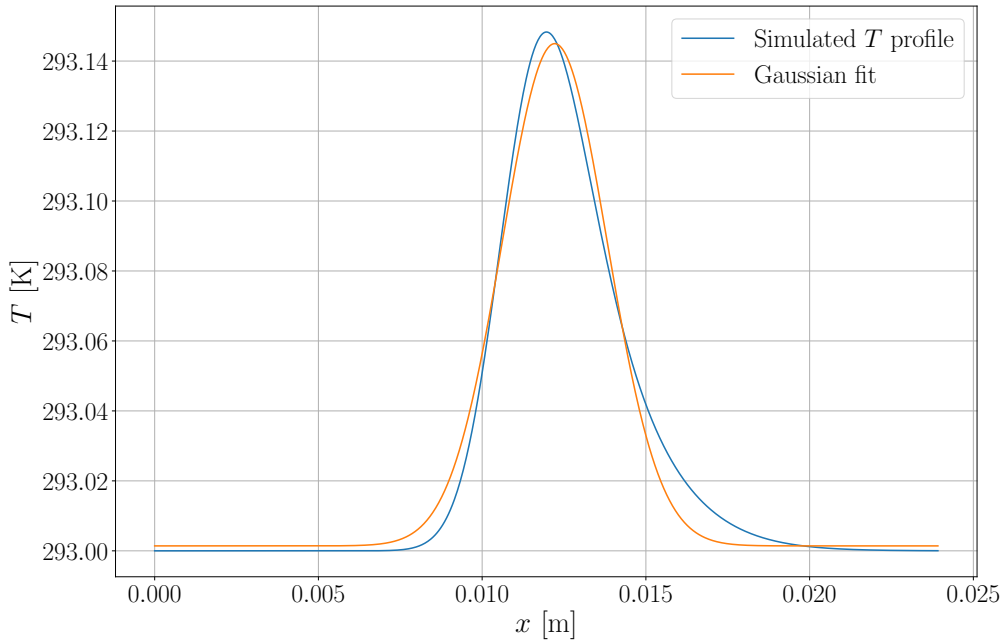

Fig 6.9.: A simulated temperature profile (blue) 0.5 s after heating. There was no shear in y-direction, and the velocity gradient in z-direction $\partial u/\partial z = 35/\text{s}$. The shape is slightly unsymmetrical, more like a skew Gaussian, in contrast to the Gaussian (orange) actually fitted to the profile. However, the fit is still able to estimate the width.

6.3 Analysis of the simulation

As explained in section 4.6, the output of the simulation consists of three different temperature profiles; one carefully analysed based on equation (4.38) and two simplified approximations. Irrespective of this, all temperature profiles were analysed by fitting Gaussians to them. The profiles are, however, not truly Gaussian shaped due to boundary effects at the surface, and resemble skew Gaussians, especially for longer times since the heating of the line, see section 7.1. The fits therefore miss the exact position of the maximum, but this value is of minor interest. More importantly, the performed fits still yield a good approximation of the widths, and considering that the real data was evaluated in the same manner, the fitting of Gaussians is the method of choice. See figure 6.9 for a plot of the temperature profile and the fitted Gaussian.

6.4 Matching the measurements with the simulation

In order to be able to analyse the measurements, the line widths needed to be compared to the results of the simulation. As the simulations were only carried out for certain combinations of parameters, which generally not coincided with the actual physical ones, the simulated data was interpolated. This means that the unknown quantity, i.e. $\tau \propto$

$\partial u/\partial z$, was interpolated linearly as a function of $t, \partial u/\partial y, \sigma_0^2$ and $\sigma^2(t)$. In the case of $\partial u/\partial y = 0$, this parameter was omitted, as the range of permitted gradients in y-direction $\Delta(\partial u/\partial y)$ is small. The choice of linear interpolation is not optimal, but the built-in function did not support cubic interpolation for more than two dimensions. As $\sigma^2(t)$ was only calculated for every 50 ms in the simulation, a linear approximation is suboptimal to describe the clearly non-linear temporal development of this parameter. However, a third degree polynomial turned out to describe the simulated widths well (see section 7.1.2), and hereby the temporal resolution of the simulated data could be increased, reducing the unwanted effects due to the linear interpolation. These fits for upsampling the simulated data were applied only to the time interval also used to evaluate the measured data, see below.

The effect of additional broadening of the lines due to the velocity gradients needs some time to develop, as it is a result of the tilt in the vertical profiles. This means that the distinction of the line widths for the different velocity gradients increases with time. Furthermore, the measured data becomes affected by a bias if the signals are evaluated at high times, as the lines exposed to fluctuations of high shear stresses weakens more and become harder to differentiate from the noise. This leads to more data points corresponding to low shear for high signal times. Hence, it is desirable to evaluate the data at high times, but before being affected by this bias. The upper time limit t_r could be roughly estimated by considering the curvature of the temporal development of the quadratic line widths $\partial^2\sigma^2/\partial t^2$, as there should be no roots of this curvature according to the simulations. In the case of the measurements, however, the mentioned bias causes a root at t_r, this being assumed as the highest time unaffected by the bias. The lime-green, vertical line at $t = 0.43\,\mathrm{s}$ in figure 6.10 corresponds to t_r. In most cases, the estimation of t_r was difficult due to scattering of the data points, sometimes leading to multiple roots or roots that depend on the interval of evaluation, and was used as a guideline rather than an absolute criteria.

In the case of using the statistical approach (see section 6.2) to evaluate the measurements, the values for $\mu(t)$ of the Gaussian fits of the line width distributions $\sigma^2(t)$ were fitted with $p_3(t)$ in order to reduce outliers. This was done for a somewhat broader time window than used for the evaluation, a look at figure 6.10 is illustrative. In the case of considering only a few lines, the values of the fitted $\mu(t)$ were, as explained in section 6.2, replaced by a fit of $p_3(t)$ through the quadratic widths directly. In both cases, the array of values $p_3(t')$, $t' \in [t_1, t_2]$ obtained from the fits were used for representing $\sigma^2(t')$ in the time interval $[t_1, t_2]$ between the grey vertical lines in figure 6.10. The array $p_3(t')$ was then put into the interpolated simulated data set, along with the other two necessary parameters ($\partial u/\partial y$ and σ_0), returning the values for viscous shear stress τ_{visc}. For each element of $p_3(t')$ one value for τ_{visc} was returned. The returned values corresponding to the chosen time interval of evaluation (lime lines in figure 6.10), were then averaged. For an uncertainty estimation, the returned values of τ_{visc} for $t' \in [t_1, t_2]$ were used to compute the standard deviation, this interval accounting for the uncertainty of the upper time limit t_r. The time window $[t_1, t_2]$ was chosen according to the measurement, and tended to be narrower for high wind speeds as the broadening of the heated lines is stronger and hence develops on shorter time scales.

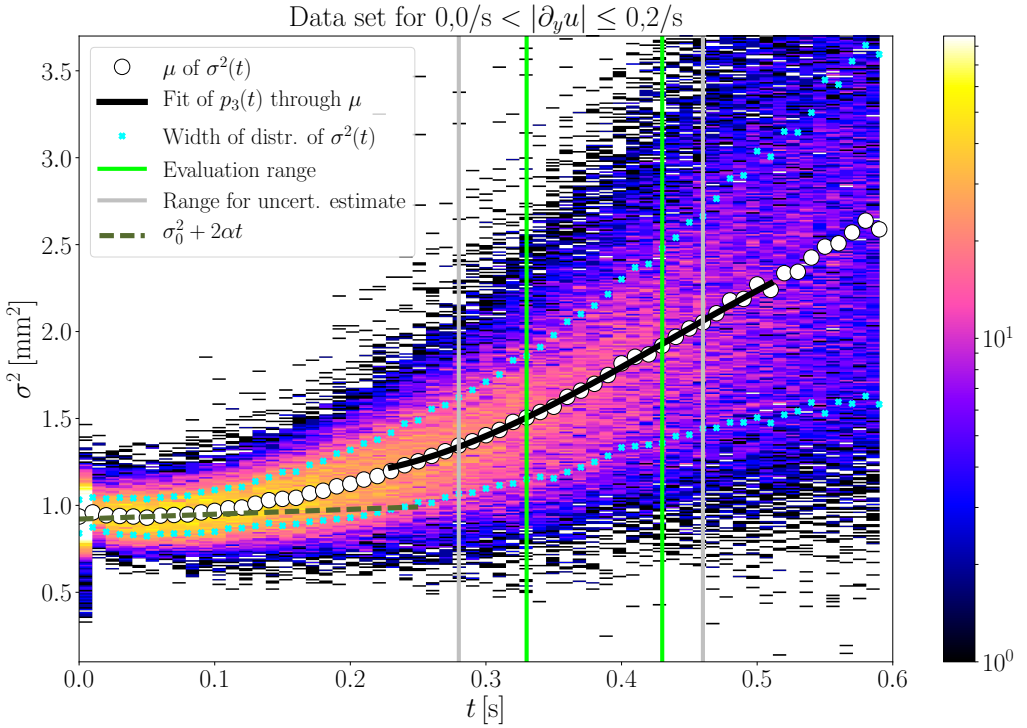

FIG 6.10.: The figure illustrates the principle of the data evaluation, here for the statical approach, showing the stationary 10 Hz data set for $\left|\frac{\partial u}{\partial y}\right| \pm \Delta\frac{\partial u}{\partial y} = (0.0 \pm 0.2)/\mathrm{s}$. The white dots show the mean values μ from the Gaussian fits of the distributions $\sigma^2(t)$, whereas the cyan crosses show the standard deviations of these Gaussians. The black solid line shows the fit of $p_3(t)$ through μ, used to represent these values. The time interval used for the evaluation of $\tau_{\mathrm{visc}} \propto \partial u/\partial z$ is shown as lime-green vertical lines, and the interval for the uncertainty estimate with the grey lines. Note that the slope of $\sigma^2(t)$ is decreasing for higher times outside the evaluation range. The olive green dashed line shows the estimate for σ_0^2, which is corresponding to the line at $t = 0$. Thereby all needed parameters are known ($\sigma^2(t), \partial u/\partial y$ and σ_0^2), and the data can be evaluated by directly passing these values to the interpolated data set from the simulation, returning the values for τ_{visc}. The result is shown in figure 7.8 in section 7.2.

6.5 Constants and parameters

Constant or parameter	Symbol	Value
Grid cell length in z-direction[1]	Δz	$15\,\mu$m
Grid cell length in y-direction	Δy	$15\,\mu$m
Grid cell length in x-direction	Δx	$30\,\mu$m
Domain length in z-direction	l_z	2 mm
Domain length in y-direction (3D case)	l_y	$45\,\mu$m
Domain length in x-direction	l_x	30 - 120 mm
Time step	Δt	0.4 ms
Heating time	$t_{\text{laser on}}$	10 ms
Time step between evaluating the temperature profile		50 ms
Simulated total time of the signal	$t_{\max}$	0.5 - 1 s
Velocity gradient in z-direction	$\partial u/\partial z$	0 - 65/s
Step size of velocity gradient in z-direction		1/s
Velocity gradient in y-direction	$\partial u/\partial y$	0 - 6.0/s
Step size of velocity gradient in y-direction		0.5/s
Dynamic viscosity	μ	$1001.6\,\mu$Pa·s
Initial width of heated line	σ_0	0.6 - 1.4 mm
Thermal diffusivity	α	$1.4{\cdot}10^{-7}\,\text{m}^2/\text{s}$
NIR-Laser wavelength	$\lambda_\text{l} \pm \Delta\lambda_\text{l}$	(1477 ± 5) nm
Penetration depth laser	ξ_{λ_l}	$355\,\mu$m
IR camera sensitive range		3.4 - 5.0 μm
Penetration depth in camera sensitive range	$\xi(\lambda)$	see figure 4.4
Mean penetration depth in camera sensitive range	$\bar{\xi}$	$44\,\mu$m
Initial temperature	T_0	293 K
Power of laser per unit line length	P_l	175 W/m
Density of water at 20°C	ρ	$998.2\,\text{kg/m}^3$
Specific heat capacity of water	c_V	4182 J/(K·kg)
Angle of observation, air	θ_a	20°
Angle of observation, water	θ_w	14.7°
Refractive index water	n_w	1.33

Table 6.1.: The constants and parameters used in the simulation and for the analysis.

[1] A grid cell size in z-direction of $\Delta z = 10\,\mu$m also was tested. That yielded a computation time that is about 3 times longer, as Δz and Δt is closely related over equation (4.19). The quadratic line widths $\sigma^2(t)$ for higher times t than considered in the analysis, differed by less than 1‰ from the case of $\Delta z = 15\,\mu$m, for all tested combinations of parameters. These combinations where evenly spread over the whole range of those considered in the simulations. Hence, the coarser resolution was chosen in order to save computational time.

7 Results and discussion

In this chapter, the results of the simulations as well as of the measurements will be shown and discussed. For all following sections except for the last, only data sets corresponding to velocity gradients in y-direction $\partial u/\partial y$ close to zero will be considered. See section 6.2 for more information. As the measured line widths depend on $\partial u/\partial y$, allowing a certain range of this parameter, is connected to introducing errors. These (relative) errors can be estimated by the simulation, and are, when allowing for $\partial u/\partial y$ of up to 0.2/s, in the range $\sim 1\%$.

Values that differ by more than 3 standard deviations, will be referred to as significant deviations. Wind speeds will still be given in terms of the wind generator frequency, for the actual reference wind speeds, see table 5.1.

7.1 Simulation results

Figures 7.1 and 7.2 show two cross sections of the simulated volume of the same run at different times. The typical behaviour can be illustrated with these figures.

The profile immediately after heating of the line (figure 7.1) is not tilted due to the shear yet, and of Gaussian shape. Hence, the to be expected broadening at these low times, corresponds to 1D diffusion (equation (6.4)). Later on, the tilt due to the shear develops, causing the additional broadening as explained in section 3.1. However, as figure 7.2 shows, boundary effects due to the surface develops, leading to a bend in the temperature profile width depth. These can be understood by imagining the volume of the water surrounding the heated line. Upwind of the line, close to the surface, the volume between the profile and surface is smaller than downwind. Therefore the heat flowing from the profile to the surrounding water, can be distributed to larger amounts of water downwind of the profile, hence leading to a greater heat loss in that direction. Upwind the situation is the opposite, with a smaller heat loss, leading to the in section 6.3 mentioned surface profiles resembling skew Gaussians. This also has the consequence, that the neglection of boundary effects in the earlier approach (see section 3.2) is leading to a clearly incorrect description.

7.1.1 Comparison with the earlier approach

The boundary effect can be quantitatively analysed by comparing the width $\sigma(t)$ of the temperature profile at the surface, with the one deeper down ($z = 1.3\,\mathrm{mm}$ in the following). A comparison with the analytical model, equation (3.5), is also of interest. This is because the model neglects boundary effects, and the deeper layers are less influenced by them. See figure 7.3 for the a plot of $\sigma^2(t)$ for the three cases. As can

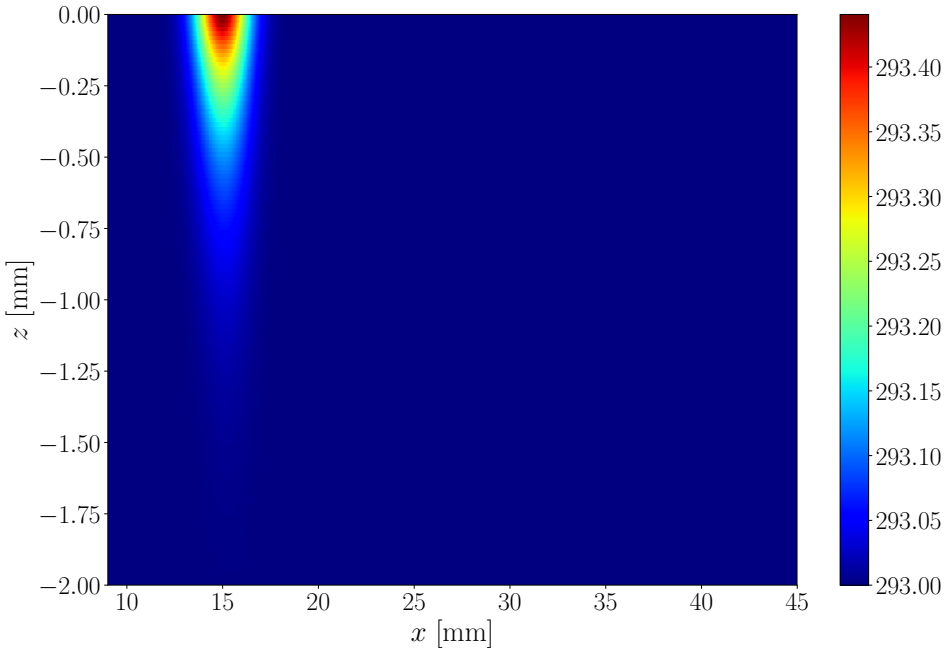

FIG 7.1.: Part of the simulated volume directly after heating the line, $t = 10\,\text{ms}$. $\partial u/\partial z = 30/\text{s}$, $\partial u/\partial y = 0/\text{s}$ and $\sigma_0 = 1\,\text{mm}$. z describes the depth, and the wind direction is in negative x-direction. The colour coding represents the temperature in Kelvin.

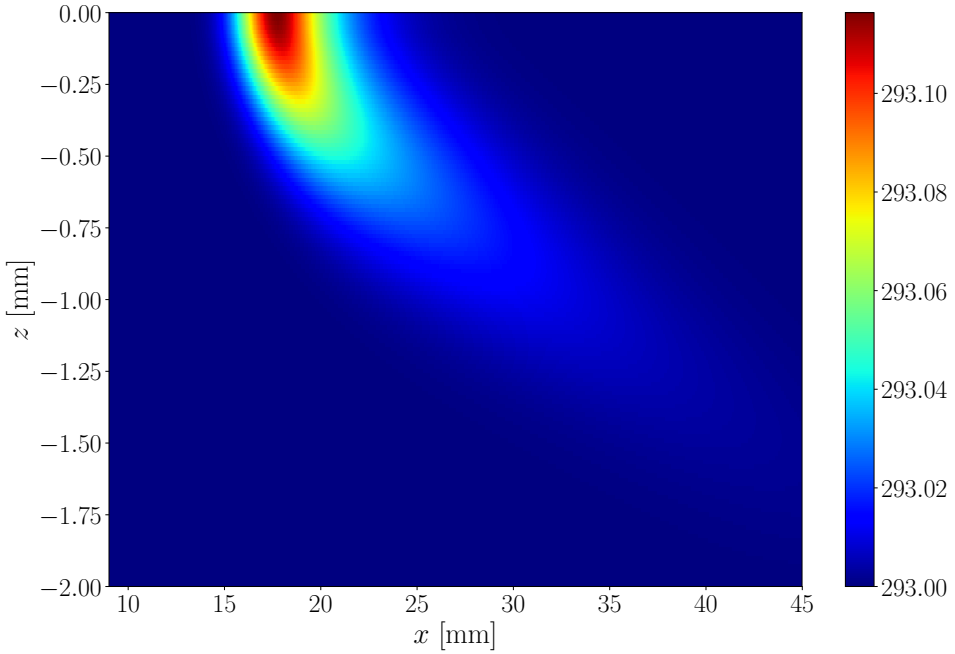

FIG 7.2.: The simulated heated line after 0.7 s. Analogous to figure 7.1. The shear is tilting the temperature profile, therefore the upwind (positive x-direction) amount of water "locked" between the surface and the temperature profile, is smaller than the downwind amount. This leads to a greater heating of the "locked" water upwind of the profile compared to downwind, and causing the bend in the profile towards the surface. Note the displacement of the temperature maximum at the surface due to the bending.

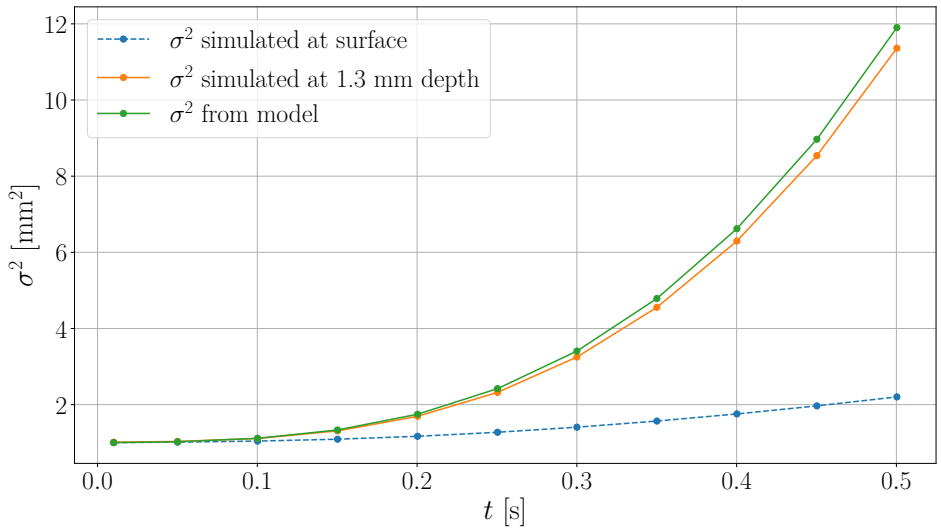

FIG 7.3.: The quadratic, simulated line widths σ^2 at the surface and at 1.3 mm depth, compared to the widths estimated by the analytical model (3.5). The parameters were $\partial u/\partial z = 30/\text{s}$, $\partial u/\partial y = 0/\text{s}$ and $\sigma_0 = 1\,\text{mm}$. As can be seen, the widths for the deeper layer and the model deviate strongly from the simulated surface layer. The deviations between the model and the layer at 1.3 mm, are likely caused by the model assuming the temperature profile as independent of z, which it is not.

be seen, the model and deeper layer compare as expected, with deviations likely caused by the model assumption of the temperature profile as independent of z. The widths of the line at the surface, on the other hand, deviate strongly compared to the model. Therefore, equation (3.5) will not be considered in the following for evaluating the viscous sheer $\tau_{\text{visc}} \propto \partial u/\partial z$.

7.1.2 Parametric dependencies of the line widths

The simulation gives the opportunity to study the behaviour of the system when varying the different parameters. In the following, only the profiles at the surface are considered, as these are of key interest. A variation of the power of the laser, that is, increasing or lowering the amplitudes of the temperature profiles (still neglecting heat induced advection), turned out to not play a role. The relative deviations of the *quadratic* line widths by varying the laser power by +100 % and -50 % were smaller than 0.1 ‰ for all tested combinations of the other parameters.

Shear in z-direction

When looking at the dependencies of the (quadratic) widths as a function of time, whilst varying the shear in z-direction and keeping the other parameters constant ($\sigma_0 = 1\,\text{mm}$, $\partial u/\partial y = 0$), figure 7.4 arises. Only some interesting values of $\partial u/\partial z$ are shown in the figure. Recall that the viscous shear stress $\tau_{\text{visc}} \propto \partial u/\partial z$ is constant within the simulated volume of the boundary layer.

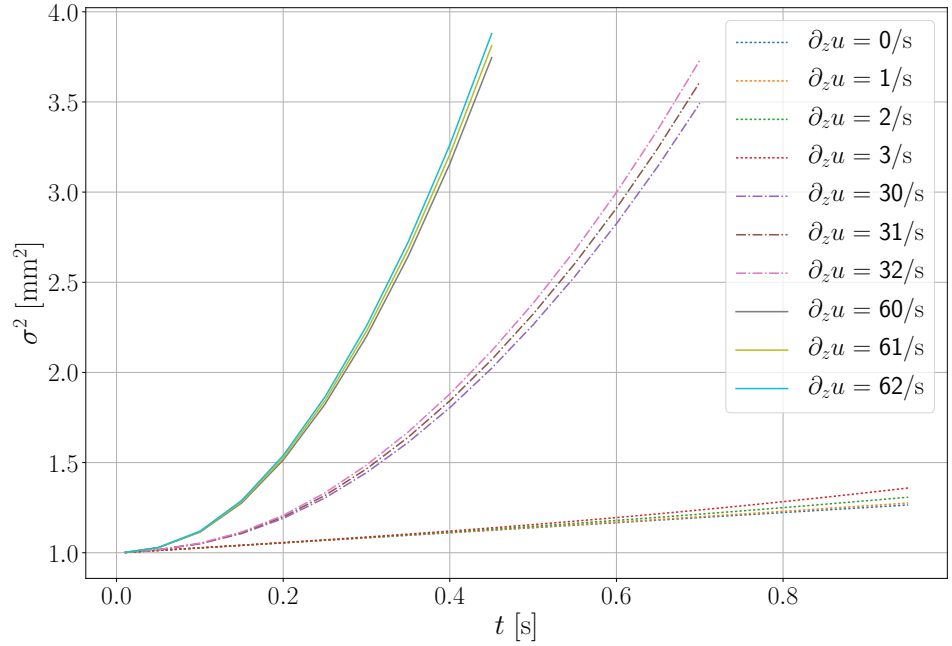

FIG 7.4.: The dependencies of the temporal change of the quadratic line widths σ^2 on a constant gradient with depth, $\partial u/\partial z$. The other parameters where kept constant; $\sigma_0 = 1$ mm, $\partial u/\partial y = 0$. As the figure shows, σ^2 for a given time is a monotonically increasing function of $\partial u/\partial z$, ultimately enabling the approach of this work. Further on, for $\partial u/\partial z = 0$, the change is linear, as expected for 1D diffusion, see equation (6.4).

As figure 7.4 shows, $\sigma^2(t)$ is a monotonically increasing function of $\partial u/\partial z$. This also holds for the values in-between the shown, ultimately enabling the determination of the viscous shear by the method presented in this thesis. For $\partial u/\partial z = 0$, the 1D diffusion equation (6.4) is obtained, as expected. This was confirmed by a linear fit yielding a relative deviation from the theoretical coefficient of less than 0.1 ‰.

Shear in y-direction

The quadratic line widths also depend on the velocity gradient in y-direction (parallel to the lines). This contribution is not only due to the geometrical contributions from the resulting angle of the line, considering that the widths are measured in x-direction; there is an additional broadening stemming from the same principle as for the influence of $\partial u/\partial z$. Indeed, when considering the analytical model (3.5) for $\partial u/\partial z$, the assumption was a temperature distribution independent of z, which turned out to be invalid. For the y direction, however, this assumption is fulfilled when substituting z with y, that is,

$$\sigma(t) = \sqrt{\sigma_0^2 + 2\alpha t \left(\frac{1}{3} \left(\frac{\partial u}{\partial y} \right)^2 t^2 + 1 \right)} \,. \tag{7.1}$$

This is enables the (analytical) description of σ^2 if the only shear stress is in y-direction, see figure 7.5.

As the figure shows, the contribution to the additional broadening of the lines is quite substantial, even for low values of $\partial u/\partial y$. Notice that the contributions to the quadratic

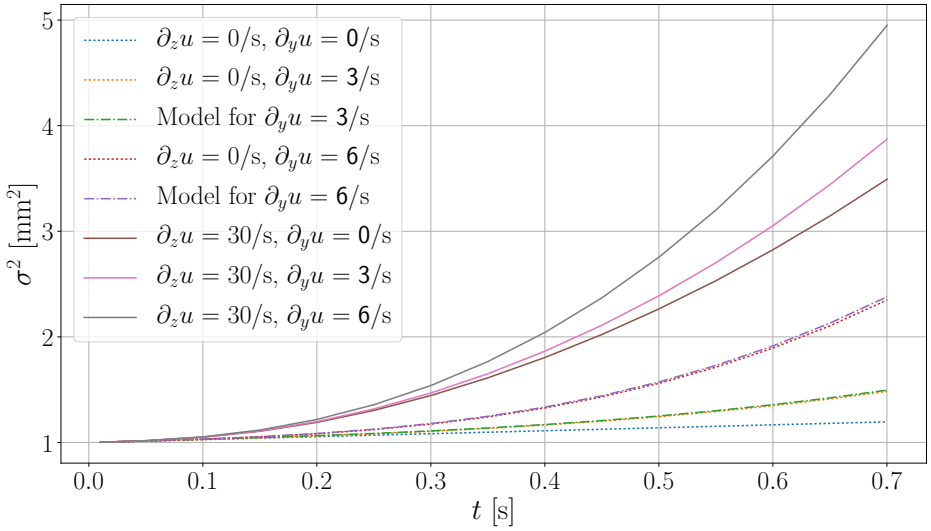

FIG 7.5.: The dependencies of the temporal change of the quadratic line widths σ^2 on a constant gradient parallel to the lines, $\partial u/\partial y$, for the two values of $\partial u/\partial z = 0$ (dotted lines) and 30/s (solid lines). The initial width σ_0 was kept constant at 1 mm. As the figure shows, σ^2 at a given time is monotonically increasing with $\partial u/\partial y$, and the influence is large relative to that of $\partial u/\partial z$. The two contributions do not add up. For $\partial u/\partial z = 0$, the analytical model (3.5) (dash-dotted lines) yields a satisfactory description when evaluated for $\partial u/\partial y$ instead of $\partial u/\partial z$.

line width from $\partial u/\partial z$ and $\partial u/\partial y$ do not add up. Also for $\partial u/\partial y$, $\sigma^2(t)$ is monotonically increasing for higher values of this parameter.

Dependence on σ_0

Interestingly, the quadratic line widths subtracted the initial, that is, $\sigma^2(t) - \sigma_0^2$, generally depend on σ_0. This is neither expected for 1D diffusion (equation (6.4)), nor from the analytical model (equation (7.1)), the latter being applicable for shear purely in y-direction as discussed above. Therefore, in the case of no shear in z-direction, $\sigma^2(t) - \sigma_0^2$ is independent of σ_0. For $\partial u/\partial z \neq 0$ the dependence on the initial line width increases with increasing $\partial u/\partial z$. Further on, $\sigma^2(t) - \sigma_0^2$ for a given $\partial u/\partial z$ is higher for large σ_0 than for small. At this point a look at figure 7.6 is illustrative. The seen dependence in the case of $\partial u/\partial z \neq 0$ is a result of the shape of the temperature profile at the surface not being Gaussian. In the the absence of shear in z-direction, on the other hand, the profiles are Gaussian, and the dependence on σ_0 vanishes.

Functional dependence on time

The question on how σ^2 depends on time t remains. This was analysed by cubic spline interpolation of the simulated widths, and then taking the temporal derivative. Figure 7.7 shows this for a selection of the other parameters. As expected from equation (7.1), $\partial u/\partial y$ has t^3 as a leading power for high t. For $\partial u/\partial z$, however, the discussed boundary effect at the surface (section 7.1.1), limits it functional dependence to $\lesssim t^2$ for high t. With time, t^3 dominates, which explains the high influence by even relatively low $\partial u/\partial y$. This also justifies the choice of describing $\sigma^2(t)$ by a third grade polynomial.

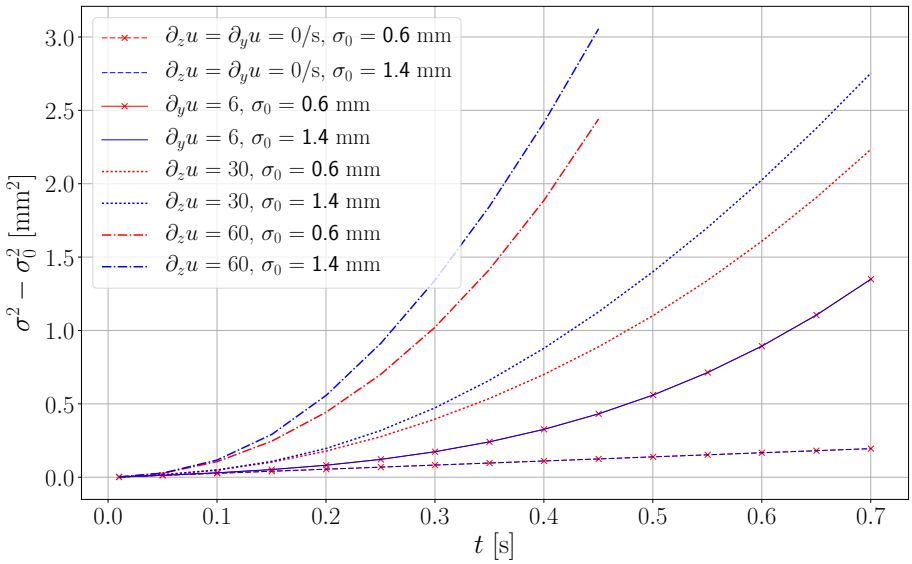

FIG 7.6.: The dependencies the quadratic line widths minus the initial ones, i.e. $\sigma^2(t) - \sigma_0^2$, for different velocity gradients. For $\partial u/\partial z \neq 0$ and $\partial u/\partial y = 0$ (dotted and dash-dotted lines), $\sigma^2 - \sigma_0^2$ at a given time is monotonically increasing with σ_0, and the influence gets higher for high values of $\partial u/\partial z$. For $\partial u/\partial z = 0$/s and $\partial u/\partial y \geq 0$ (solid and dashed lines), there is no dependence on σ_0 as expected from the analytical model, equation (7.1).

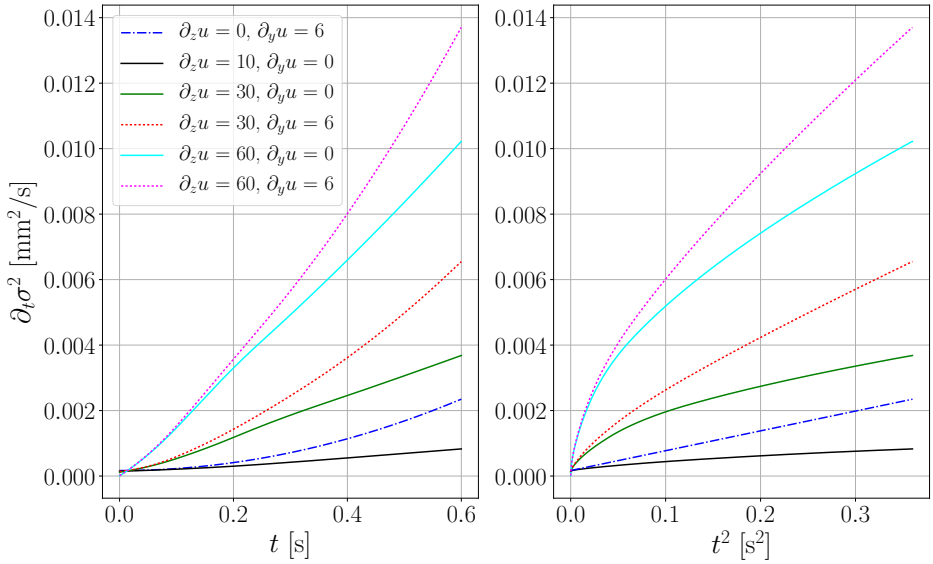

FIG 7.7.: The functional dependence of σ^2 on t, illustrated by $\partial\sigma^2/\partial t$ as function of t (left) and t^2 (right). σ^2 is about $\propto t^2$ for high t when only considering $\partial u/\partial z$ (solid lines), and about $\propto t^3$ for only $\partial u/\partial y$ (blue dash-dotted line). The latter can be understood by equation (7.1). The loss of one power in t for $\partial u/\partial z$ is due to the boundary effects form the surface. The remaining curves show $\partial\sigma^2/\partial t$ for different combinations of $\partial u/\partial y$ and $\partial u/\partial z$, see the legend.

7.2 Stationary measurements

In the following section, the results of the four stationary measurements with the wind always on, as explained in section 5.3, will be presented. The statistical approach of evaluation will be used, see section 6.2. The tree different subscripts ξ, $\bar{\xi}$ and s refer to the simulated temperature profiles calculated by equation (4.38), ie. considering the individual penetration depths in the sensitive spectrum of the camera, the profiles calculated by assuming a mean penetration depth in line with equation (4.39), and to using the temperature profile at the air-water interface directly, respectively. See figure 7.8 for the evaluation of the measurement with a wind speed setting of 10 Hz. The figure shows the measured line widths, along with the simulated curves for the obtained τ_{visc} and for $\tau_{\text{visc}} \pm 5\,\%$. Furthermore, the time intervals for both uncertainty- and evaluation of τ_{visc} are shown. The three other plots of the results for the other wind speeds, can be found in the appendix A.1.

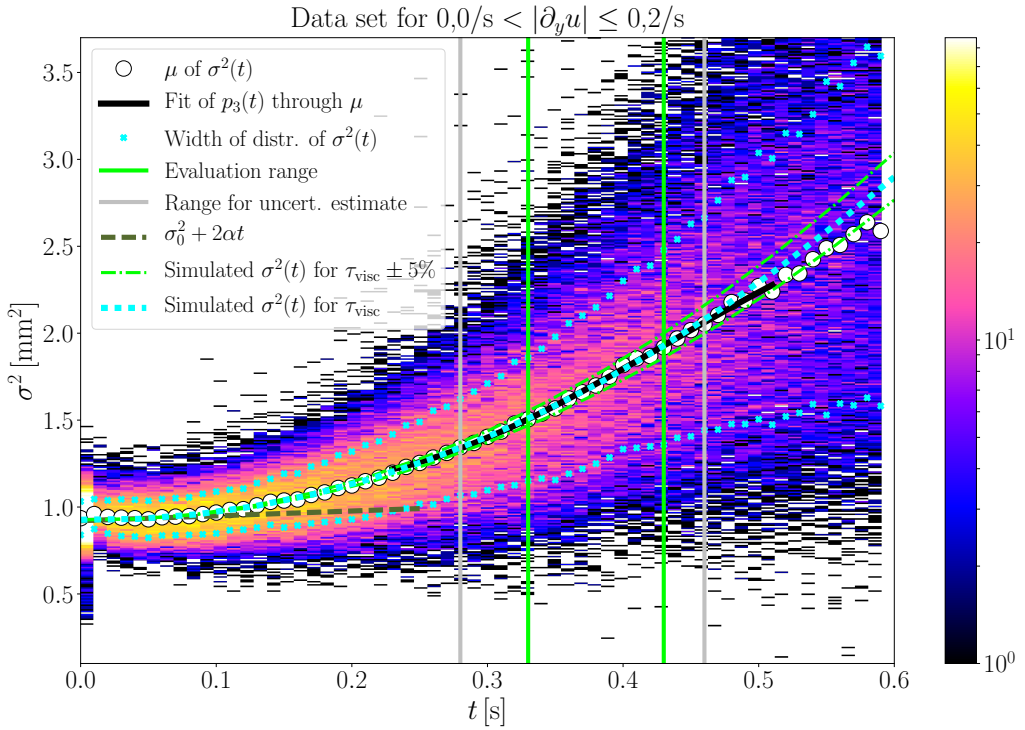

Fig 7.8.: The evaluation of the quadratic line widths $\sigma^2(t)$ for the stationary 10 Hz measurement and for negligible $\partial u/\partial y$. The figure is analogous to figure 6.10, except for additionally showing the simulated $\sigma^2(t)$ curve (cyan dotted line) based on the determined value of τ_{visc} (see table 7.1). As can be seen, the temporal development of the simulated and measured curve fits well. To give an idea of the sensitivity of the system, the lime-green dashed curves show the simulated curve for the determined $\tau_{\text{visc}} \pm 5\,\%$. Note that this does not indicate the uncertainty of the determined value for τ_{visc}.

Wind ref. [Hz]	$\tau_{\text{visc},\,\xi}$ [mPa]	$\tau_{\text{visc},\,\bar{\xi}}$ [mPa]	$\tau_{\text{visc},\,s}$ [mPa]
5.0	$8.31 \pm 0.08 \pm (0.21)_{\sigma_0}$	8.28 ± 0.08	8.51 ± 0.07
7.5	$18.03 \pm 0.08 \pm (0.16)_{\sigma_0}$	18.00 ± 0.08	18.75 ± 0.17
10.0	$31.67 \pm 0.32 \pm (0.36)_{\sigma_0}$	31.44 ± 0.30	32.95 ± 0.55
12.5	$44.59 \pm 0.48 \pm (1.35)_{\sigma_0}$	44.41 ± 0.48	47.90 ± 1.13

TABLE 7.1.: The results of the stationary measurements. See table 5.1 for the wind reference. ξ, $\bar{\xi}$ and s refer to the way of calculating the observed temperature profile in the simulation, see section 7.2. The uncertainties are calculated from the standard deviation of the returned τ_{visc}, see figure 6.10. The uncertainty with index σ_0 stems from the uncertainty in the initial widths, as explained in section 6.2, and is only estimated for $\tau_{\text{visc},\,\xi}$ as it differs little between the methods.

Wind reference [Hz]	$\tau_{\text{visc, PSV}}$ [mPa]	$\tau_{\text{turb, } z=0\text{, PSV}}$ [mPa]
5.0	7.0	-0.4
7.5	17.8	-1.4
10.0	32.0	-2.1
12.5	49.4	-5.6

TABLE 7.2.: The results obtained by the PSV method, for the upper (viscous) water layers where τ_{visc} is constant. $\tau_{\text{turb, } z=0}$ is not directly relevant, but should be zero per definition, possibly indicating that there are relevant uncertainties associated with the method.

Table 7.1 summarized the values of the shear stress obtained by the three methods (ξ, $\bar{\xi}$ and s) for all studied wind speeds. There is little difference between $\tau_{\text{visc},\,\xi}$ and $\tau_{\text{visc},\,\bar{\xi}}$. $\tau_{\text{visc},\,s}$ on the other hand, however, is somewhat higher than the other two values; in the case an wind generator frequency of 7.5 Hz, the difference is significant. This is due to the fact that considering deeper layers when calculating the simulated temperature profile, broadens it somewhat as the profiles of deeper layers are both wider and somewhat displaced relative to that of the surface. Hence, the simulated width of the heated lines, when only considering the surface layer, are smaller than in the other two cases. In turn, when comparing the simulation with the actual measurement, this leads to the need of a higher $\tau_{\text{visc},\,s}$ than $\tau_{\text{visc},\,\bar{\xi}}$ and $\tau_{\text{visc},\,\xi}$ in order to reach the measured widths. Also, the uncertainties of $\tau_{\text{visc},\,s}$ tend to be somewhat larger than for the other two. These uncertainties reflect the agreement on the shape of the temporal development of the quadratic line widths $\sigma^2(t)$ between simulation and measurement. Hence, this means that using the temperature profile at the surface directly, yields a slightly worse match between experiment and simulation than also taking deeper layers into account. Even though this points towards $\tau_{\text{visc},\,\xi}$ and $\tau_{\text{visc},\,\bar{\xi}}$ as the better choice, it needs to be emphasized that the differences is small and in most cases not significant.

As table 7.1 also shows, the uncertainties with respect to the initial widths σ_0 are larger than the standard deviations of the returned data, see section 6.2 for an explanation of these estimates. The uncertainties for σ_0 are only given for $\tau_{\text{visc},\,\xi}$, as they differ little between the methods ξ, $\bar{\xi}$ and s. They arise largely due to the unexpected temporal development shortly after heating the line (section 6.2), but also due to the slight variation of the initial width along the heated line.

The values obtained from these measurements were compared to the ones gained from PSV (section 5.2), see table 7.2. Assuming the PSV-results to be errorless, the values of $\tau_{\mathrm{visc},\,\bar{\xi}}$ and $\tau_{\mathrm{visc},\,\xi}$ are significantly deviating for the 5 Hz and 12.5 Hz measurement, when considering only the uncertainties stemming from the fluctuations of the returned data. Taking the uncertainties from σ_0 into account leaves only the 5 Hz result as a significant deviation. For $\tau_{\mathrm{visc},\,s}$, the deviations are significant for the two lowest wind settings.

The PSV-results were given without error estimates. Performing an error analysis for this method, is out of the scope for the work presented here. However, the results came with an estimate of the turbulent stress, τ_{turb}, evaluated at the interface between air and water ($z = 0$). This value should be equal to zero in the viscous layer, but is not for all of the wind settings. This might be an indication that there are some relevant uncertainties also with this method.

The viscous stress determined by PSV for the 5 Hz measurement is not constant for the whole boundary layer; it decreases somewhat for the topmost layers. A (very) close look at figure 7.9, reveals that the spline fitted through the data points tends to lie above the points (that is, closer to the surface) for layers close to the air-water interface. This corresponds to too small values of τ_{visc}, and could explain the decrease towards the surface within the viscous layer. The discrepancy to the values obtained by the thermographic approach would also shrink.

For the measurements with a wind setting of 7.5 and 10 Hz (see the appendix A.2 for the plots for the remaining wind settings), the both methods compare well as mentioned earlier. For the 12.5 Hz, however, there is a more substantial deviation. This might be caused by non-achievement of the assumption of a constant τ_{visc} in the upper 2 mm of the water body, which was assumed in the simulation, as the PSV-results show (see figure 7.10). Due to the discussed surface effects (figure 7.2) in the temperature profiles, the deeper layers also influence the broadening of the heated lines at the topmost water layers. The value obtained from the thermographic measurement corresponds to the value of $\tau_{\mathrm{visc,\,PSV}}$ reached at about 0.6 mm depth, possibly indicating that deeper layers indeed play a role. The thickness of the layer with a constant viscous shear stress is about 0.3 mm according to the PSV-values. It needs to be noted that the layer of constant τ_{visc} is about equally thick in the case of the 10 Hz measurement, without the discrepancy between the methods, thereby possibly indicating that there are other effects also playing a role in causing the deviations. The good agreement of the shape between the measured and simulated curve for the 12.5 Hz measurement supports the latter proposition.

As a final note regarding the viscous shear stress, it was also measured globally in the wind-wave facility, using an approach of momentum balance, by Schwenk [2019]. The results for τ_{visc} from the thermographic approach of this work, are about double (range: 1.4-2.1) of the values obatined by the momentum balance. For the highest wind setting the deviations were somewhat smaller. As the waves were suppressed by the surfactants, both methods should, generally speaking, yield the same result. The thermographic method measures the shear stress locally, however, and deviations from global measurements are expected due to inhomogeneities in the wind field and secondary flows due to the annular shape. Nevertheless, the discrepancies turned out to be large; the order of 20 % is expected (Bopp [2014]). Having direct measurements available from the PSV values, these agreeing reasonable well with the thermographic results, supports the inference that the results of the momentum balance are not comparable to those of the two other methods.

The lines are moving at the speed of the water surface $v_{x,\,z=0}$, which enables a simple determination of this quantity, see figure 7.11 for the 5 Hz measurement. The results

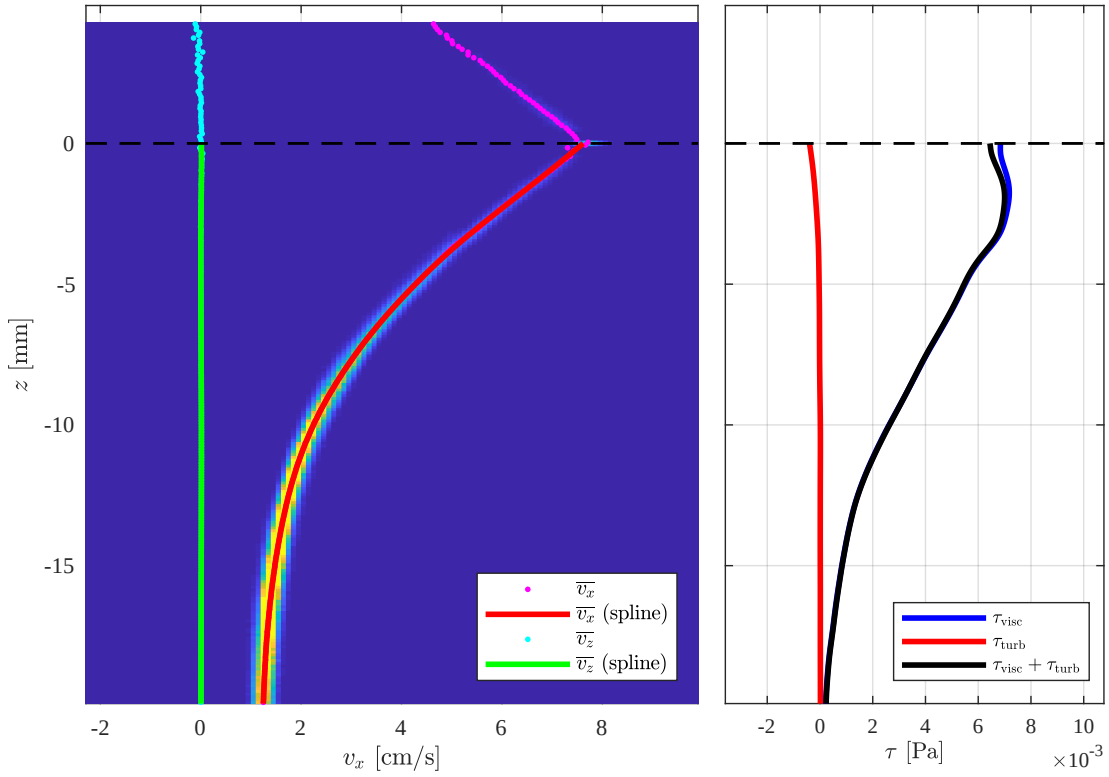

FIG 7.9.: The PSV-results of the 5 Hz stationary measurement. The left plot is showing a histogram of the detected particles with velocity v in x- and z-direction (abscissa), and the depth (ordinate). The right figure shows determined values of τ_{visc}, τ_{turb} and the sum of both. Values above $z = 0$ are due to reflections of the particles at the interface. A very close look at the left plot, reveals that the spline is laying slightly above the data points close to the surface. This corresponds to a underestimated τ_{visc}, and might correspond to the small (unexpected) decrease of τ_{visc} towards the surface. Note the narrow distribution of data points in the histogram, witnessing a little turbulence in the flow, also seen in the vanishing values of τ_{turb}.

of averaging the velocities of the individual lines are given in table 7.3. These do not deviate significantly from those obtained by PSV.

Starting from figure 2.1, it is possible to roughly determine the thickness of the viscous boundary layer δ_{visc}, i.e.

$$\delta_{\mathrm{visc}} = \frac{v_{x,\,z=0} - v_{\mathrm{bulk}}}{\partial u / \partial z}. \tag{7.2}$$

The values for v_{bulk} were obtained by PSV, and are taken from Schwenk [2019] who measured them simultaneously. The exception from this is for the 5 Hz measurement, where the value stems from the measurement shown in figure 7.9. The determined δ_{visc} are given in table 7.3, with uncertainties calculated by Gaussian uncertainty propagation of equation (7.2). Comparing these values with the PSV results (figure 7.9, A.5, A.6 and 7.10 for wind generator frequencies of 5, 7.5, 10 and 12.5 Hz, respectively) reveals, as also pointed out above, that the assumption of the shear being constant within the given δ_{visc} does not hold, especially for the three highest wind settings. This is further

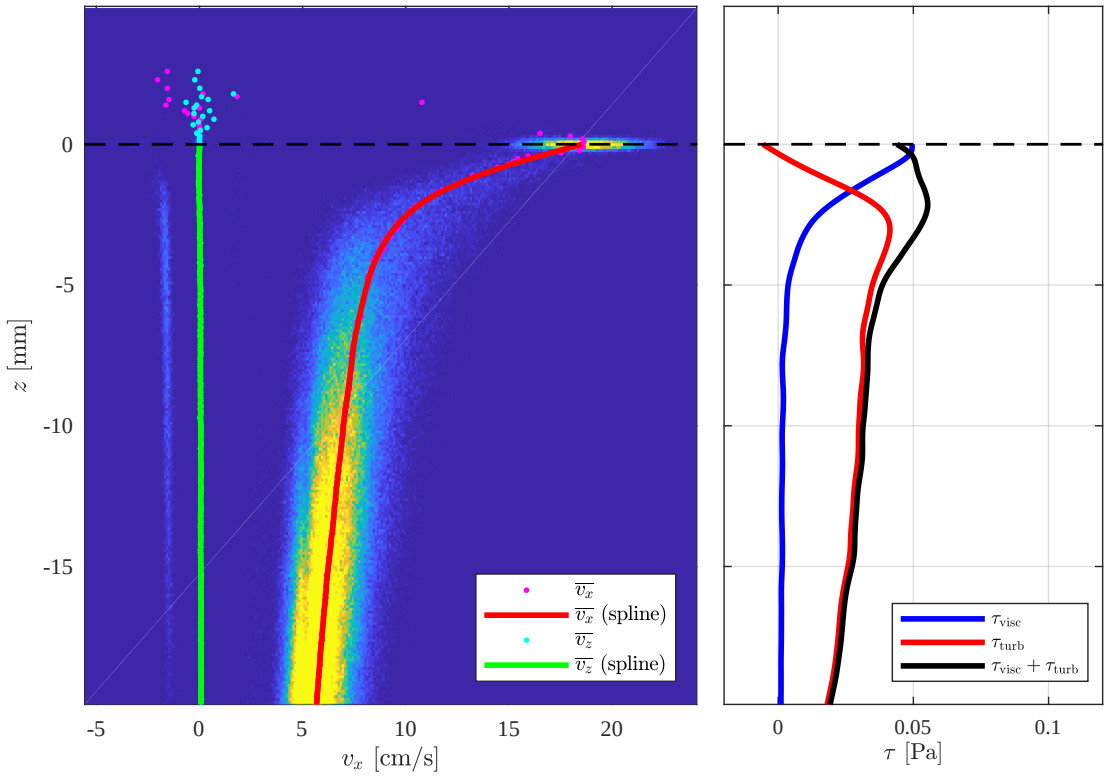

FIG 7.10.: The PSV-results for the stationary measurement with wind corresponding to 12.5 Hz. The plot is analogous to figure 7.9. Note the thin layer of constant τ_{visc} ($\sim 0.3\,\mathrm{mm}$), and a greater influence of turbulence.

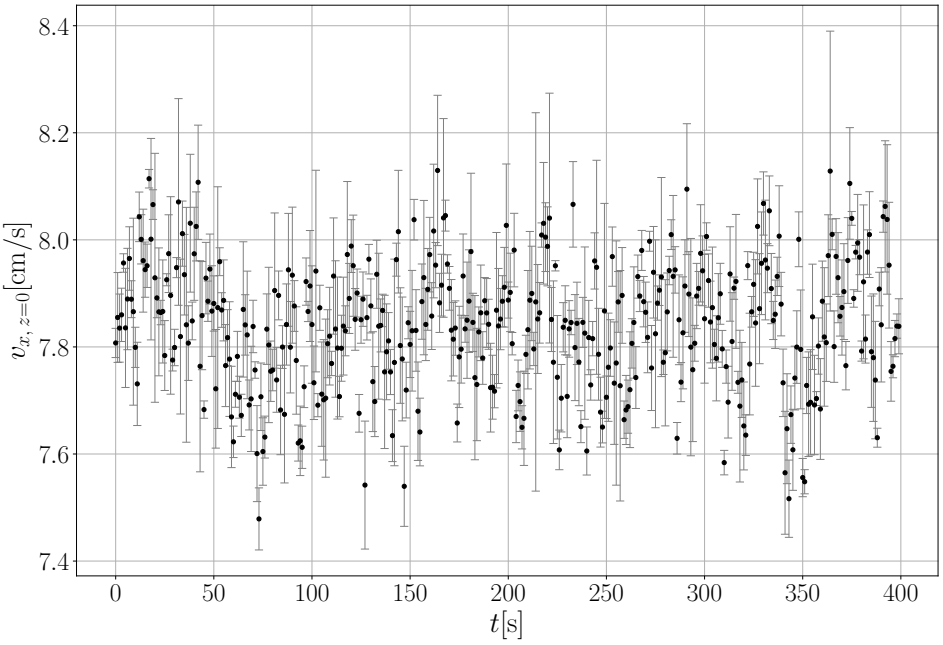

FIG 7.11.: The surface water velocity v_x of the stationary measurement, determined by the velocity of the heated lines.

Wind ref. [Hz]	$v_{x,\,z=0}$ [cm/s]	$v_{x,\,z=0,\,\mathrm{PSV}}$ [cm/s]	$v_{x,\,\mathrm{bulk},\,\mathrm{PSV}}$ [cm/s]	δ_{visc} [mm]
5.0	7.82 ± 0.15	7.6	1.2	8.0 ± 0.2
7.5	10.1 ± 0.9	10.2	2.2	4.4 ± 0.5
10.0	14.2 ± 1.2	14.6	3.1	3.5 ± 0.4
12.5	18.2 ± 1.5	18.5	4.0	3.2 ± 0.3

TABLE 7.3.: The results for the surface velocities of the thermographic method, and the determined velocity for surface and bulk (bulk velocities 7.5-12.5 Hz: taken from Schwenk [2019]). δ_{visc} denotes the estimated thickness of the viscous boundary layer.

supporting the use of a more realistic velocity profile within the boundary layer for the future simulations.

7.3 Periodic on-off measurement

The periodic on-off measurement gave the first glance at the temporal resolution possible to achieve with this method and setup. First, using the statistical approach, see section 6.2, all the data points (except those within 10 s after turning the wind on and off) were considered, yielded:

$$\tau_{\mathrm{visc},\,\xi,\,\mathrm{wind\ on}} = (33.5 \pm 0.7 \pm (0.5)_{\sigma_0})\,\mathrm{mPa},$$
$$\tau_{\mathrm{visc},\,\xi,\,\mathrm{wind\ off}} = (1.0 \pm 0.9 \pm (0.5)_{\sigma_0})\,\mathrm{mPa},$$

which is in agreement with the stationary measurement with a wind corresponding to 10 Hz (see figure 7.12), and with a value near zero (see figure A.7) for no wind and hence no shear. Nevertheless, as can be seen in the mentioned figures, there is a worse agreement between the shapes of the measured and simulated temporal development of the line widths $\sigma^2(t)$, than seen for the stationary measurement with the wind continuously on in section 7.2. The simulation assumes a constant viscous shear in the upper 2 mm of the water column, deviation from this might be able to alter the shape of the temporal development of the curve. As the wind is repeatedly turned on and off, and the measurements conducted shortly (10-50 s) after this, there might be some inconsistencies between the assumed and actual velocity profile, and hence $\tau_{\mathrm{visc,\ wind\ on}}$ in the boundary layer.

Now, turning to the higher resolved analysis with respect to time, the on-off turning of the wind gave the opportunity to see whether the method could keep track on the changes or not. The first option considered was to evaluate every single line by itself, the other was to consider 10 lines at once for each measuring point. As figure 7.14 for the evaluation of only one line at once shows, τ_{visc} is responding quickly to the changes in the wind; the build-up when turning on the wind is in the order of seconds, which is of the same order as the build-up of the wind field. The decay when turning the wind off is somewhat slower, due to the wind still moving a for while. As stated in Jähne [1980], a characteristic time scale t' for changes in τ_{visc} can be given by:

$$t' = \beta^2 \nu / u_*^2, \tag{7.3}$$

with $\beta \approx 10$ being a dimensionless scaling factor, the friction velocity u_* given by

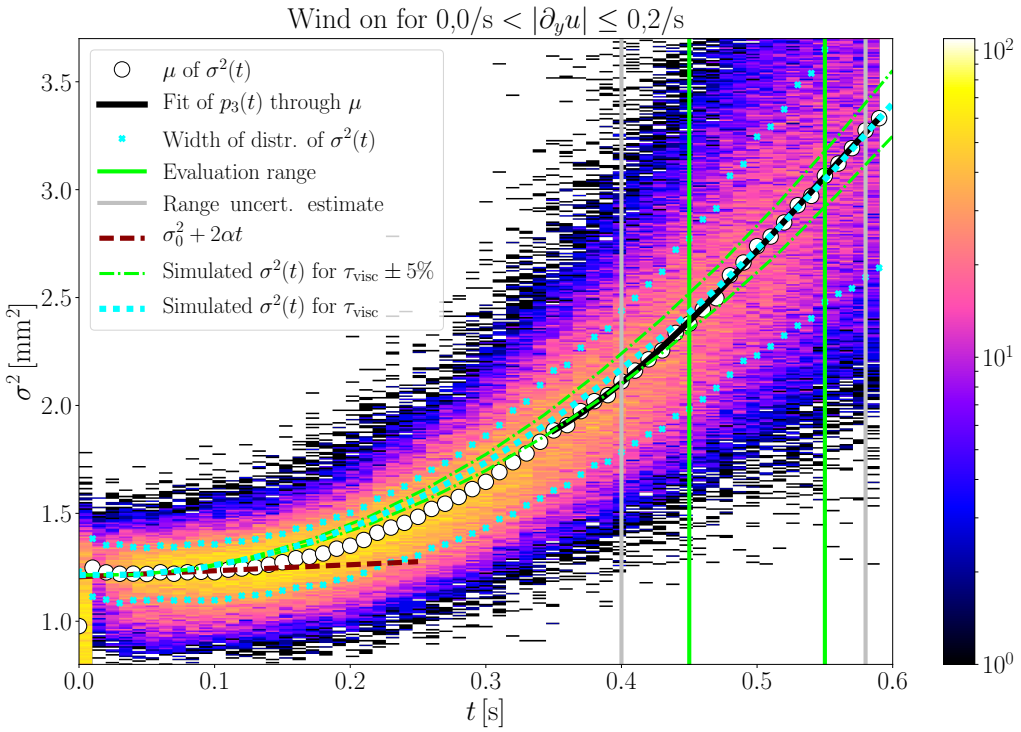

FIG 7.12.: The analysis of the wind-on part of the data set from the wind on-off measurement. Note that the shape of the simulated and measured curve differs.

equation (2.3) and $\nu = \mu/\rho$ (table 6.1) being the kinematic viscosity of water. This yields $t' \approx 3\,\mathrm{s}$. This is in the same order of magnitude of the seen changes of the viscous shear stress. Note that the build-up of the wind field is also at the time scales of seconds.

For the evaluation of only one line at once a typical challenge was the high influence of fluctuations in the flow patterns, an influence which tended to be higher with the wind turned off, whereas the line widths $\sigma^2(t)$ were easier to evaluate when the wind was turned on. See figure 7.13 for the temporal evolution for some lines, showing the rather unexpected shape caused by due to influence of flow patterns for the lines with the wind turned off. The algorithm fail if the lines are getting thinner than expected form pure diffusion, which can happen under the influence of convergences normal to the lines. This is introducing a bias towards higher τ_{visc} as a result. This is lastly a consequence of the algorithm not to fail if the line is getting thicker due to flow patterns (that is, divergences), and thereby returning too high values for τ_{visc}.

Further on, outliers towards to higher widths tended to dominate. This is partly due to the fact that the widths cannot be smaller than zero, whereas there is no upper limit. As there were not enough data points to be able to detect these outliers reliably, the results of τ_{visc} considering one or only a few lines, are generally speaking somewhat higher than those of the statistical approach, which are not prone to the influence of those outliers.

Evaluating ten lines at once, tended to diminish the challenges of short term fluctuations in the flow, leading to less scattering of the data points. Changes in the flow patterns over somewhat longer times ($\sim 10\,\mathrm{s}$) can still bee seen, and is able to explain the fluctuations in τ_{visc} for the intervals of wind off. See figure 7.14 and 7.15 for the results. Still, the tendency towards too high τ_{visc} can be seen.

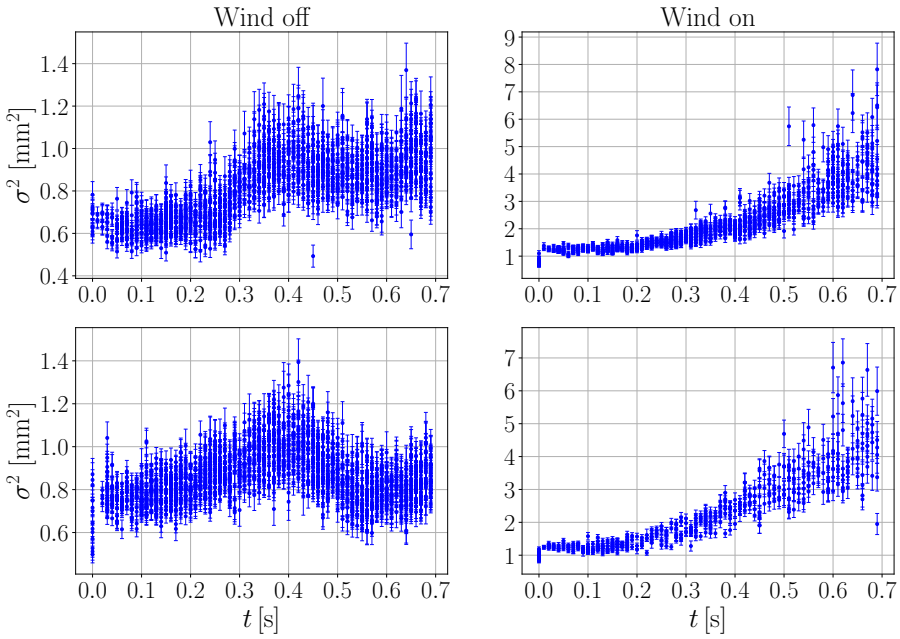

FIG 7.13.: The temporal development of the quadratic line widths $\sigma^2(t)$ for individual lines, for wind off-conditions (left) and wind on (right). Note the influence of flow patterns on $\sigma^2(t)$, altering the shape compared to the expected linear behaviour from 1D diffusion, see equation (6.4). This influence tends to be of less importance when the wind is on.

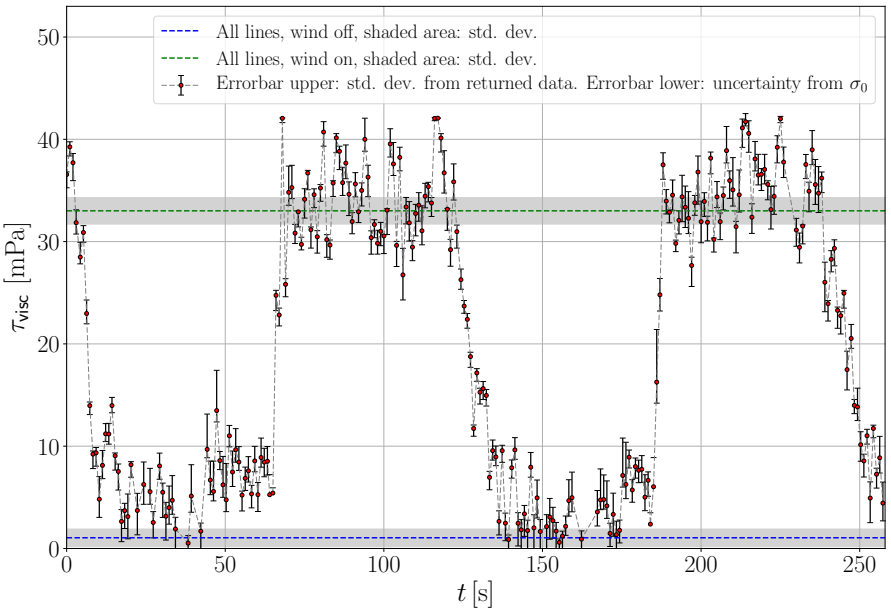

FIG 7.14.: The analysis of the wind on-off measurement considering one heated line at a time. The values tend to be too high when the wind is turned off, due to influence of flow pattern. The upper errorbars correspond to the standard deviation of the values of τ_{visc} returned from the analysis, and the lower to the uncertainty corresponding to the initial width of the line. The dotted lines show the result of the statistical approach considering all lines with the wind turned on (green, see figure 7.12) and off (blue, see figure A.7 in the appendix A.3).

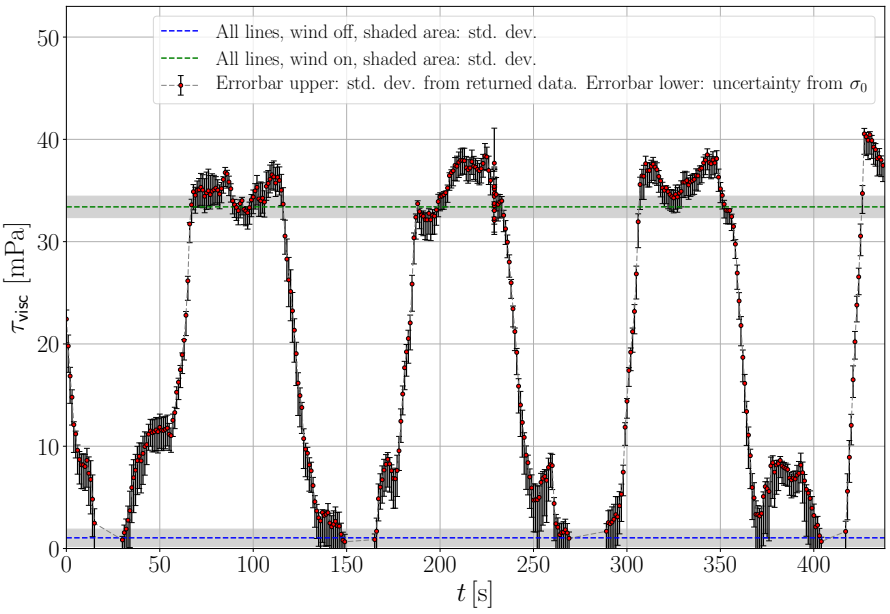

FIG 7.15.: The analysis of the wind on-off measurement considering ten heated lines at once. Otherwise, the figure is analogous to figure 7.14. Note less scattering. The determined values tend to be too high, especially for the wind turned off, due to the influence by flow patterns of on the line widths.

7.4 Non-stationary measurements

The non-stationary measurements were evaluated considering one and 15 lines at a time. For the evaluation with one line at a time, the results again tended to scatter, as seen in section 7.3, especially for longer times, see figure 7.16 for one of the 10 Hz measurements. In this figure, the wind was turned on a few seconds before the first data point seen. The first data points after the turning the wind on are missing (~ 3 s), as the water speed is too low and the lines are heated on-top of eachother and hence not evaluable. Further on, as can be seen in the figure, the scattering suddenly starts to increase, at about 80-100 s after turning on the wind. This is consistent between the other measurements of that wind setting. Also for the other wind settings, except for the lowest of 5 Hz, similar changes in the scattering can be observed, at quite consistent times for the respective wind speed. These times until the strong scattering are smaller for higher wind speeds, indicating this might be connected to distinctive changes in the flow of the water. It could, for example, be caused by a change to a regime which is more influenced by turbulence, with eddies disturbing the individual lines and hence leading to the seen scattering of the data points. The lack of this onset of high scattering for the 5 Hz measurement, can be understood little turbulence at the low wind speed, recall figure 7.9, and hence less short term fluctuations in the flow. The sudden onset of spreading of the data points happens at about 280-320 s for a wind setting of 7.5 Hz, at about 80-100 s for 10 Hz and 30-50 s for 12.5 Hz.

The evaluation of 15 subsequent lines at a time reduces the scattering due to the short time (~ 1 s) fluctuations seen above, and leaves the variations of τ_{visc} on longer scales. These turned out to be substantial. Again, the results might indicate a change of regime at the times mentioned previously, as the (periodic) fluctuations in the data becomes

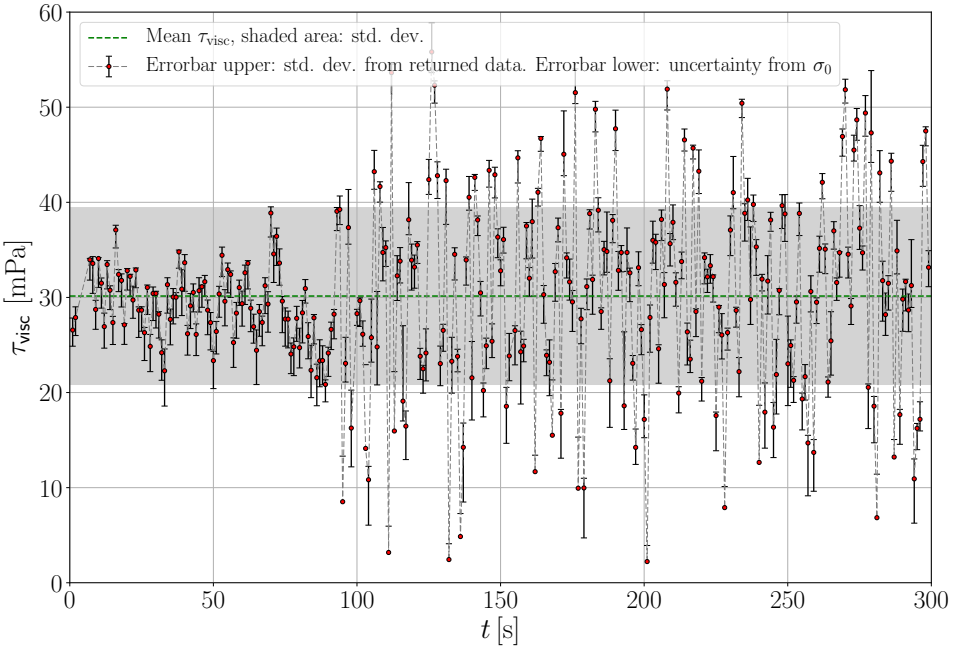

FIG 7.16.: τ_{visc} as function of time for the non-stationary measurement with a wind corresponding to 10 Hz is shown, considering every individual heated line. The wind was turned on a few seconds before the first point seen. As can be seen, the fluctuations suddenly increase at about 100 s. The upper errorbars correspond to the standard deviation of the values of τ_{visc} returned from the analysis, and the lower to the uncertainty corresponding to the initial width of the line.

larger after these points of time. However, before turning to these larger variations, the evaluation by 15 lines also showed periodic variations in the case of little turbulence, that is, for the 5 Hz measurement, see figure 7.17 below for the 15-line evaluation and figure A.8 in the appendix A.4 for the corresponding results for one line. These oscillations have a period of roughly 40 s, being about similar for the 7.5 Hz measurement. For comparison, also the *stationary* 5 Hz measurement show this oscillation, see figure A.4 in the appendix A.1, indicating it has nothing to do with the non-stationary conditions. What causes these periodic variations remains an open question. It could be they are caused by an increasing shear, which, when reaching a critical value, relieves over the course of time, and then builds up again. Figure A.8 indicates that the suggested build-up of τ_{visc} happens rather quickly, in agreement with the findings of section 7.3, followed by a slower degradation. It seems to not be connected to the flow velocity, see figure 7.18, at this quantity does not show the same oscillations.

Further on, what also can be seen in figure 7.17 for the *non-stationary* 5 Hz measurement, is an overshoot of τ_{visc} immediately after turning the wind on. As corresponds to the very beginning of the measurement, with deeper water layers being little influenced by the momentum transfer from the wind. Hence, it could be that lack of fluctuations of the flow velocities of the deeper layers allow for a somewhat higher critical τ_{visc}, leading to the overshoot. For the other wind settings, the overshoot was mostly not seen, possible with some exceptions for the 7.5 Hz measurement. It must be noted, however, that when

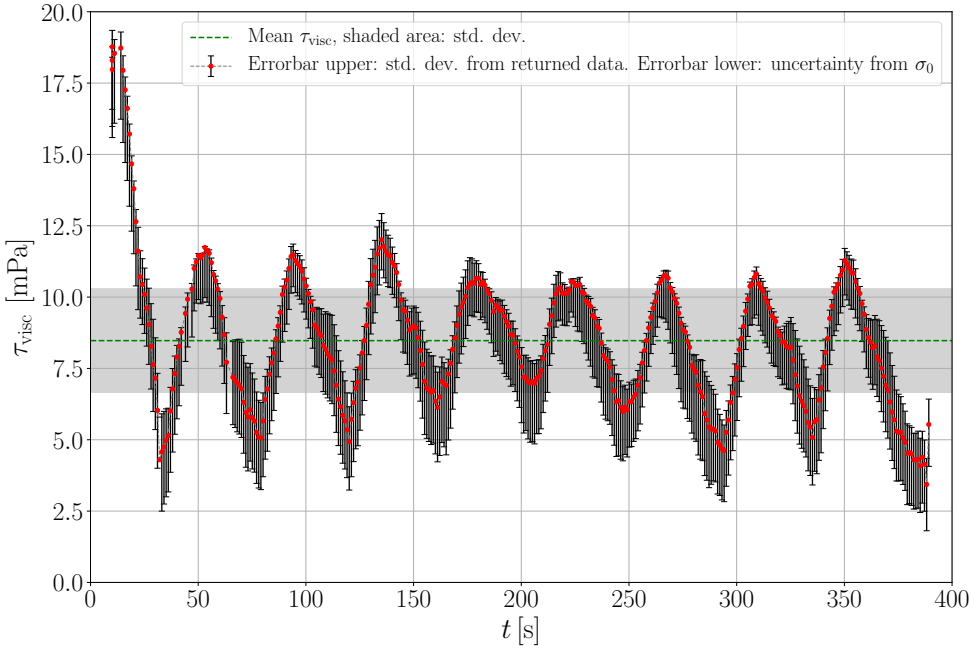

FIG 7.17.: The evaluation of τ_{visc} as function of time, showing the non-stationary measurement with a wind corresponding to 5 Hz, considering 15 heated lines at once. Otherwise, the figure is analogous to figure 7.16. Notice the overshoot at the beginning of the measurement (first data point corresponding to a ~ 3 s after turning the wind on), and the oscillation with a period of about 40 s.

assuming the duration of the overshoot to decrease with higher wind speeds, as the shear increases, and considering that the couple of first data points after turning the wind on are lost as explained above, the absence of the overshoot in the measurements at the other wind settings does not rule out that might they are taking place.

Turning to the regime change, the evaluation of 15 lines at a time of the 10 Hz measurement is shown in figure 7.19. As can be seen in the figure, τ_{visc} starts to vary strongly at about the same time as the onset of the high scattering in figure 7.16, which is showing the same measurement. This means that the fluctuations seen for the evaluation of one line, are not randomly distributed, but follow some variations of longer time scales. Interestingly, a marked drop in the surface velocity can also be seen at the same time as the strong fluctuations in τ_{visc} start, see figure 7.20. This overshoot in the surface velocity can be seen in all measurements except for those conducted at a wind reference of 5 Hz, in which also the enhanced scattering of τ_{visc} is absent. The change in surface velocity could be another indication of the scattering actually being caused by a change of regime in the flow. Further figures for the other measurements can be found in the appendix A.4.

The mean values obtained from considering 15 lines at once, for times higher than 50 s since turning on the wind, can also be given, as these tend to oscillate around a fixed $\bar{\tau}_{visc}$, as seen in the mentioned figures. The result of this, seen in table A.1 in the appendix A.4, can then again be averaged for the different measurements, results are given in table 7.4. Note that the uncertainties given in table 7.4 refer to the deviations between the measurements, and not to the amplitudes of the fluctuations seen within one. The values for the three lowest wind settings are in good agreement with those obtained form the stationary measurement, for the highest wind setting, the result is

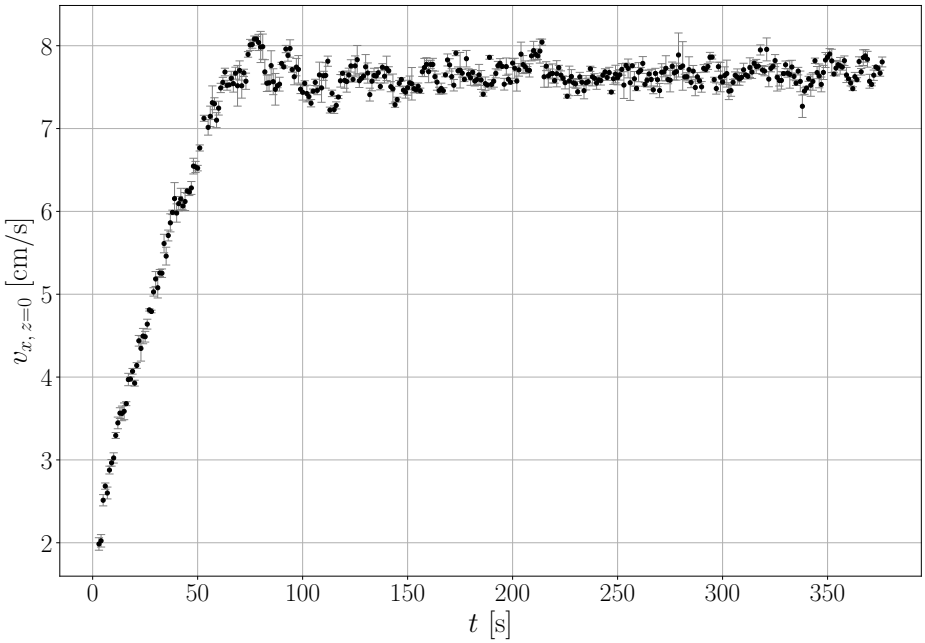

FIG 7.18.: The surface velocity v_x of the 5 Hz non-stationary measurement as function of time since the wind was turned on. As can be seen, the velocity does not show the same oscillation as τ_{visc} (figure 7.17), suggesting the oscillations to be independent of that parameter.

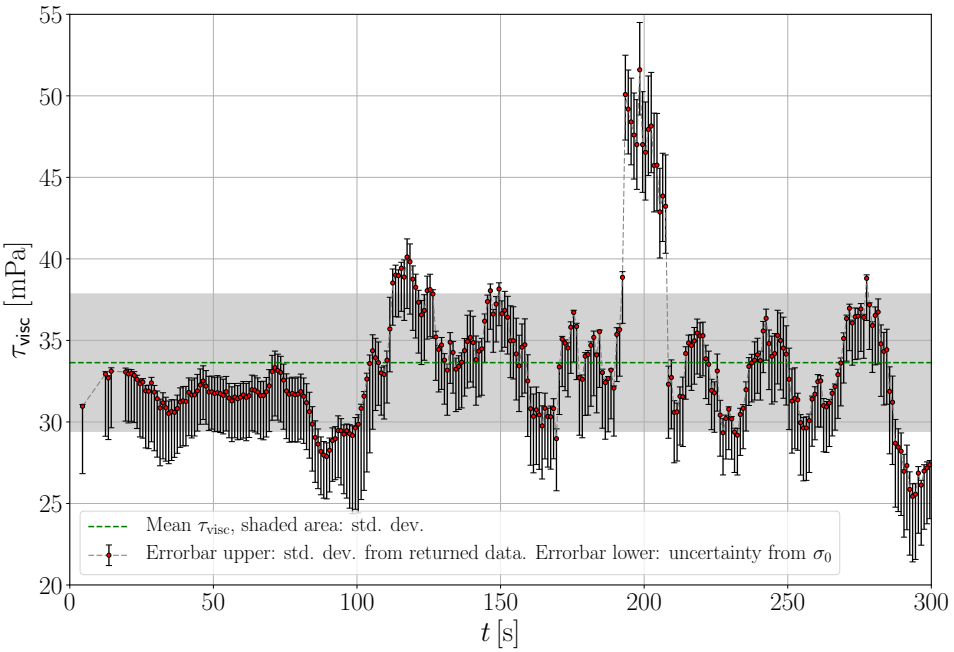

FIG 7.19.: The evaluation of τ_{visc} as function of time since the wind was turned on. The measurement is the same as in figure 7.16, but now considering 15 heated lines at once. Else the figure is analogous. Notice the variation in τ_{visc} beginning at about the same time as the high fluctuations seen when considering only one line.

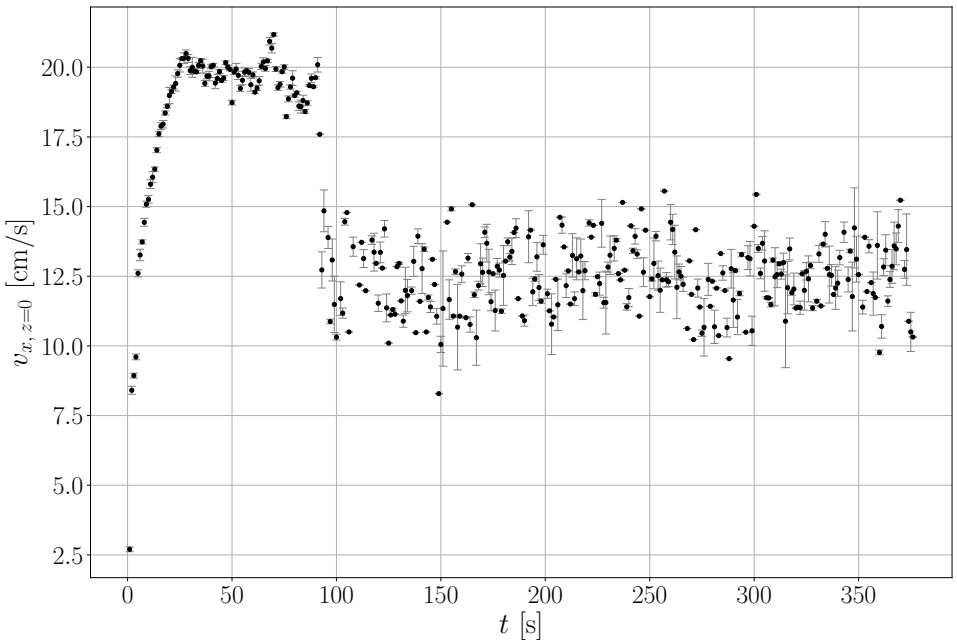

FIG 7.20.: The surface velocity v_x of the 10 Hz non-stationary measurement as function of time since the wind was turned on. There is a marked drop of the velocity the same time as the onset of the enhanced scattering in τ_{visc} of the data points in figure 7.16, suggesting that there is indeed a change of regime.

higher and significantly deviating. This value is possibly even too low, as the simulated values of τ_{visc} stopped at about 65 mPa (chosen limit in the scope of this work), hence leading to a cut-off at this value. Figure A.14 in A.4 shows that this could be the case.

For one of the non-stationary measurements at 12.5 Hz, an analysis considering the dataset after 200 s (hereby being about stationary, and hence the statistical approach, see section 6.2, could be applied), yielded a result of $\tau_{\text{visc},\,\xi} = (48.7 \pm 0.7)$ mPa, see figure A.15 in the appendix A.4. Compared to $\bar{\tau}_{\text{visc}} = (55 \pm 5)$ mPa from considering 15 lines at once, this is not deviating significantly. The large uncertainty in $\bar{\tau}_{\text{visc}}$ reflects the discussed fluctuations. The discrepancy between the statistical approach and taking the mean of the temporal resolved values, and between the stationary and non-stationary measurements, are higher at this wind speed than for the others. It is possible that this reflects the problem of outliers mentioned in section 7.3, where the strongly deviating values towards high line widths tend to dominate over those tending to small widths. With higher wind speed, the influence of outliers become more prominent. As there are not enough data points to reliably discard these values when evaluating only few lines, this might explain the inconsistency between the methods. It could possibly also indicate that the thermographic method is reaching its limits. The latter could be supported by $\tau_{\text{visc},\,\xi}$ deviating significantly from the thermographic result of the stationary measurement of that frequency (table 7.1), but not for the stationary PSV reference measurement.

Wind reference [Hz]	$\bar{\tau}_{\text{visc},\,\xi}$ [mPa]
5.0	8.31 ± 0.13
7.5	17.95 ± 0.34
10.0	33.6 ± 1.1
12.5	57 ± 1.5

TABLE 7.4.: The averaged results of the non-stationary measurements, for $t \geq 50\,\text{s}$ after turning the wind on. The agreement to the stationary measurements is good (table 7.1), except for the 12.5 Hz measurement, which deviates significantly.

7.5 Features regarding the shear in y-direction

The last thing that briefly will be mentioned, is an interesting observation related to gradients in y-direction, which have been completely disregarded until now. It turns out, that it makes a difference whether positive or negative gradients are considered. This asymmetry can be seen independent on the wind generator frequency.

As figure 7.21 shows, the line widths at a given time for negative values of $\partial u/\partial y$, are much higher than for positive $\partial u/\partial y$ and higher than the corresponding simulated widths. This is probably due to some sort of divergences happening for negative y gradients, causing the excess broadening of the line. The widths for positive gradients behave oppositely, mostly being lower than the simulated and hence corresponding to a divergence. A brief look at figure 7.22 supports the given explanation, with the movement of the structure in the middle moving toward the inner wall of the channel. This is as expected from the annual shape of the wind-wave facility. However, such clearly con- and diverging structures are not always seen, see for example figure 6.5. The convergence could maybe cause so called streaks, i.e. stripe-like thickening of the viscous layer in wind direction, see Klein [2019] and Kräuter et al. [2014] for more information on this topic.

For even higher $\partial u/\partial y$, the widths of both positive and negative gradients tend to be higher than the simulated ones, with those corresponding to the negative ones still being the highest, see figure 7.23. A further, more detailed and quantitative investigation of this phenomenon is out of the scope for this work, but it beautifully illustrates the complexity of this, at a first glance, rather simple system.

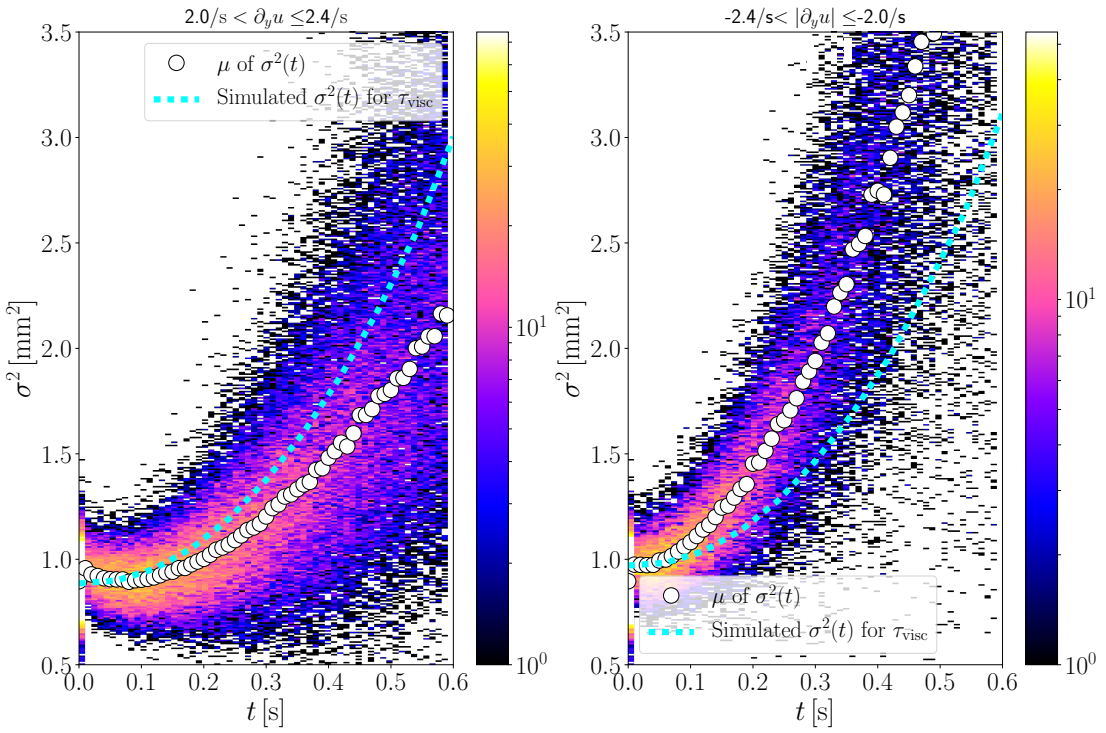

FIG 7.21.: The quadratic line widths $\sigma^2(t)$ form the stationary 10 Hz measurement, for $\partial u/\partial y$ of (+2.2± 0.2)/s (left) and (-2.2±0.2)/s (right). The simulated curve for $\partial u/\partial y$ and τ_{visc} from table 7.1, is also shown (cyan dotted line). The widths for positive gradients in y-direction, lay below those of negative.

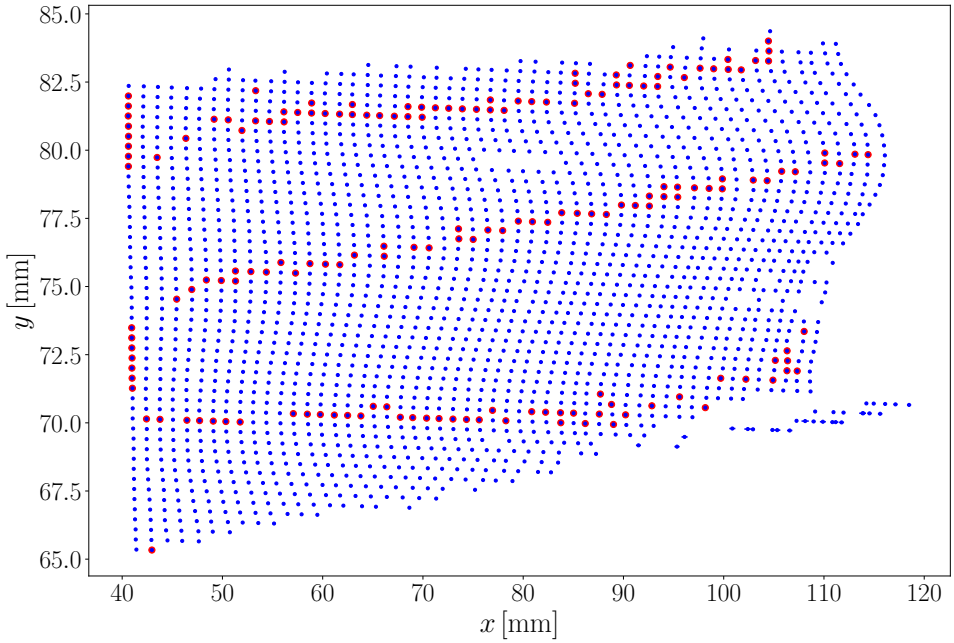

FIG 7.22.: The figure shows one heated line every 10 ms, with $t = 0$ to the left. The wind direction is in positive x-direction, and the inner wall of the channel towards high y. The red dots correspond to $\partial u/\partial y$=0, and are indicating the flow patterns (recall section 6.2). These tend to not be parallel, hence leading to a convergence in the upper part of the figure (negative angles, corresponding to negative values of $\partial u/\partial y$), and divergences for positive angles. This could explain the behaviour of the line widths seen in figure 7.21.

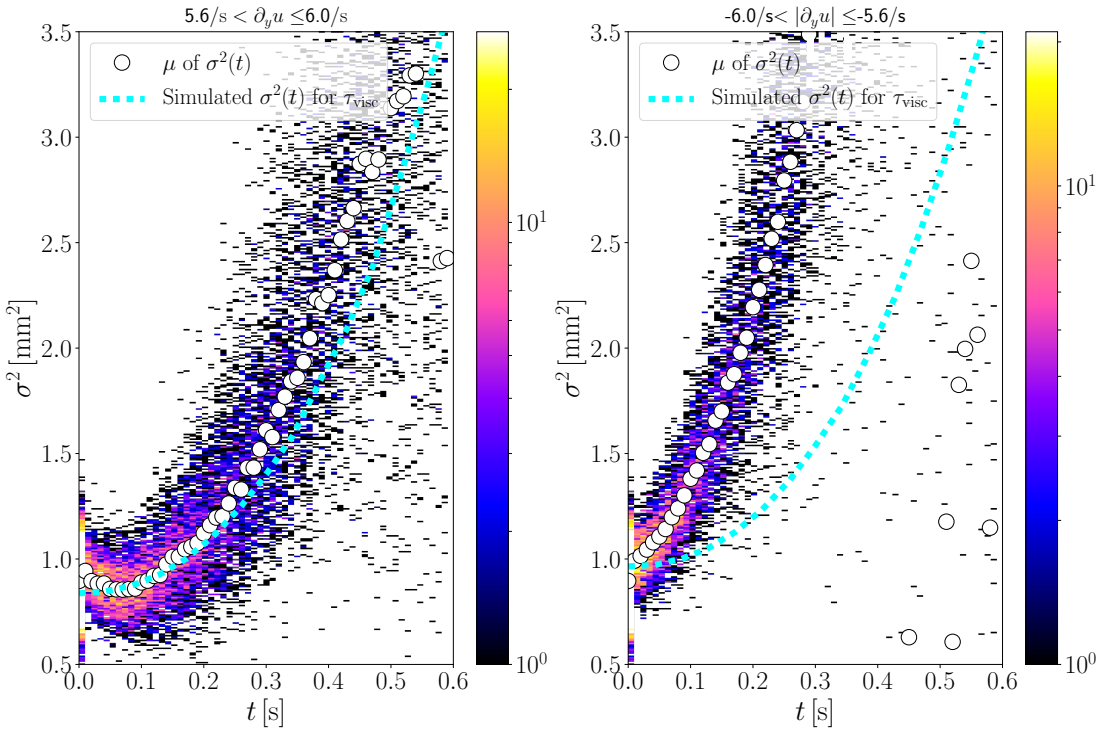

FIG 7.23.: The figure is analogous to figure 7.21, but shows higher $\partial u/\partial y$. The width for negative gradients still lie above those of positive, but now both cases lead to a broadening higher than that simulated. Note the decrease in the line widths for small times in the left figure, and not in the right. This could possibly be due to the initial angle of the heated line, being about $\theta_{s0} = -2.3°$, which for positive $\partial u/\partial y$ first needs to be "overcome", before line starts to tilt with positive angles. The curve for negative $\partial u/\partial y$ is, however, still steeper than for positive gradients.

8 Summary and outlook

The local viscous shear stress τ_{visc} in the watersided boundary layer was measured using a thermographic approach in an annular wind-wave facility, at wind velocities at 10 m height u_{10} of up to roughly 6.1 m/s. The surfactant Triton X-100 was used to suppress the waves. The method is based on heating thin lines with a near-infrared laser on the water surface, and monitoring the broadening of this line with time. The broadening is dependant on the velocity gradient of the flow with depth, that is, $\partial u/\partial z$, at the surface. Assuming this gradient to be constant in the viscous boundary layer yields a constant $\tau_{\text{visc}} \propto \partial u/\partial z$. This enables the determination of the viscous shear by monitoring the broadening of the heated lines.

In order to be able to connect the measured broadening of the line widths $\sigma(t)$ to the respective τ_{visc}, $\sigma(t)$ was simulated for relevant values of the initial line width σ_0 and the spatially constant components of the velocity gradient with depth ($\partial u/\partial z$) and the direction parallel to the line ($\partial u/\partial y$). Using these results, τ_{visc} was interpolated as a function of $\sigma^2(t)$, σ_0 and $\partial u/\partial y$. The measured line widths could then be passed on to this function along with the other parameters, yielding the τ_{visc} as output. $\partial u/\partial y$ could be estimated by calculating the time dependent angles of the measured lines, see section 6.2.

The results of the measurements under stationary conditions show a good agreement between the described method and a reference measurement using particle tracking (PSV-method, section 5.2) to determine τ_{visc} directly. The discrepancies between the results of the two methods are smaller than 20 % for the considered wind speeds. It should be emphasized that thermographic method is superior to the PSV method regarding the experimental setup, as neither particles nor water-sided cameras are needed.

The heated lines in these experiments had a length of about 2 cm. This yields relatively few data points, especially when discarding the endpoints of the line in order to diminish the evaluation of data points not agreeing with the simulated conditions. A longer line would give more data points, and a better representation of the conditions as small scale fluctuations in the flow patterns would influence the measurements less. This would also enable a better temporal resolution, as less lines are needed to acquire a sufficient amount of data points. That being said, with the used setup, it is possible to achieve reasonable values for τ_{visc} with a temporal resolution of ~ 1 s for most measurement conditions.

There is still room for improvement when it comes to the data analysis, especially in the case of a high temporal resolution. Outliers tend to have a relatively large influence, and should be detected and removed reliably. Similarly, lines affected by con- and divergences in the flow, leading to incorrect results, should be removed. This would again be simplified by obtaining more data points with a longer line. Regarding the rest of the analysis, a better uncertainty estimation is needed, as the uncertainties tend to be small and reflecting the output of the algorithm rather than physical uncertainties

and assumptions of the simulation.

The method presented in this thesis was found to work best at low, but not zero, wind speeds. For no wind, artefacts not related to τ_{visc} tended to become important. For higher wind speeds, the method tends to deliver more unreliable results, and is possibly restrained by the lack of data points for proper statistics or simply reaching its limits. Further testing is required. A possible improvement for higher wind speeds would be to simulate the system with more realistic velocity profiles than done in this work, for example gained from the PSV-method.

Due to the localized measurements and promising temporal resolution, combining this method with laser induced fluorescence (LIF), which is measuring concentration profiles and localized gas transfer rates (Friedl [2013], Arnold [2015]), could yield interesting results. Of course, this also applies to other measurement techniques, such as boundary layer imaging (Kräuter et al. [2014]), which measures the thickness of the mass boundary layer with high spacial resolution. Air-sided PSV for comparison between the viscous layers of the two compartments can also yield valuable insights. Another interesting application could be combining the method of this work along with the image processing algorithms and methods described in (Lu et al. [accepted 2019]), that is, analysing flow characteristics by images obtained from passive thermography.

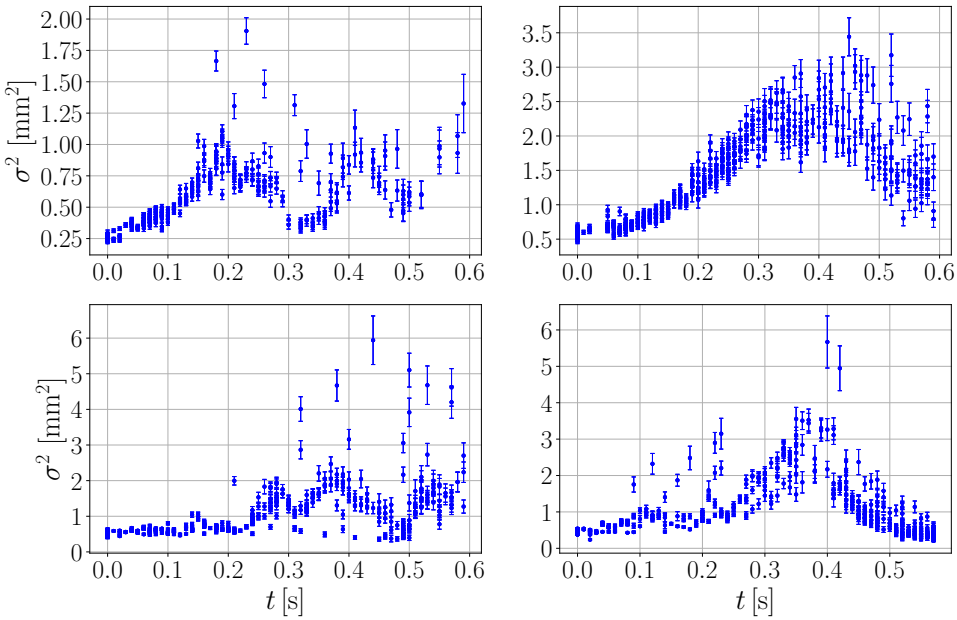

FIG 8.1.: The temporal development of the quadratic line widths $\sigma^2(t)$ for four lines, under wavy conditions. The dynamics of the waves, leading to a stretching and compressing of the surface layer, can be seen as the oscillatory behaviour of $\sigma^2(t)$. Note the different scales.

Last, but not least, the experiments were conducted without waves. For the method to become applicable under a wider range of conditions, it should be able to handle waves. This is not the case, as it turned out, because the waves are stretching and compressing the water surface. The widths of the heated lines are therefore oscillating, this effect being pronounced, and making the algorithm used in this work fail. See figure 8.1 for some examples of the temporal development of the line widths for some individual lines. Further on, it is not clear how these div- and convergences of the surface are affecting the broadening of the lines. Lastly, τ_{visc} is not constant over the wave phase (Bopp [2018]). This would lead to a different broadening of the lines, depending on where on the wave the line is heated. Interferences between more waves are additionally complicating the situation. In any case, more studies and an improvement of the evaluation procedure concerning wavy conditions are needed.

Bibliography

Akela Laser Cooperation, 1470 nm / 4.5 W Laser Diode on C-mount ALC-1470-04500-CMT-125, data sheet, 2017.

Arnold, N.: Visualisierung des Gasaustauschs an der windbewegten Wasseroberfläche mittels vertikaler Konzentrationsfelder von gelöstem Sauerstoff quer zur Windrichtung, Bachelor's thesis, Institute of Environmental Physics, Department of Physics and Astronomy, University of Heidelberg, Germany, doi:10.11588/heidok.00018411, 2015.

Bopp, M.: Luft- und wasserseitige Strömungsverhältnisse im ringförmigen Heidelberger Wind-Wellen-Kanal (Aeolotron), Master's thesis, Institute of Environmental Physics, Department of Physics and Astronomy, University of Heidelberg, Germany, doi:10.11588/heidok.00017151, 2014.

Bopp, M.: Air-Flow and Stress Partitioning over Wind Waves in a Linear Wind-Wave Facility, Dissertation, Institute of Environmental Physics, Department of Physics and Astronomy, University of Heidelberg, Germany, Heidelberg, doi:10.11588/heidok.00024741, 2018.

Charnock, H.: Wind stress on a Water Surface, Q.J.R. Meteorol. Soc, 81, 639–640, 1955.

Crank, J.: The Mathematics of Diffusion, Clarendon Press, Oxford, 2nd edn., 1975.

Crueger, T., Roeckner, E., Raddatz, T., Schnur, R., and Wetzel, P.: Ocean dynamics determine the response of oceanic CO2 uptake to climate change, Climate Dynamics, 31, 151–168, doi:10.1007/s00382-007-0342-x, URL `https://doi.org/10.1007/s00382-007-0342-x`, 2008.

Downing, H. D. and Williams, D.: Optical constants of water in the infrared, Journal of Geophysical Research (1896-1977), 80, 1656–1661, doi:10.1029/JC080i012p01656, URL `https://agupubs.onlinelibrary.wiley.com/doi/abs/10.1029/JC080i012p01656`, 1975.

Emmel, A.: Bestimmung der Geschwindigkeit und des Geschwindigkeitsgradienten an der windgetriebenen Wasseroberfläche, Bachelor's thesis, Institute of Environmental Physics, Department of Physics and Astronomy, University of Heidelberg, Germany, doi:10.11588/heidok.00023754, 2017.

Fernando, H., ed.: Handbook of Environmental Fluid Dynamics, vol. 1, CRC Press, Boca Raton, doi:https://doi.org/10.1201/b14241, 2013.

Friedl, F.: Investigating the Transfer of Oxygen at the Wavy Air-Water Interface under Wind-Induced Turbulence, Dissertation, Institute of Environmental Physics,

Department of Physics and Astronomy, University of Heidelberg, Germany, doi: 10.11588/heidok.00014582, 2013.

Garbe, C. S., Degreif, K., and Jähne, B.: Estimating the viscous shear stress at the water surface from active thermography, in: Transport at the Air Sea Interface — Measurements, Models and Parameterizations, edited by Garbe, C. S., Handler, R. A., and Jähne, B., pp. 223–239, Springer-Verlag, Berlin, Heidelberg, doi:10.1007/978-3-540-36906-6_16, 2007.

Gruber, N., Clement, D., Carter, B. R., Feely, R. A., van Heuven, S., Hoppema, M., Ishii, M., Key, R. M., Kozyr, A., Lauvset, S. K., Lo Monaco, C., Mathis, J. T., Murata, A., Olsen, A., Perez, F. F., Sabine, C. L., Tanhua, T., and Wanninkhof, R.: The oceanic sink for anthropogenic CO_2 from 1994 to 2007, Science, 363, 1193–1199, doi:10.1126/science.aau5153, URL `https://science.sciencemag.org/content/363/6432/1193`, 2019.

Gutsche, M.: Surface Velocity Measurements at the Aeolotron by Means of Active Thermography, Masterarbeit, Institute of Environmental Physics, Department of Physics and Astronomy, University of Heidelberg, Germany, doi:10.11588/heidok.00017431, 2014.

Haußecker, H.: Messung und Simulation von kleinskaligen Austauschvorgängen an der Ozeanoberfläche mittels Thermographie, Dissertation, IWR, Institute of Environmental Physics, Department of Physics and Astronomy, University of Heidelberg, Germany, doi:10.5281/zenodo.14789, 1996.

Hoegh-Guldberg, O., Cai, R., Poloczanska, E., Brewer, P., Sundby, S., Hilmi, K., Fabry, V., and Jun, S.: The Ocean. In: Climate Change 2014: Impacts, Adaptation, and Vulnerability. Part B: Regional Aspects. Contribution of Working Group II to the Fifth Assessment Report of the Intergovernmental Panel on Climate Change [Barros, V.R., C.B. Field, D.J. Dokken, M.D. Mastrandrea, K.J. Mach, T.E. Bilir, M. Chatterjee, K.L. Ebi, Y.O. Estrada, R.C. Genova, B. Girma, E.S. Kissel, A.N. Levy, S. MacCracken, P.R. Mastrandrea, and L.L. White (eds.)], Cambridge University Press, Cambridge, United Kingdom and New York, NY, USA, pp. 1655-1731, 2014.

Holtmann, L. G.: Aufbau eines aktiven Thermographiesystems zur Messung des Geschwindigkeitsgradienten in der windgetriebenen wasserseitigen viskosen Grenzschicht, Bachelor's thesis, Institute of Environmental Physics, Department of Physics and Astronomy, University of Heidelberg, Germany, doi:10.11588/heidok.00023754, 2017.

Ilmberger, J.: Impulsübertrag und Strömungsverhältnisse in einem runden Wind-Wasser Kanal, Diplomarbeit, Institute of Environmental Physics, Department of Physics and Astronomy, University of Heidelberg, Germany, doi:10.5281/zenodo.13346, iUP D-167, 1981.

Jähne, B.: Zur Parametrisierung des Gasaustauschs mit Hilfe von Laborexperimenten, Dissertation, Institute of Environmental Physics, Department of Physics and Astronomy, University of Heidelberg, Germany, doi:10.11588/heidok.00016796, iUP D-145, Link Nationalbibliothek http://d-nb.info/810123614, 1980.

Jähne, B.: Digitale Bildverarbeitung, Springer, Berlin, 7 edn., doi:10.1007/b138991, 2012a.

Jähne, B.: Atmosphere-water exchange, in: Encyclopedia of Sustainable Science and Technology, edited by Meyers, R. A., vol. 1, pp. 594–606, Springer, doi:10.1007/978-1-4419-0851-3_644, 2012b.

Klein, A.: The Fetch Dependency of Small-Scale Air-Sea Interaction Processes at Low to Moderate Wind Speeds, Dissertation, Institute of Environmental Physics, Department of Physics and Astronomy, University of Heidelberg, Germany, doi:10.11588/heidok.00026559, 2019.

Krall, K. E.: Laboratory Investigations of Air-Sea Gas Transfer under a Wide Range of Water Surface Conditions, Dissertation, Institute of Environmental Physics, Department of Physics and Astronomy, University of Heidelberg, Germany, doi:10.11588/heidok.00014392, 2013.

Kroeker, K. J., Kordas, R. L., Crim, R., Hendriks, I. E., Ramajo, L., Singh, G. S., Duarte, C. M., and Gattuso, J.-P.: Impacts of ocean acidification on marine organisms: quantifying sensitivities and interaction with warming, Global Change Biology, 19, 1884–1896, doi:10.1111/gcb.12179, URL https://onlinelibrary.wiley.com/doi/abs/10.1111/gcb.12179, 2013.

Kräuter, C., Trofimova, D., Kiefhaber, D., Krah, N., and Jähne, B.: High resolution 2-D fluorescence imaging of the mass boundary layer thickness at free water surfaces, jeos, 9, 14 016, doi:10.2971/jeos.2014.14016, 2014.

Kunz, J.: Active Thermography as a Tool for the Estimation of Air-Water Transfer Velocities, Ph.D. thesis, Institute of Environmental Physics, Department of Physics and Astronomy, University of Heidelberg, Germany, doi:10.11588/heidok.00022903, 2017.

Lide, D. R. and Frederikse, H. P. R.: CRC Handbook of Chemistry and Physics, CRC Press, Inc. Boca Raton , FL, 1995.

Liss, P. S. and Johnson, M. T., eds.: Ocean-Atmosphere Interactions of Gases and Particles, Springer, doi:10.1007/978-3-642-25643-1, URL http://link.springer.com/book/10.1007/978-3-642-25643-1, 2014.

Lu, G., Tsai, W., and Jähne, B.: Decomposing Infrared Images of Wind Waves for Quantitative Separation into Characteristic Flow Processes, IEEE Transactions Geosciences and Remote Sensing, doi:10.1109/TGRS.2019.2920280, accepted 2019.

Münnich, K. and Flothmann, D.: Gas exchange in relation to other air/sea interaction phenomena, in: SCOR Workshop on "Air/Sea Transport of Pollutants", Miami, doi:10.5281/zenodo.13345, 1975.

Rembeck, L. S.: Geschwindigkeit- und Geschwindigkeitsgradientenmessung an der windgetriebenen Wasseroberfläche mittels aktiver Thermographie, Bachelor's thesis, Institute of Environmental Physics, Department of Physics and Astronomy, University of Heidelberg, Germany, 2018.

Roy-Barman, M. and Jeandel, C.: Marine Geochemistry: Ocean Circulation, Carbon Cycle and Climate Change, 2016.

Schwenk, C.: Messung der Schubspannungsgeschwindigkeit am Heidelberger Aeolotron unter instationaren Bedingungen, Bachelor's thesis, Institute of Environmental Physics, Department of Physics and Astronomy, University of Heidelberg, Germany, 2019.

A | Appendix

A.1
Stationary measurements, thermographic results

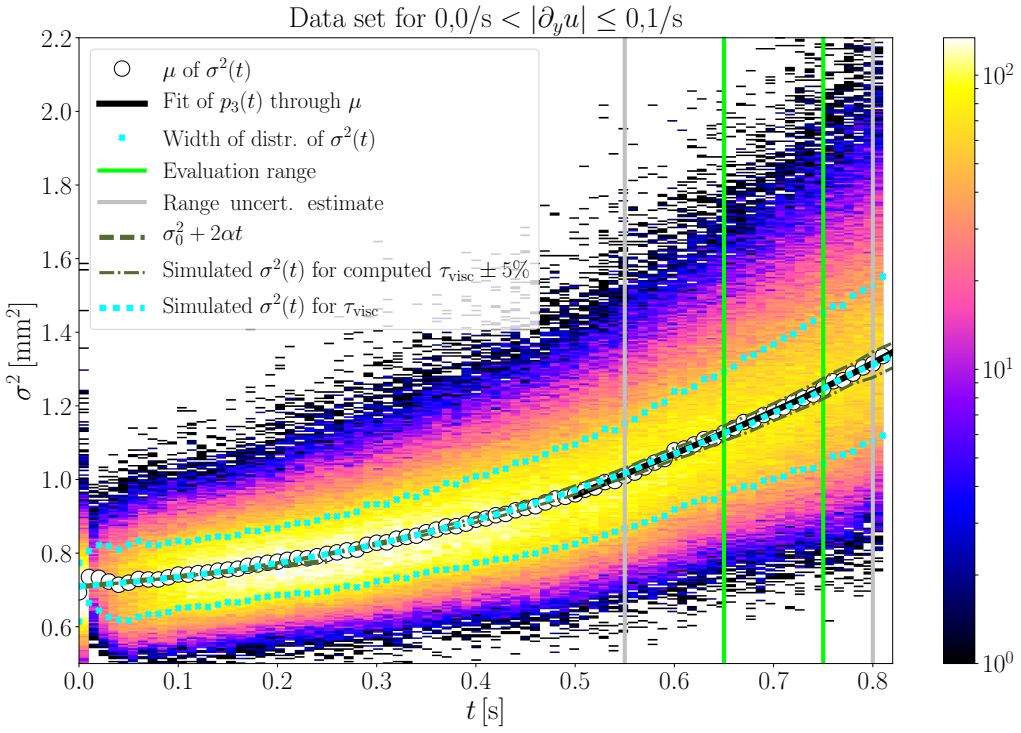

Fig A.1.: Analogous to figure 7.8, but shows the 5 Hz (wind reference) measurement. The result can be found in table 7.1.

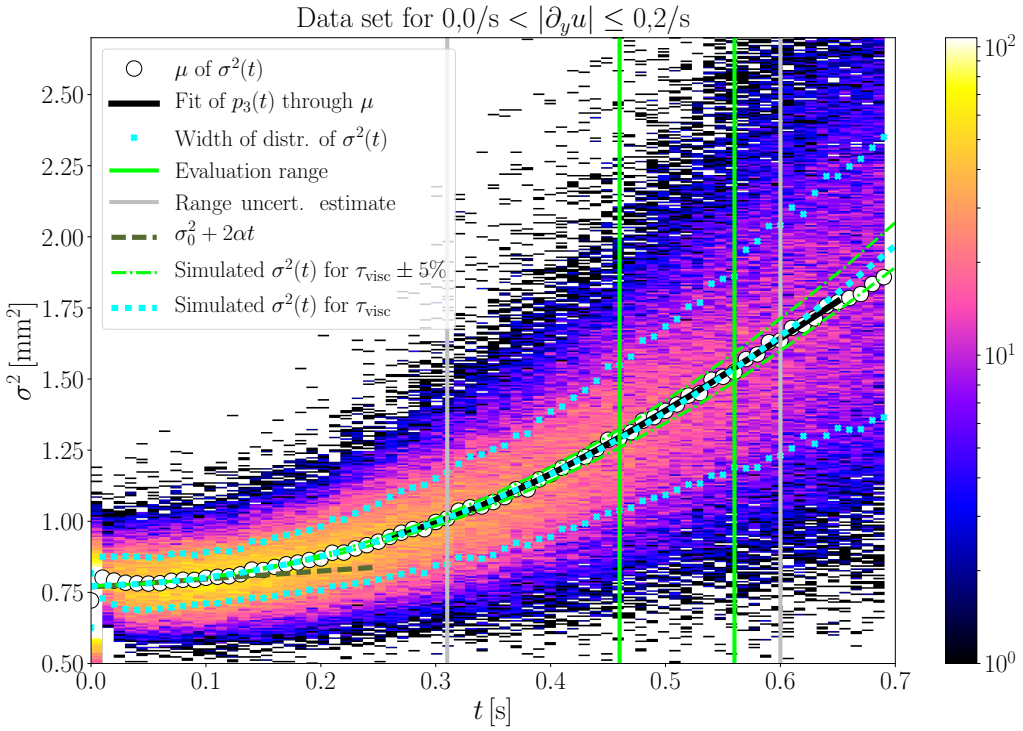

FIG A.2.: Analogous to figure 7.8, but shows the 7,5 Hz (wind reference) measurement. The result can be found in table 7.1.

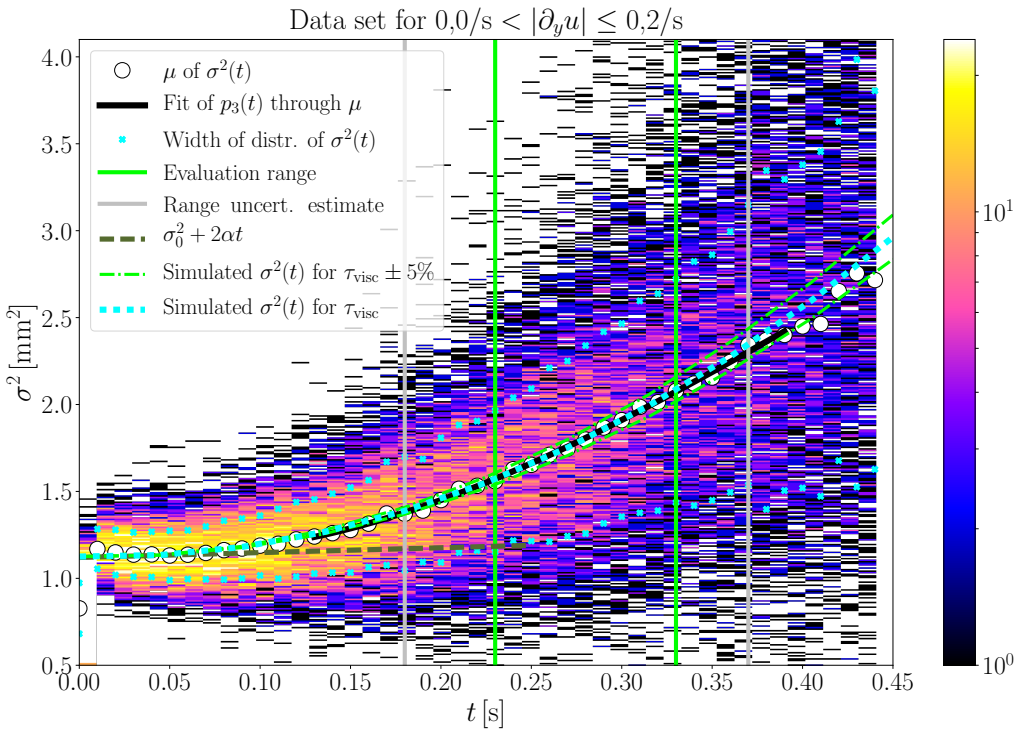

FIG A.3.: Analogous to figure 7.8, but shows the 12,5 Hz (wind reference) measurement. The result can be found in table 7.1.

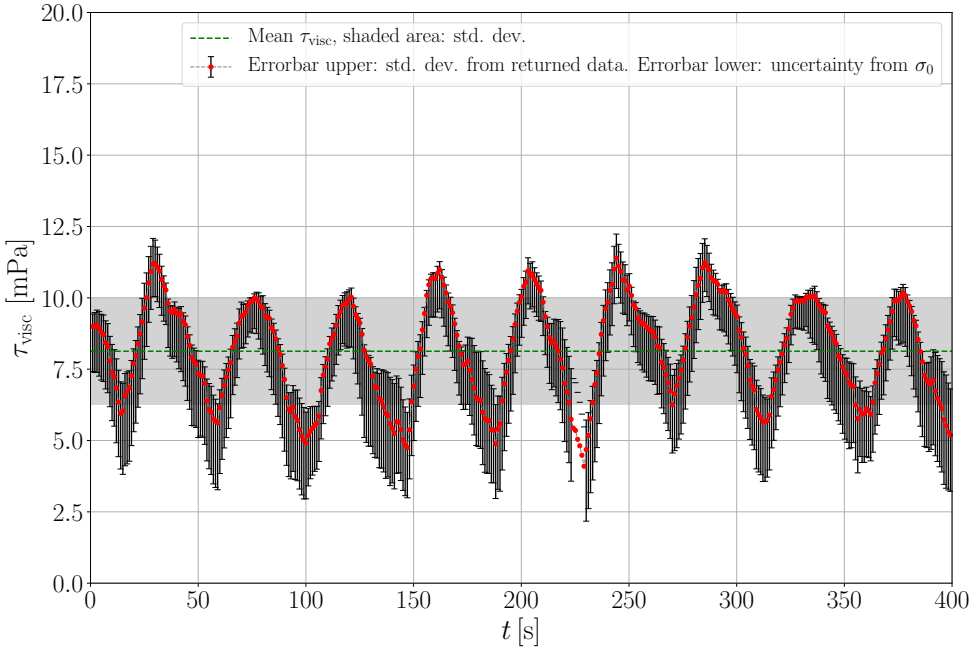

FIG A.4.: Analogous to figure 7.17, but shows the *stationary* 5 Hz (wind reference) measurement. The mean value for $t > 50$ s is (8.1±1.9) mPa. The seen oscillations are not seen in the velocity, see figure 7.11 in section 7.2.

A.2
Stationary measurements, PSV

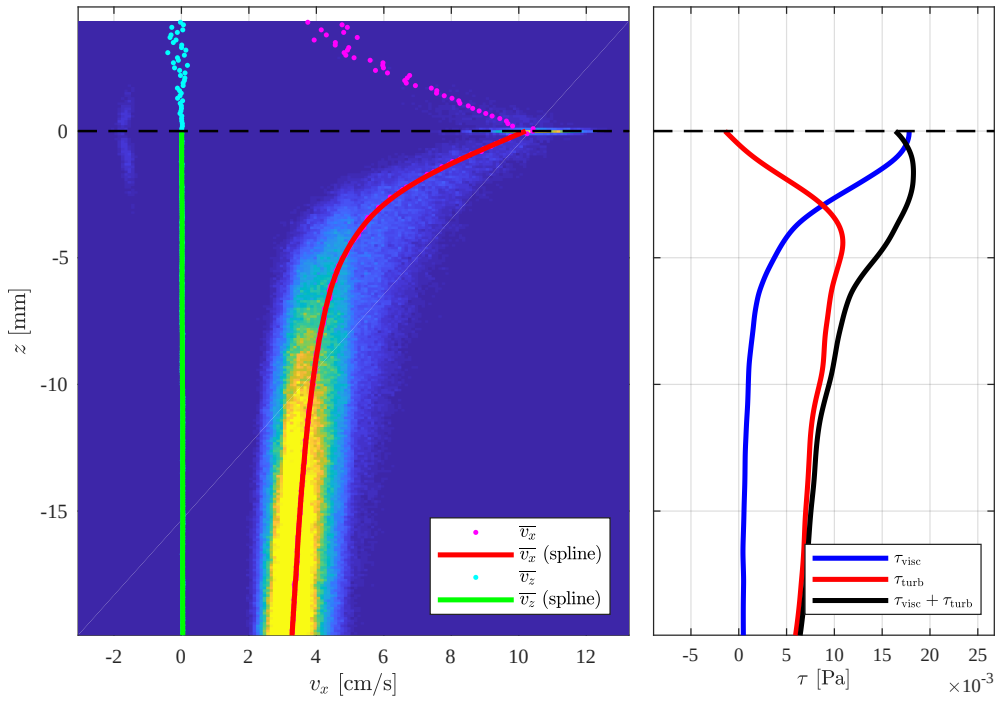

Fig A.5.: Analogous to figure 7.9, but for the 7.5 Hz measurement.

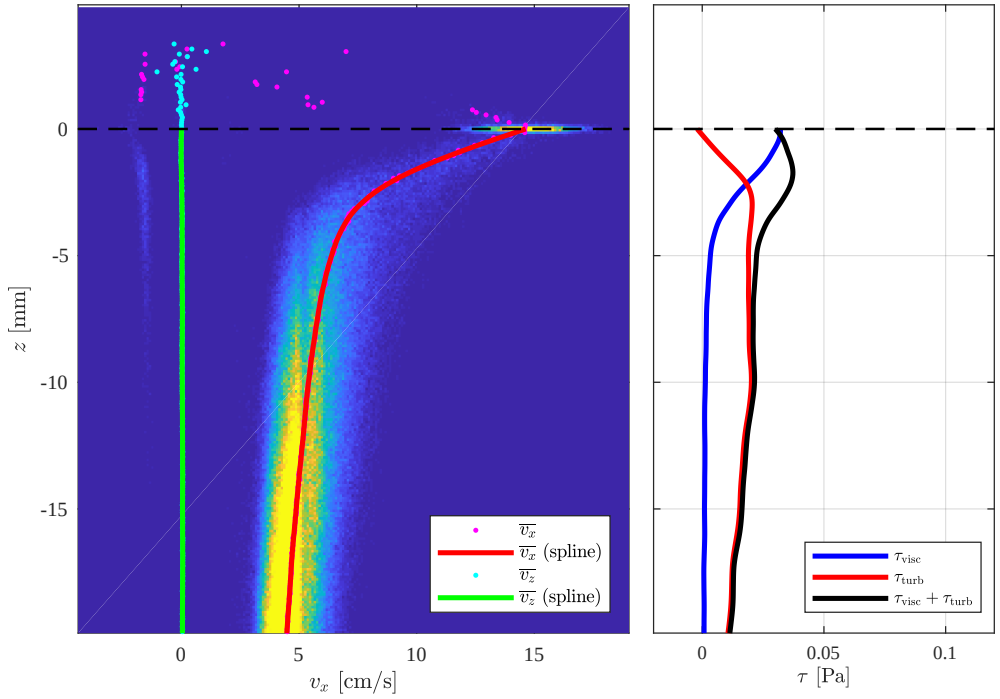

Fig A.6.: Analogous to figure 7.9, but for the 10 Hz measurement.

A.3
Stationary wind on-off measurement

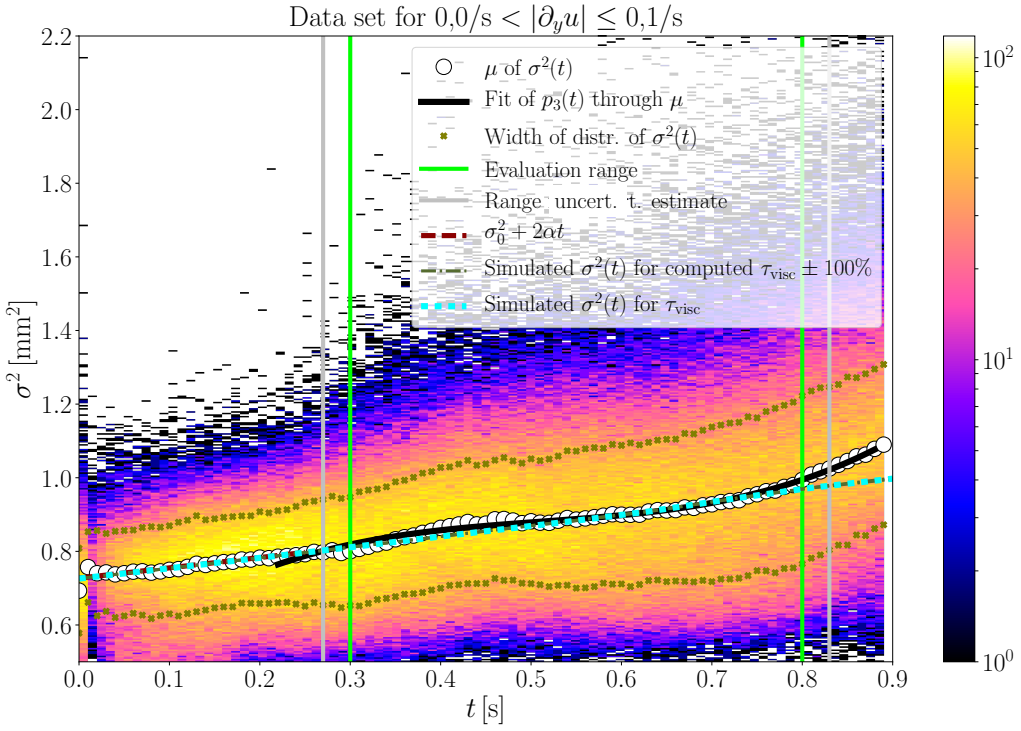

Fig A.7.: Analogous to figure 7.12, but for the part of the wind on-off measurement with the wind turned off. The first 10 s after turning the wind off, were discarded in order to not falsify the result. $\tau_{\text{visc, }\xi\text{, wind off}}$ was determined to $(1.0 \pm 0.9 \pm (0.5)_{\sigma_0})$ mPa.

A.4 Non-stationary measurements

Wind reference [Hz]	$\bar{\tau}_{\mathrm{visc},\,\xi}$ [mPa]
5.0	8.5±1.8
5.0	8.2±1.9
5.0	8.4±1.8
5.0	8.4±1.9
5.0	8.2±1.8
5.0	8.2±1.8
7.5	18.3±1.2
7.5	17.8±1.8
7.5	18.3±1.2
7.5	17.7±1.3
7.5	18.0±1.2
7.5	17.4±1.2
7.5	18.2±1.4
10.0	32.5±3.6
10.0	32.3±3.9
10.0	34.0±3.6
10.0	34.7±3.8
10.0	34.4±3.1
12.5	57.4±4.9
12.5	55.0±5.0
12.5	58.6±6.0
12.5	56.1±5.6
12.5	58.3±4.3

Table A.1.: The averaged results of each of the non-stationary measurements, for times higher than 50 s since turning the wind on. The uncertainties reflect the oscillations in τ_{visc} The agreement to the stationary measurements is good, except for the 12.5 Hz measurements.

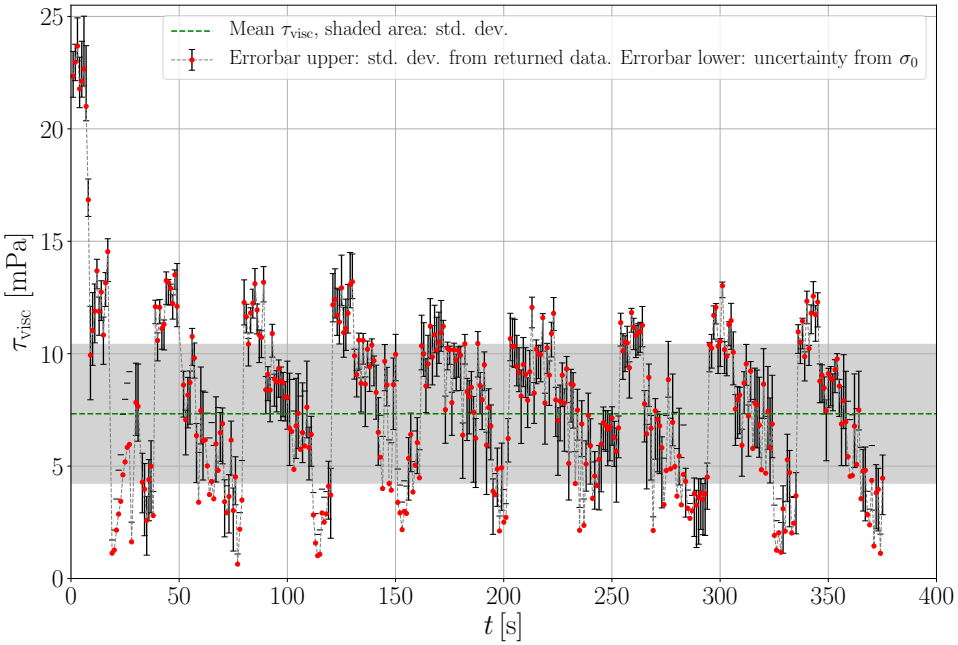

FIG A.8.: The figure shows the evaluation of τ_{visc} as function of time, for the non-stationary 5 Hz measurement, by considering one heated line at a time. The wind was turned on $\sim$ 3s before the first data point. The overshoot seen in figure 7.17 (result by 15 lines at a time) can be seen here too, and also the oscillations can be seen. Notice the rather steep increase, followed by the slower decrease.

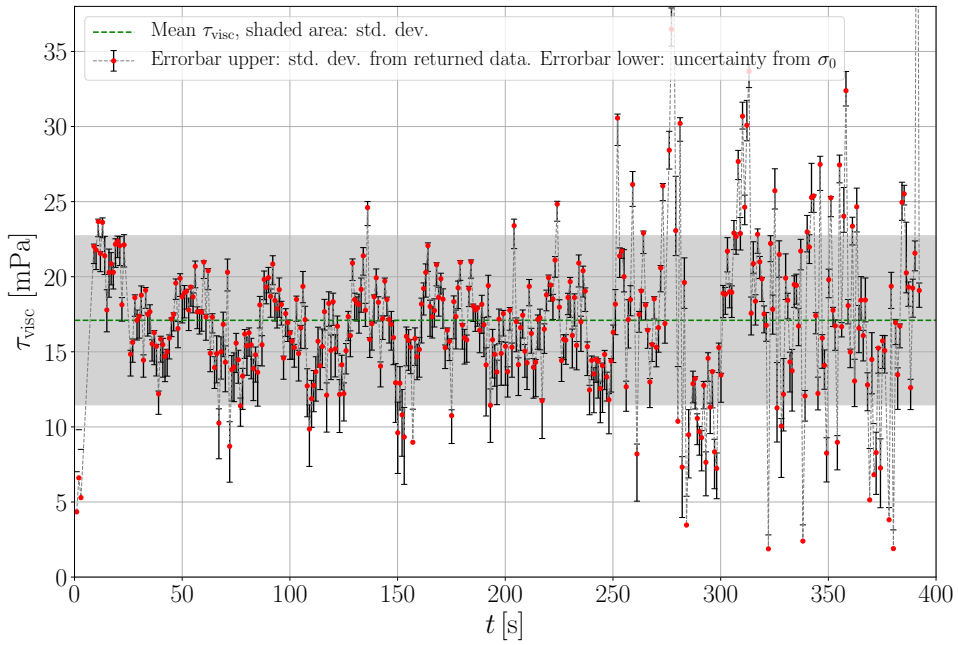

FIG A.9.: Analogous to figure A.8, but for the 7.5 Hz measurement. Both the oscillations for low times and the regime change (see section 7.4) for $t \gtrsim 250$ can be seen.

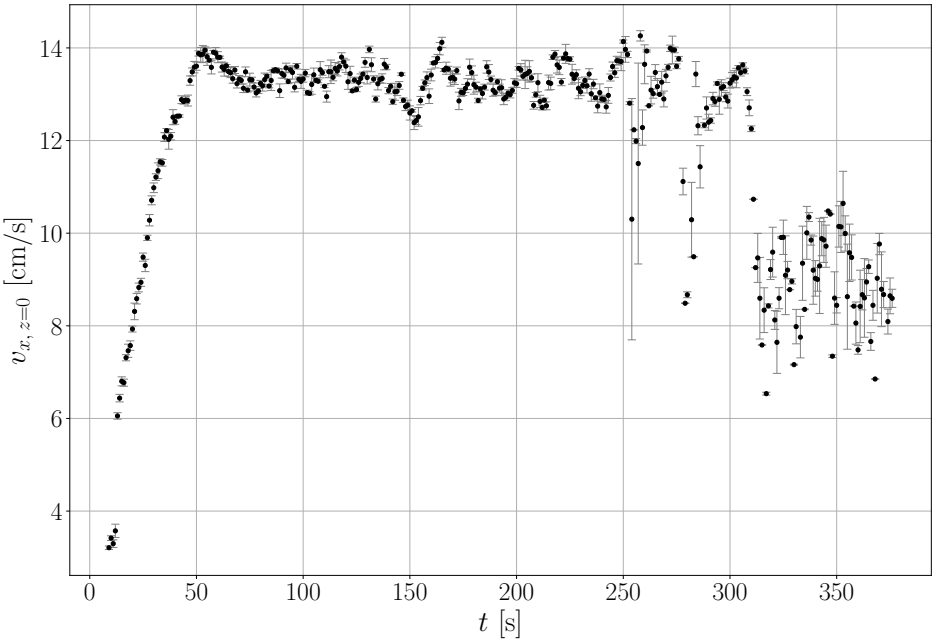

FIG A.10.: The surface velocity v_x for the 7.5 Hz measurement in figure A.9, but for the 7.5 Hz measurement. The large fluctuation in τ_{visc} are associated with a drop in the velocity and regime change. Note that the change is not as abrupt as for the higher wind speeds.

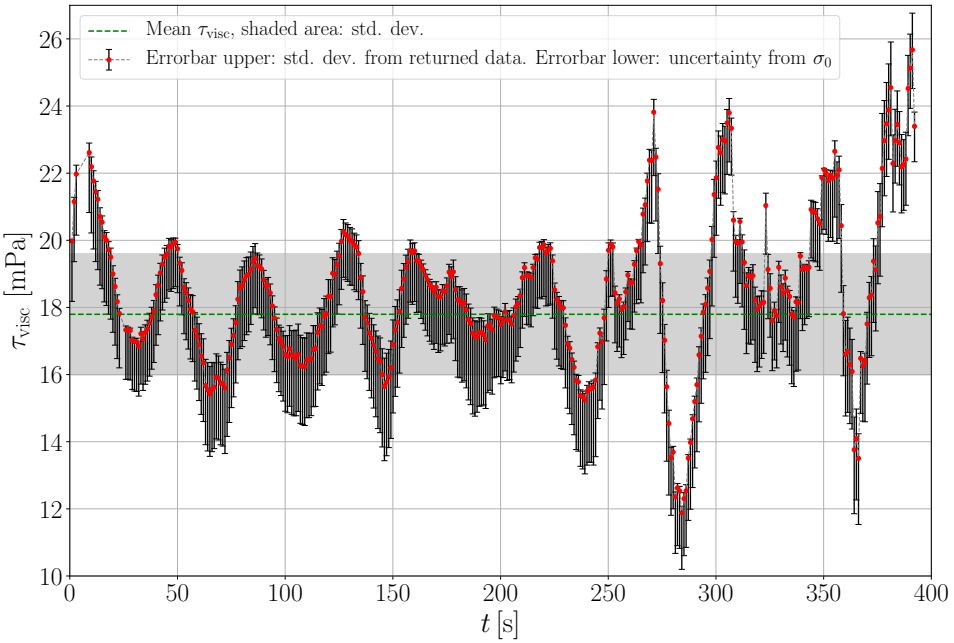

FIG A.11.: The figure is analogous to A.9, but evaluated by 15 lines at a time. The oscillations for low times now become obvious, as well as the stonger fluctuations in τ_{visc} after the change of regime discussed in section 7.4.

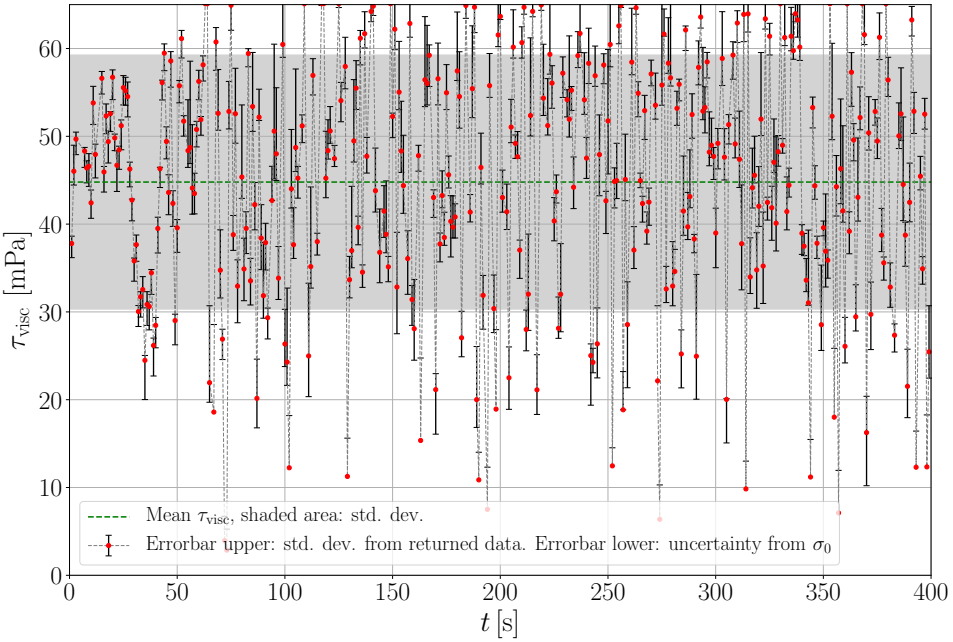

FIG A.12.: Analogous to figure A.8, but for the 12.5 Hz measurement. There is an allusion for a regime change at about 40-50 s (section 7.4), where the points start to scatter strongly. The highest simulated τ_{visc} were 65 mPa, and hence no data points can lie above this, leading to a cut-off at this value. The mean value (green dotted line) is therefore questionable. Further on, at these wind speeds, outliers became more prominent. The used setup in combination with the temporal resolved evaluation, seemed to reach its limits at this wind setting.

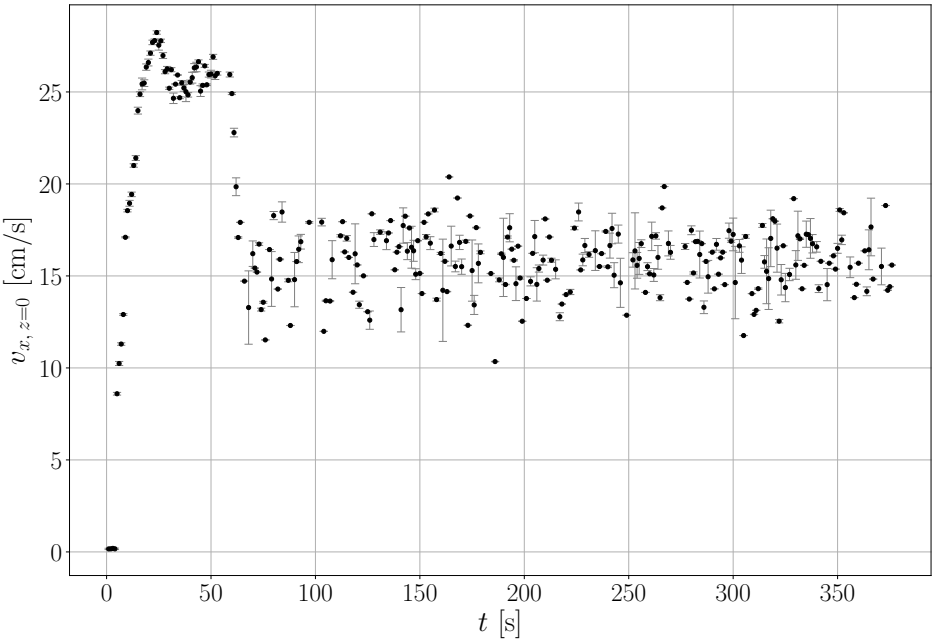

FIG A.13.: The surface velocity v_x for the 12.5 Hz measurement in figure A.12, but for the 7.5 Hz measurement. The large fluctuations in τ_{visc} are associated with a drop in the surface velocity.

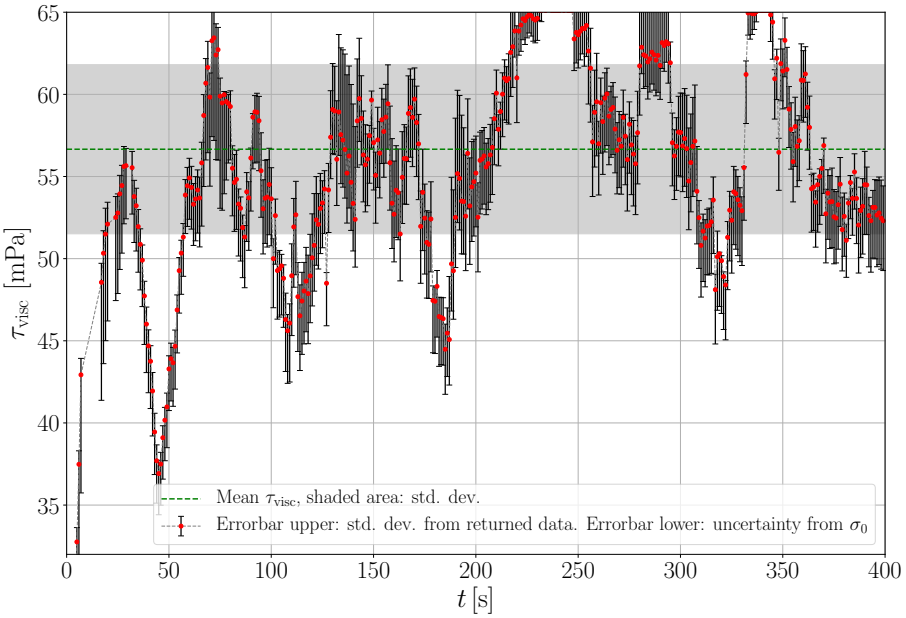

FIG A.14.: Analogous to figure A.14, but for the evaluation of 15 lines at a time. The highest simulated τ_{visc} were 65 mPa, and hence no data points can lie above this, leading to the seen cut-off. The mean value (green dotted line) is therefore questionable.

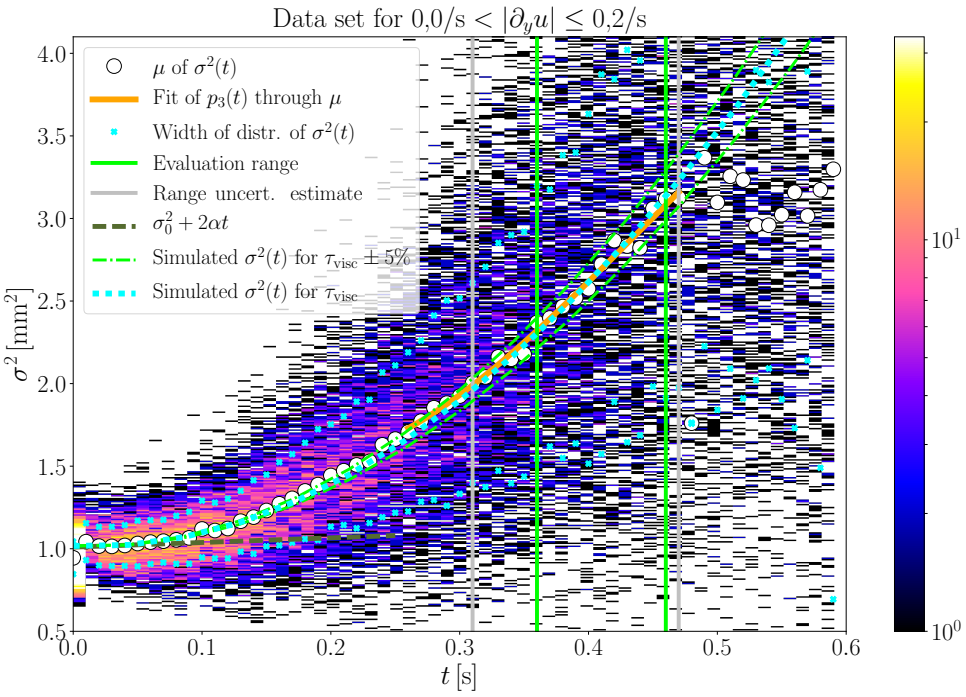

FIG A.15.: The statistical analysis approach for the same measurement as shown in figure A.12 and A.14, for times higher than 200 s since the wind was turned on, in order to have reached more or less stationary conditions. The result was $\tau_{\mathrm{visc},} = (48.7 \pm 0.7)$ mPa, significantly higher than the stationary measurement (table 7.1). The lower value obtained by this method might indicates the mentioned problem with outliers for the higher temporally resolved evaluation.

Erklärung:

Ich versichere, dass ich diese Arbeit selbstständig verfasst habe und keine anderen als die angegebenen Quellen und Hilfsmittel benutzt habe.

Heidelberg, den 01.06.2019 .....